



Swansea University
Prifysgol Abertawe



Swansea University E-Theses

Design and analysis of geodesic tensegrity structures with agriculture applications.

Cowcher, Daniel Thomas

How to cite:

Cowcher, Daniel Thomas (2015) *Design and analysis of geodesic tensegrity structures with agriculture applications..* thesis, Swansea University.
<http://cronfa.swan.ac.uk/Record/cronfa42328>

Use policy:

This item is brought to you by Swansea University. Any person downloading material is agreeing to abide by the terms of the repository licence: copies of full text items may be used or reproduced in any format or medium, without prior permission for personal research or study, educational or non-commercial purposes only. The copyright for any work remains with the original author unless otherwise specified. The full-text must not be sold in any format or medium without the formal permission of the copyright holder. Permission for multiple reproductions should be obtained from the original author.

Authors are personally responsible for adhering to copyright and publisher restrictions when uploading content to the repository.

Please link to the metadata record in the Swansea University repository, Cronfa (link given in the citation reference above.)

<http://www.swansea.ac.uk/library/researchsupport/ris-support/>



**Prifysgol Abertawe
Swansea University**

**Design and Analysis of Geodesic
Tensegrity Structures with Agriculture
Applications**

Daniel Thomas Cowcher

Submitted to Swansea University in fulfilment of the
requirements for the Degree of Master of Research

Swansea University, College of Engineering

2015



ProQuest Number: 10798036

All rights reserved

INFORMATION TO ALL USERS

The quality of this reproduction is dependent upon the quality of the copy submitted.

In the unlikely event that the author did not send a complete manuscript and there are missing pages, these will be noted. Also, if material had to be removed, a note will indicate the deletion.



ProQuest 10798036

Published by ProQuest LLC (2018). Copyright of the Dissertation is held by the Author.

All rights reserved.

This work is protected against unauthorized copying under Title 17, United States Code
Microform Edition © ProQuest LLC.

ProQuest LLC.
789 East Eisenhower Parkway
P.O. Box 1346
Ann Arbor, MI 48106 – 1346

Abstract

This report aims to promulgate and elucidate the effective application of scientific principles in the design and optimisation of tensegrity structures for practical applications. By developing the intrinsic geometry of the geodesic dome and applying tensegrity design principles, a range of efficient, lightweight, modular structures are developed and broadly classified as *geodesic tensegrity structures*. Novel systems for clustering domes in two dimensions are considered and the analytical geometry required to generate various dome structures is derived from first principles. Computational methods for performing the design optimisation of tensegrity structures are reviewed and explained in detail. It is shown how an efficient, unified computational framework, suitable for the analysis of tensegrity structures in general, may be developed using computations which involve the equilibrium matrix of a structure. The importance of exploiting symmetry to simplify structural computations is highlighted throughout, as this is especially relevant in the analysis of large dome structures. A novel approach to generating the global equilibrium matrix of a structure from element vectors and implementing symmetry subspace methods is presented, which relies on the choice of an appropriate coordinate system to reflect the symmetry of a structure. A new algorithm is developed for implementing symmetry subspace methods in a computer program which enables the symmetry-adapted vector basis to be generated more efficiently. Methods for analysing kinematically indeterminate tensegrities and prestressed mechanisms and performing the prestress optimisation of a tensegrity structure are briefly reviewed and explained. Efficient tensegrity modular systems are developed for constructing a range of double-layer geodesic tensegrity domes and grids, based on the pioneering work of the artist, Kenneth Snelson. Finally, the cultural significance of tensegrity technology is illustrated by focusing on a range of novel applications in agriculture and sustainable development and adopting the holistic, "*design science*," approach advocated by Buckminster Fuller.

Declaration

This work has not previously been accepted in substance for any degree and is not being concurrently submitted in candidature for any degree.

Signed.. Date..18/01/2016.....

Statement 1

This dissertation is the result of my own independent work/investigation, except where otherwise stated. Other sources are acknowledged by footnotes giving explicit references. A bibliography is appended.

Signed..] Date..18/01/2016.....

Statement 2

I hereby give my consent for my dissertation, if relevant and accepted, to be available for photocopying and for inter-library loan, and for the title and summary to be made available to outside organisations.

Signed Date..18/01/2016.....

Contents

Acknowledgements	5
List of Figures	7
List of Tables & Boxes	9
1. Introduction	10
1.1. A brief account of the early history of geodesic domes and tensegrities	10
1.2. The evolution of tensegrity theory	12
1.3. Design in nature	15
1.4. The nature of tensegrity geodesic spheres	18
1.5. Applications	23
1.6. Aims and Objectives	25
1.7. References	28
2. Geodesic Tensegrity Domes and Dome Honeycomb Structures	31
2.1. Geodesic domes	31
2.2. Planar tessellations and linkages	34
2.3. Geodesic breakdown systems and coordinate geometry	41
2.3.1. Breakdown systems	41
2.3.2. Coordinate systems and transformation equations	45
2.4. Basic geometry of the honeycomb dome	49
2.5. Dome honeycombs; design concepts and functionality	54
2.6. References	58
3. Structural Analysis of Tensegrity Domes by the Force Method	59
3.1. Structural computations with the singular value decomposition of the equilibrium matrix	59
3.1.1. SVD of the equilibrium matrix	61
3.1.2. Physical interpretation	62
3.1.3. Formulae for structural computations	63
3.2. Assembly of equilibrium matrices in cylindrical polar coordinates for reticulated assemblies	64
3.3. Matrix methods for computational analysis of tensegrity dome frameworks	69
3.3.1. X-module element matrices in 2-dimensions	69
3.3.2. X-module element matrices in 3-dimensions	74
3.4. References	79

4. A Computational Framework for the Analysis of Symmetric Structures	80
4.1. Symmetry group representations for structures with C_{6v} symmetry	81
4.2. Symmetry-adapted coordinates and symmetry subspace methods	86
4.2.1. Fundamentals of group representation theory	86
4.2.2. Block-diagonal form of the equilibrium and flexibility matrices	89
4.3. Assembly of symmetry-adapted vector basis matrices	91
4.4. Analysis of the symmetry-substructure	95
4.5. References	98
5. Analysis of Internal Mechanisms and Prestress States for Tensegrity Structures	99
5.1. Rigidity Theory	99
5.1.1. Infinitesimal rigidity	100
5.1.2. Prestress stability and super stability	101
5.1.3. Higher order mechanisms	102
5.1.4. Finite mechanisms	103
5.2. Analysis of internal mechanisms for kinematically and statically indeterminate reticulated systems	104
5.2.1. Geometrical characterisation algorithm for mechanisms order analysis	105
5.3. Prestress design and optimisation	108
5.3.1. Theory of prestress design for tensegrity structures	108
5.3.2. The integral feasible prestress optimisation algorithm	109
5.3.3. Discussion and further applications	111
5.4. References	111
6. Geodesic Tensegrity Dome Design Development	113
6.1. Design of 3-dimensional tensegrity modules	113
6.1.1. The tensegrity prism	113
6.1.2. Applications of the T-prism in dome design	117
6.2. Design of a dome honeycomb structure	122
6.3. Generalised geodesic tensegrity structures	133
6.4. Applications	141
6.5. References	145
7. Conclusions	146

Acknowledgements

I would like to thank all those who have helped make this project possible and supported me on my journey of discovery.

Many thanks go to my project supervisor, Professor Mike Friswell for his patience and encouragement.

My special thanks go to the Douglas Bomford Trust for the research grant I received from them and their continued interest in developing innovative structural systems for agriculture applications involving greenhouse technology. I am especially grateful to the trustees, Malcolm Crabtree and Peter Redman, who visited me at Swansea University and offered their expert advice, encouragement and suggestions on how to develop the technology further.

I would like to thank Matthew Parker and William Hyner for discussions I had with them regarding the project and for providing inspiration for certain parts of the introduction.

Thanks and praise also goes to Buckminster Fuller and Kenneth Snelson whose pioneering work has been a constant source of inspiration throughout the design process.

Finally, I would like to thank my family for their encouragement and support.

*“Imagination is more important than knowledge.
Knowledge is limited, imagination encircles the world.”*

Albert Einstein

List of Figures

Fig. 1.1: Schütte-Lanz SL1 rigid airship..... Carl Zeiss geodesic dome.....	10
Fig.1.2: Snelson's "X-piece," sculpture. "X-module," in Snelson's patent.	11
Fig. 1.3: An illustration of loganson's sculpture. Tensegrity 3-prism.	12
Fig. 1.4: Geodesic forms in cell cytoskeleton..... Isotropic vector matrix	15
Fig. 1.5: Jitterbug transformations. Jitterbug model. Isotropic vector equilibrium.	16
Fig. 1.6: Tensegrity icosahedron. Nucleated tensegrity cell model.....	17
Fig. 1.7: Buckminsterfullerene. Carbon nonotube. Graphene.....	18
Fig. 1.8: Deflection of curved members under compressive and tensile loads.....	19
Fig. 1.9: Bracing tension against compression. Rectangular bay braced by curved members.....	20
Fig. 2.1: Dymaxion Air-Ocean map.....	31
Fig 2.2: Structural details of the Montreal Biosphere.....	33
Fig.2.3: Hexagonal tessellation. Hexagonal lattice linkage with triangular bracing.....	36
Fig. 2.4: Unstable, open lattice linkage..... The "X-trihexagonal," stable planar lattice structure.....	36
Fig. 2.5: Geodesic subdivision of an octahedron face using the X-trihex lattice structure...	37
Fig. 2.6: The "X-module" tensegrity, with details of strut to strut connections.....	39
Fig. 2.7: Illustration of the dome of Fig. 2.5 in its folded configuration.....	40
Fig. 2.8: Polytope contraction operations applied to the X-trihex lattice.....	41
Fig. 2.9: Superposition of 3v Class I and 6v Class II subdivision of a triangular chart.	43
Fig. 2.10: Constructing an X-trihex chart lattice from triangular lattices	44
Fig. 2.11: Hybrid X-trihex chart lattice.....	44
Fig. 2.12: 5v Class I chart lattice, indicating local coordinate and node numbers	46
Fig. 2.13: X-trihex chart lattice transformation under octahedral centre projection	48
Fig. 2.14: Symmetry substructure for the X-trihex dome.. developed for dome clustering..	51
Fig. 2.15: Simplified model of an X-trihex lattice dome, developed for clustering.....	52
Fig. 2.16: Simplified dome modules assembled in a honeycomb structure.....	55
Fig. 2.17: Deployable, geodesic tensegrity dome model, mounted in a hexagonal box.	56

Fig. 3.1: A typical element in plan view with local and global coordinates indicated	67
Fig. 3.2: A two-dimensional hexagonal cable structure.....	68
Fig.3.3: X-module composed of two beams joined by a scissor hinge and braced with cables.....	70
Fig. 3.4: Two-dimensional beam element with local coordinate system $1, x, y$	71
Fig. 4.1: External coordinate system and reflection symmetry planes for the structure of Fig. 3.2.....	81
Fig. 6.1: Tensegrity Prism	113
Fig. 6.2: T-Prism: Cylindrical Polar Coordinates	114
Fig. 6.3: Hybrid X-trihex lattice	118
Fig. 6.4: Kenneth Snelson, Assembly of 3 X-modules.	119
Fig. 6.5: Hybrid tensegrity prism	119
Fig. 6.6: Simplified Hybrid T-prism	121
Fig. 6.7: Hybrid X-trihex lattice dome clustering	124
Fig. 6.8: Hybrid X-trihex lattice dome sub-structure	125
Fig. 6.9: Double T-prism	127
Fig. 6.10: Application of the Double T-prism in dome sub-structure design	127
Fig. 6.11: Dome sub-structure incorporating a simplified version of the Double T-prism.	127
Fig. 6.12: Plan and elevation of dome sub-structure attached to foundation	128
Fig. 6.13: Rigid tensegrity tetrahedron provides a strong structural foundation.....	129
Fig. 6.14: Geodesic tensegrity dome design – Plan, elevation and perspective view.....	130
Fig. 6.15: Dome honeycomb – cluster of three domes	131
Fig. 6.16: Collapsible dome.....	132
Fig. 6.17: Class II, frequency 4 X-trihex chart lattice.....	135
Fig. 6.18: Double-layer tensegrity grid composed of X-modules and T-prisms	137
Fig. 6.19: Tensegrity Torus: Assembly of 6 X-modules and 6 T-prisms.	138
Fig.6.20: Assembly of 3 hybrid T-prisms.....	139

List of Tables & Boxes

Tab. 2.1: 5v Class I chart lattice coordinate transformations	47
Tab. 2.2: X-trihex chart lattice coordinate transformations	48
Tab. 2.3: X-trihex dome global Cartesian coordinates	52
Tab. 4.1: Irreducible representations of symmetry group C_{6v}	87
Tab. 6.1: T-prism cylindrical polar coordinates	115
Tab. 6.2: T-prism Cartesian coordinates	117
Tab. 6.3: Hybrid X-trihex chart lattice coordinate transformations	122
Tab. 6.4: Cartesian dome nodal coordinates	123
Tab. 6.5: Geodesic Tensegrity Chart Lattice Structures	134
Box 4.1: <i>Algorithm 4.1</i>	93
Box 4.2: <i>Algorithm 4.2</i>	94

Chapter 1 Introduction

1.1 A brief account of the early history of geodesic domes and tensegrities

The geodesic dome, developed by Buckminster Fuller in the 1950's, represented a major breakthrough in the development of lightweight structures worldwide, and continues to be one of the most efficient structures for enclosing large volumes over a wide area, largely unsupported. Despite the initial success of the geodesic dome, many of its leading proponents were disappointed by the slow pace of development and limited range of applications that have been realised over the second half of the 20th century (Makowski, 1984). Although the basic geometry of the geodesic dome has remained unaltered, a number of improvements in the local structure have led to a wide range of structural systems and types of geodesic domes.

The structural principles of the geodesic dome had been used by engineers some 20 years before Fuller developed the intrinsic mathematics and terminology used to describe the dome. In fact, the first geodesic dome appeared in Germany shortly after World War 1 and was designed by Walther Bauersfeld. The dome was constructed for a planetarium in Jena, Germany, which opened to the public in 1926 (Figure 1.1). Geodesic space frames were simultaneously being developed in the UK by the aeronautical engineer and inventor Barnes Wallis. In the 1930's, Wallis developed the geodesic construction method for the airframes of aircraft. Combined with a light alloy structure, the arrangement of members to follow

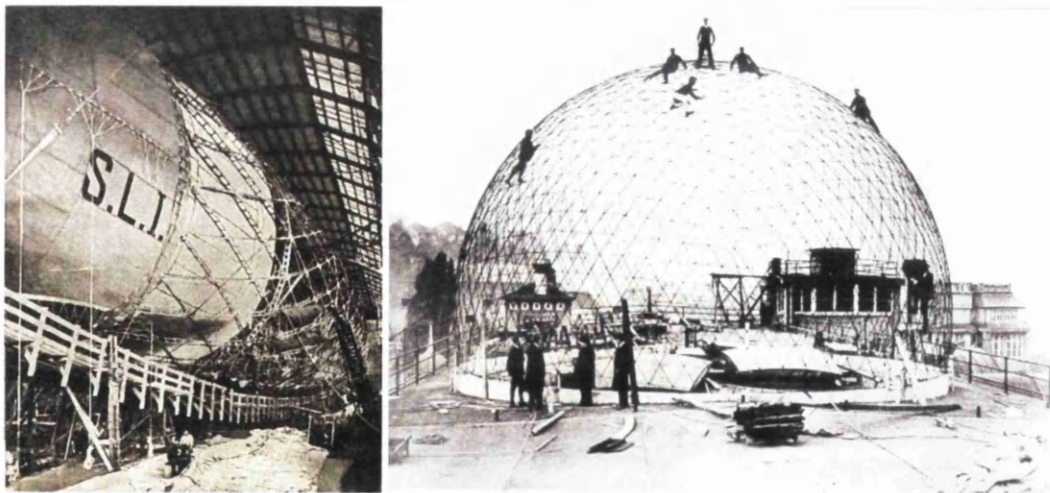


Figure 1.1: Schütte-Lanz SL1 rigid airship under construction, 1911 (left) (SL1 Wooden Lattice framework n.d.). Construction of the Carl Zeiss geodesic dome in Jena (Germany) 1922 (right) (Bauersfeld-Zeis-Jena n.d.).

geodesic curves forming a two-way basket weave along the inner surface of the fuselage produced an exceptionally strong, lightweight framework. Geodesic cable structures had been used previously in the wire networks used to surround the gasbags of airships. As early as 1911 a geodetic airframe was built for the pre-World War 1 Schütte-Lanz SL1 rigid airship's envelope structure (Figure 1.1).

Tensegrity structures represent a broad category of structures, the simplest forms of which are essentially self-supporting, self-stressed, reticulate systems composed of tensile and compressive members. Much of the early work on tensegrity began in the 1950's and its three main proponents were David Georges Emmerich, Richard Buckminster Fuller and Kenneth Snelson. Snelson described tensegrity as "*floating compression*," whereas Fuller described tensegrity systems as "*islands of compression in an ocean of tension*." The name "*Tensegrity*," was coined by Fuller in 1955 as a contraction of "*tensional*," and "*integrity*." Tensegrity structures and geodesic domes were developed in parallel as a result of the inspiration and creative output from Black Mountain College where Bucky Fuller and the artist Kenneth Snelson first met in 1948. A major breakthrough in the early development of tensegrity structures came from the pioneering work of Snelson who presented his first "X-piece," sculpture in 1949, although the ideas of Fuller were undoubtedly an inspiration to the young artist (Motro, 1990).

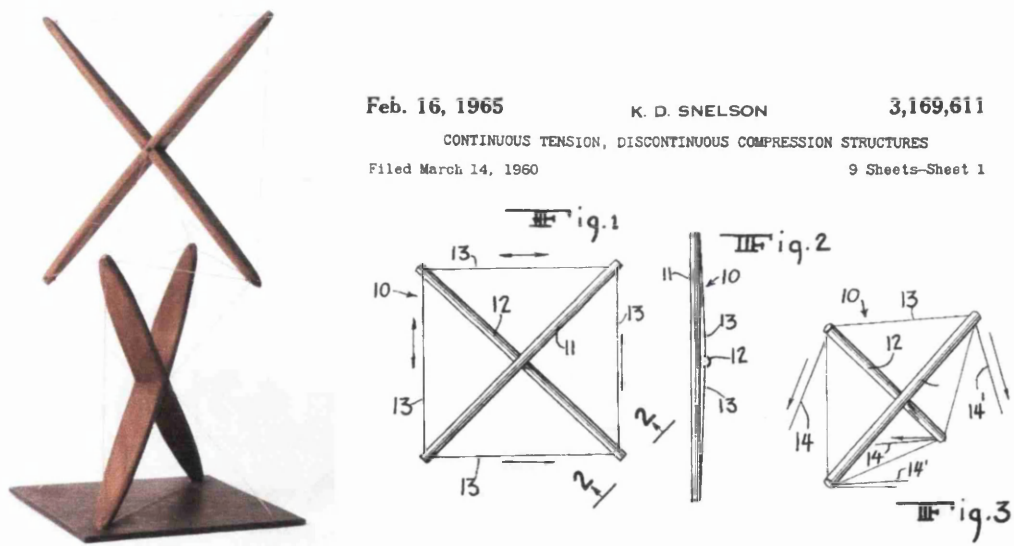


Figure 1.2: Snelson's "X-piece," sculpture (left) (Snelson, 1948), "X-module," in Snelson's patent (right) (Snelson, 1965).

Emmerich, discovered tensegrity independently in France at around the same time, however, Emmerich had reported that the first proto-tensegrity structures appeared in the work of Russian

constructivist artists in the 1920s. In particular, in the sculptures of the Latvian constructivist Karl loganson could be seen the emergence of tensegrity principles and of early tensegrity structures (Figure 1.3). Although most of loganson's work was destroyed or lost from Soviet Russia during the Great Purge of the 1930's, photographs of his constructions exhibited in the 1921 Obmochu exhibition in Moscow were widely distributed in latter publications. loganson's work was undoubtedly an inspiration to Emmerich and would have influenced Snelson through the Bauhaus (Gough, 1998).

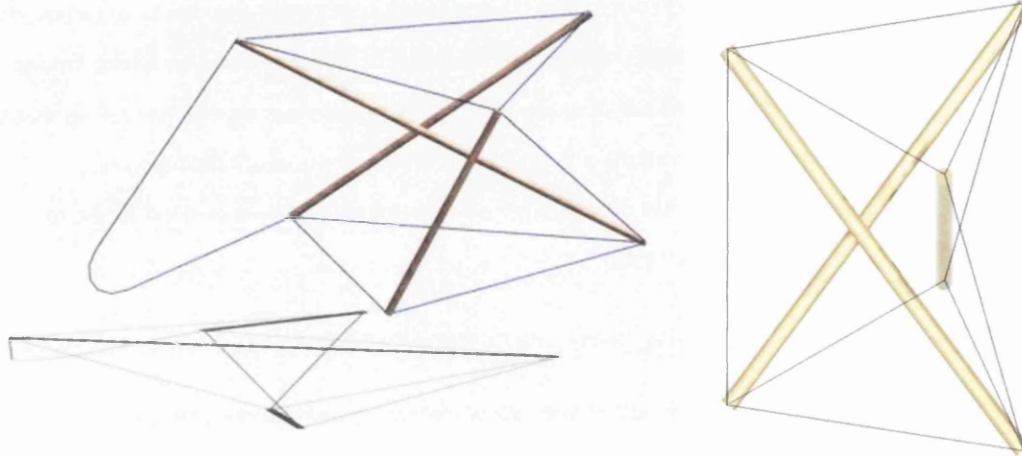


Figure 1.3: An illustration of loganson's sculpture (left) (Tensegridad.es, 2010).
Tensegrity 3-prism (right).

1.2 The evolution of tensegrity theory

Emmerich, Fuller and Snelson were each granted patents describing similar structural systems and adopted similar design principles. The tensegrity 3-prism (Figure 1.3) appeared in all three of the men's patents and resembled loganson's sculpture, although the latter was a flexible structure, and not self-stable as most tensegrity structures were later designed to be (Motro, 2006). Snelson described a tensegrity structure or simply a tensegrity as follows:

Definition 1.1:

"Tensegrity describes a closed structural system composed of a set of three or more elongate compression struts within a network of tension tendons, the combined parts mutually supportive in such a way that the struts do not touch one another, but press outwardly against nodal points in a tension network to form a firm, triangulated, prestressed, tension and compression unit."

(Snelson, 2012)

In the modern literature the definition of a tensegrity is often extended to include reticulate structures in which the struts are permitted to make contact with each other, but the structure should still be free-standing and have both tensile and compressive members (Ohsaki, Zhang, 2006; Motro, 2006).

Both Fuller and Snelson advocated the principle of *"continuous tension, discontinuous compression,"* i.e. that the tensile components of a tensegrity constitute a continuous set and the struts constitute a discontinuous set. Although, most of the tensegrity structures designed and built by Fuller were reticulated structures, in his writings concerning the theory of tensegrity, he used tensegrity principles to explain a much wider range of structures and systems. Under this extended definition, Fuller included pneumatic structures, geodesic domes as well as many of the structural systems found in nature (Fuller, 1975). This more general definition of tensegrity was useful in the evolution of tensegrity as a structural principle and led Motro to suggest the following extended definition:

Definition 1.2:

"A tensegrity is a system in a stable self-equilibrated state comprising a discontinuous set of compressed components inside a continuum of tensioned components." (Motro, 2006)

Fuller extended the definition of tensegrity still further and even to the realm of metaphysics. In his book '*Synergetics*,' he wrote:

"The great structural systems of the Universe are accomplished by islanded compression and omnicontinuous tension." (794.01 (Fuller, 1975))

"All structures, properly understood, from the solar system to the atom, are tensegrity structures. Universe is omnitemporal integrity." (700.04 (Fuller, 1975))

Many of Fuller's grand proposals regarding the universality of tensegrity principles have miraculously been verified by leading scientists, largely as a result of empirical studies at the atomic and molecular level (Ingber and Landau, 2012). On the other hand, most of Fuller's futuristic predictions regarding the technological advancement of humanity through adopting tensegrity principles have remained unfulfilled and regarded by most as pure science fiction (Makowski, 1984). Despite Fuller's comprehensive treatment of tensegrity, most of his writings remain incomprehensible, and are largely ignored by the scientific community.

In regard to the structural design of geodesic domes, Fuller clearly stated a number of key ideas in his '*Synergetics*,' which were not taken on board by the next generation of tensegrity scientists and remained absent from subsequent developments of the tensegrity theory. In the first volume of '*Synergetics*,' Fuller stated the following:

"All geodesic domes are tensegrity structures, whether the tension- islated compression differentiations are visible to the observer or not."(794.01 (Fuller, 1975))

In order to qualify this statement, Fuller used an analogy with hydraulically or pneumatically inflated structures. Pneumatic structures – such as footballs – provide a firm shape when inflated due to the internal volume of pressurised air impinging outwardly against the flexible, tensile skin. Pneumatic structures are included under the extended definition of tensegrity structures given by Motro when the internal volume of air is interpreted as the compressed component of the tensegrity. It does not immediately follow that all geodesic domes can be included under this same definition of tensegrity. In order to gain further insight into Fuller's thinking it is worth reconsidering his original definition of tensegrity, given as follows:

Definition 1.3:

"Tensegrity describes a structural-relationship principle in which structural shape is guaranteed by the finitely closed, comprehensively continuous, tensional behaviours of the system and not by the discontinuous and exclusively local compressional member behaviours"(700.011 (Fuller, 1975))

To the casual reader this definition may seem a little vague and through refinement and search for greater clarity, Fuller's intended meaning may have been misinterpreted and diminished in alternative versions of the definition, put forward by various authors. Fuller's original definition is however, the most general, and in particular, includes a larger subset of the spatial reticular structures than is widely recognised today as tensegrity structures. Fuller attempted to explain the structural principles of the geodesic dome and the link with tensegrity at some length in his book '*Synergetics*.' Geometric arguments in support of Fuller's conjecture are also presented by Kenner (Kenner, 1976), who shows that under certain circumstances there is no contradiction between Fuller's statement (794.01) and the definition of tensegrity given by Snelson (Def. 1.1). Empirical evidence in support of Fullers interpretation of tensegrity is provided by recent scientific discoveries, some of which are highlighted below.

1.3 Design in nature

During the 1980's Donald Ingber developed his ambitious theory of cellular tensegrity and was able to demonstrate how patterns of cytoskeleton structure and integration in living cells can be modelled using three dimensional tensegrities (Ingber et al., 1981; Ingber and Jamieson, 1982, 1985; Ingber, 1993). The tensegrity models for the cytoskeleton proposed by Ingber were based on Fullers ideas and definition of tensegrity. The "*Jitterbug*," (Figure 1.5) a model for a foldable truss based on the cuboctahedron was the basic structure used as a model for the cytoskeleton (Ingber, 1993).

Fuller had shown how the flexible cuboctahedron could be transformed into more stable configurations including the icosahedron, octahedron and tetrahedron as a result of progressive compacting, equatorial twisting and folding (Fuller, 1979; Edmondson, 1987) (Figure 1.5). Ingber exploited these mechanisms as well as the rectified cubic honeycomb structure; a space filling tessellation composed of octahedra and cuboctahedra; in order to explain the structure and function of the cytoskeleton. Ingber proposed that if the loosely packed, unstable, rectified cubic honeycomb structure were to implode, under the influence of increased internal tension, a highly stable configuration of the structure composed of closely packed tetrahedra would be observed. Fuller referred to this space filling tessellation of octahedra and tetrahedra as the isotropic vector matrix (Fuller, 1975) (Figures 1.4 and 1.5). When viewed from above, this structure exhibits hexagonal lattice planes which correspond to the patterns which are observed within the cytoskeleton of living cells (Ingber, 1993) (Figure 1.4).

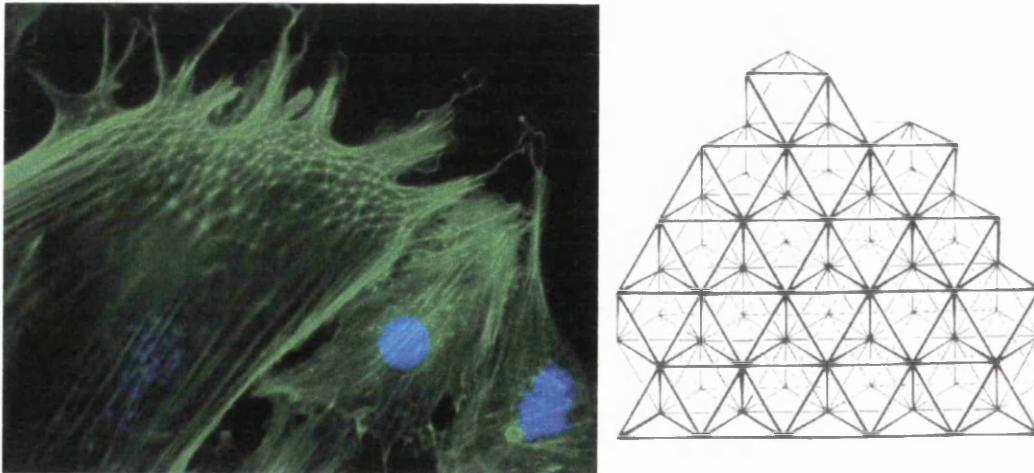


Figure 1.4: Geodesic forms in the tensed cytoskeleton of a living human cell (left) (Ingber, 2011(1)). Isotropic vector matrix (right)

Due to the reversibility of the geometric transformations of the structure, Ingber was able to explain a wide range of observable phenomenon and the mechanical role of the cell cytoskeleton (Ingber, 1993). Ingber also developed simplified models of the tensegrity cell based on the tensegrity icosahedron (Figure 1.6) and, working with Dimitrije Stamenovic, was able to predict how cells from many different tissues behave mechanically (Stamenovic, 1996).

Ingber's approach highlights the link between geodesic geometry and tensegrity, for example, the cuboctahedron dome is an unstable truss and therefore cannot be included under the established view of tensegrity held by structural engineers (Ohsaki, Zhang, 2006). Fuller on the other hand, believed all geodesic domes, as well as a range of other space structures were to be included as tensegrities. For example, the isotropic vector matrix structure belonged to a class of tensegrity structures defined by Fuller as allspace-filling tensegrity structures (Fuller, 1975).

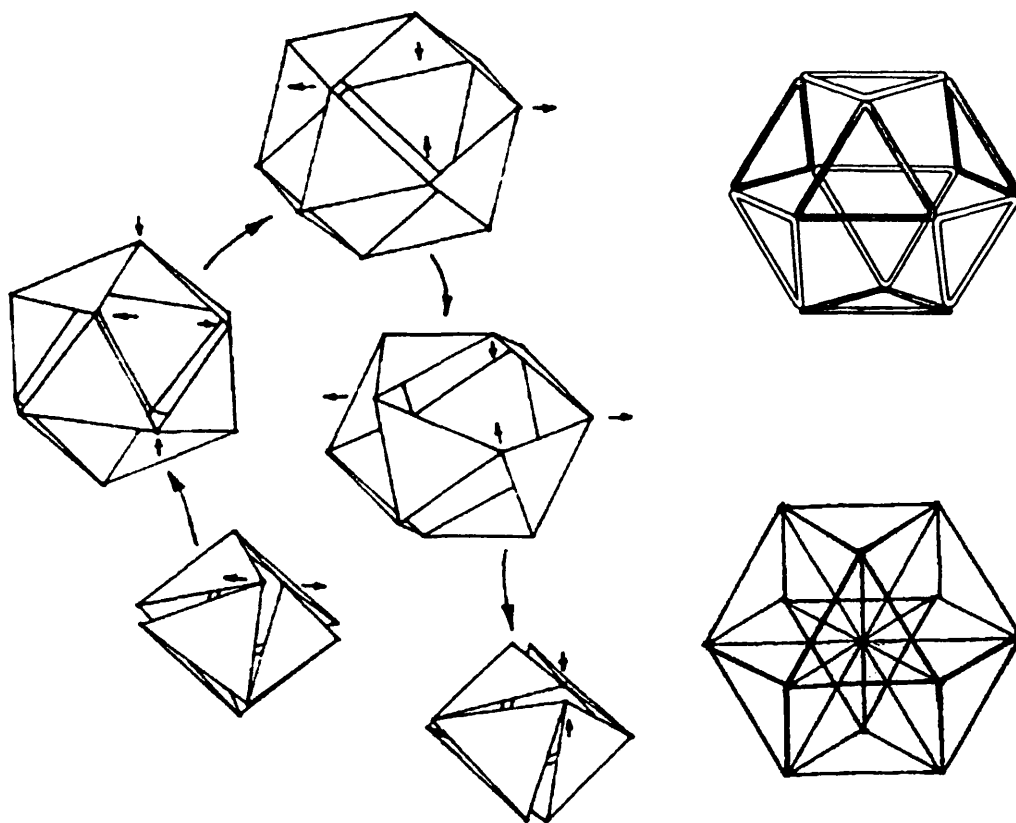


Figure 1.5: Jitterbug transformations (left), Jitterbug model (top right),
Isotropic vector equilibrium (bottom right).

The similarities between geodesic domes and tensegrities are due to the way forces are distributed and transmitted within these structures; however, similarities can often be deduced through purely geometrical arguments. For example, the tensegrity icosahedron (Figure 1.6) may be derived from the jitterbug transformation (Figure 1.5) through a simple “*formfinding*,” process described by Burkhardt (Burkhardt, 2008).

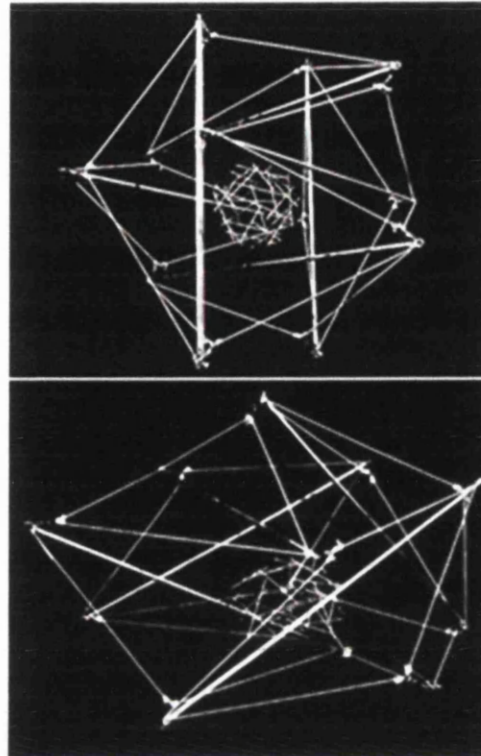
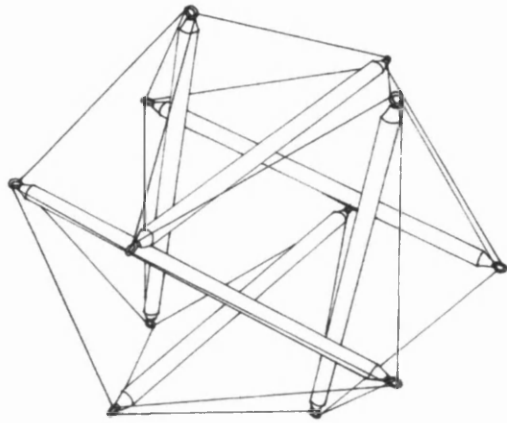


Figure 1.6: Tensegrity icosahedron model (above). Nucleated tensegrity cell model (top, right), mechanism showing how the nucleus flattens and polarizes to base when it attaches and spreads on a substrate, just like living cells (bottom, right) (Ingber, 2011(2)).

Note that the cuboctahedron corresponds to the polyhedron defined by the network of tendons of the tensegrity icosahedron, when the struts of the latter are shortened until the distance between the parallel struts matches their length. In this configuration the quadrilaterals in which the struts are nested become squares, however, the structure is no longer prestressable and is unstable. The formfinding process, which corresponds exactly to the Jitterbug transformation, aims to find a stable configuration for the tensegrity by varying the strut length, while keeping the tendons fixed in length. In Figure 1.5 the location of a typical strut is indicated by a pair of small outward-pointing arrows. When the strut length is a maximum the structure is in its self-stable, prestressable configuration which corresponds to the tensegrity icosahedron.

Further evidence for the prevalence of geodesic structures in nature has been found in the molecular structures of crystals and many other inorganic substances (Ingber, Landau, 2012), but most notably in the discovery of a new class of carbon compounds, that were later named fullerenes. In 1985, Harold Kroto, Robert Curl, Richard Smalley and others at Rice University,

discovered C_{60} during experiments aimed at understanding the mechanisms by which long-chain molecules are formed in interstellar space (Kroto et al., 1985). This remarkably stable molecule consisting of 60 carbon atoms had the structure of a truncated icosahedron and was aptly named the Buckminsterfullerene (C_{60}) (Figure 1.7). Shortly after, a whole class of carbon molecules were discovered named fullerenes, which had the same basic structure as geodesic domes. Spherical fullerenes, also called buckyballs, were also found to be prevalent in nature (Rietmeijer, 2006). Cylindrical fullerenes, also called carbon nanotubes, are one of the strongest tensile materials known to man (Figure 1.7).

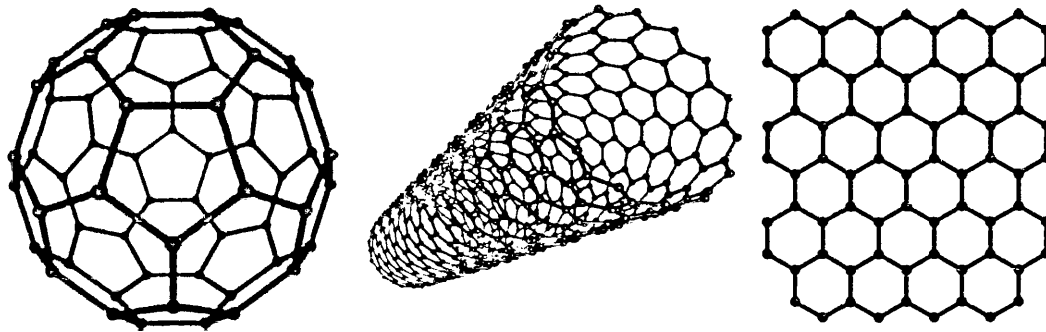


Figure 1.7: Buckminsterfullerene (left), Carbon nanotube (middle), and Graphene (right) molecular structures.

1.4 The nature of tensegrity geodesic spheres

Despite numerous examples to suggest that tensegrity principles and geodesic forms in particular are the basis for a hierarchical structure, to be found in nature (Ingber and Landau, 2012), in order to interpret Fuller's claim, that "*all geodesic domes are tensegrity structures,*" it is useful to appeal directly to structural principles. Although it was suggested at first that there may be some problem with the basic definition of tensegrity, it was later realised that Fuller's and Motro's definitions are consistent provided the following statement, by Fuller can be proved.

"Tensegrity geodesic spheres do what they do because they have the properties of hydraulically or pneumatically inflated structures." (794.01 (Fuller, 1975))

A possible mechanism that could be used to explain this principle of geodesic domes was first recognised by the engineer and inventor, Sir Barnes Wallis. The geodetic construction, pioneered by Wallis, was partly inspired by stressed-skin construction, which was at that time at the forefront of lightweight aircraft construction technology (*Flight*, 1936). Wallis set out to

develop a new construction method which combined the advantages of the stressed skin with that of skeletal structures. In the geodetic airframe, the basic framework was composed of curved members running diagonally, to follow the lines of greatest stress along the spiralling geodesic curves of the surface of the fuselage. Wallis' structures were unique at the time as they used the tendency of slender compression struts to deflect laterally under load to great structural advantage, whereas in conventional structures this tendency had always been viewed as a disadvantage. In an edition of Flight magazine published in 1936, Wallis explains the basic structural principles of his geodetic construction.

In the conventional girder fuselage construction a typical structural unit is composed of a rectangular frame, braced by diagonal cables or tie-rods as shown in Figure 1.8. The bay ABCD, is shown to deform from a rectangle or square into the rhomboid shown by the dotted lines as a result of the application of a torsional load. Assume that an alternative structural arrangement is proposed, in which two curved members are used for the diagonals AC and BD. Under torsional load, each member by itself is very unsuited for the purpose of bracing.

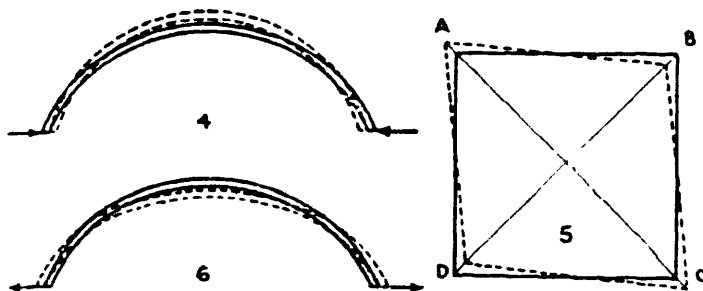


Figure 1.8:
Deflection of curved members under compressive (4) and tensile loads (6). Distortion of braced rectangular bay under torsional loads (5).

Figure 1.8 illustrates how the curved members will tend to deflect under load. The basic mechanism by which the geodetic structure achieves exceptional torsional resistance is achieved through what is described as *"balancing tension against compression"*. As Wallis explains,

"If I anchor the centres of the two (members) together they will tend to oppose each other. The compression member cannot bow because the centre of the tension member holds it down, and the tension member cannot straighten out because the compression member wants to bow and holds up the centre of the tension member. There, in short, you have the explanation of the geodetic construction." (Flight, 1936)

By making one diagonal work against the other, the bending loads in them were found to reduce almost to zero, and very light sections could be used for the members. By reducing the pitch of

the geodesics the most efficient use of geodetic construction was achieved (Figure 1.9). Minimal additional framework was required, although a typical fuselage required four additional longerons in order to take the bending loads. The geodetic or diagonal members resisted the torsion.

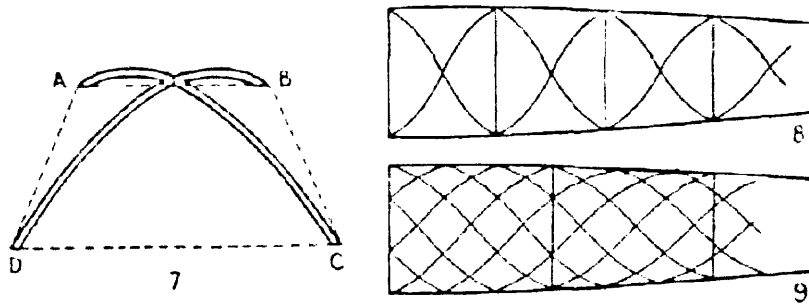


Figure 1.9: Balancing tension against compression. Rectangular bay braced by curved members joined at their centres (7), the simplest application to a fuselage (8), and multiplication of geodesics leads to reduction in number of hoops and weight reductions (9).

Clearly, Wallis' principle of "*balancing tension against compression*," is synonymous with the principles of tensegrity i.e. "*continuous tension, discontinuous compression*." The geodetic structures are consistent with Motro's definition of tensegrity, since the tensioned components surround the compressed components pulling them back towards the central axis, from which they are trying to escape, radially outwards.

The same concept may readily be applied to geodesic domes. The geodesic domes popularised by Fuller in the 1950's were fully triangulated geodesic structures constructed from a three way grid of geodesic curves. Any distortions in the surface of the spherical dome would be resisted by similar mechanisms as described above. It can then be confirmed that geodesic spheres do share certain characteristics with hydraulically or pneumatically inflated structures.

In order to qualify this theory of geodesic tensegrity spheres further it is useful to compare with an established theory; the spherical shell analogy for a geodesic dome (Makowski, 1984). In a certain sense, these two theories overlap; a spherical shell is essentially a pneumatically inflated structure with equalised internal and external air pressures. The pressure differential and thickness of the shell determine the domes structural characteristics. Hence, geodesic domes behave like pneumatic structures to some degree. Since pressurised spherical shells are tensile structures and not prone to the buckling instability phenomenon which are a well known feature of thin walled spherical shells, it would clearly be structurally advantageous to design

and build geodesic domes which behave more like pneumatic structures. Identifying the relevant design parameters involved are important both for development of the theory and applications.

The generalisation of Wallis' theory of geodetic construction to geodesic domes helps to explain how tensegrity principles are involved in resisting shear strains in the domes spherical surface. To understand how similar mechanical principles may be involved in resisting normal strains, Fuller offers the following explanation:

"One of the impressive behavioural characteristics of tensegrity spheres, witnessed at low frequencies, is that when any two islanded struts 180 degrees apart around the sphere are pulled outwardly from one another, the whole sphere expands symmetrically. When the same two 180-degrees-apart struts are pushed toward one another, the whole sphere contracts symmetrically. When the polar pulling apart or pushing together ceases, the tensegrity sphere assumes a radius halfway between the radii of the most pullingly expandable and pushingly contractable conditions; that is, it will rest in equilibrium." (794.22 (Fuller, 1975))

"At the low-frequency, push-pull, contraction-expansion susceptible state, tensegrity spheres act like basketballs. Bouncing them against the floor makes them contract locally, after which they spring back powerfully to their original shape, which impels them back against gravity. Geodesic spheres are in strict physical fact true pneumatic structures with a discrete number of oppositely paired molecules – and their respective atomic colonies – all averagingly aggregated together in the form of the islanded struts instead of being in their invisible gaseous state." (794.24 (Fuller, 1975))

An important distinction is made regarding these phenomena, which is that they are observable at low-frequencies. By frequency is meant the frequency of subdivision; typically the number of equal subdivisions of the arc of a spherical icosahedron or whatever polyhedron is used as the basis for subdivision of a sphere. The points of subdivision are interconnected with a three-way grid of great circle arcs which are used to generate the lattice points of the geodesic dome. In terms of structural principles, the frequency of subdivision is related to the degree of static indeterminacy of the structure: The higher the frequency, the greater the number of redundant members; the lower the frequency, the greater the overall connectivity of the structure. Indeed, most of the large-span geodesic domes built by engineers are known to be highly statically indeterminate structures (Makowski, 1984). Fuller believed that the big domes erected at that time had been many times overbuilt and recommended a safety factor of 2:1 as adopted by the

aeronautical industry as opposed to safety factors of 5 or 6:1 that were reported to have been used in the building of large-span domes (Fuller, 1975). As Fuller explains:

"The greater the safety factor, the greater the redundancy and less the freedom of load distribution." (794.05 (Fuller, 1975))

Nevertheless, Fuller's point was not supported by evidence. Even at the time of writing, the collapse of large-span braced domes which had not been built to the highest safety standards were well known to engineers from the early 1960's (Soare, 1984). In 1963 a large-span lamella dome built in Bucharest, which had a diameter of 93.5m and a rise of 19.1m failed catastrophically, only 17 months after its erection, resulting in complete dome reversal. The dome collapsed in a snow storm while loaded asymmetrically with snow. A number of contributing factors to the local failure and eventual collapse of the dome have been identified (Soare, 1984). The most significant reasons for the collapse were that the degree of asymmetry and local intensity of loading had not been anticipated in the engineering analysis of the structure.

Fuller's observations only go as far as showing that under highly symmetric or basic loading conditions, geodesic domes can have the remarkable properties ascribed to pneumatic structures. It does not follow that under pathological, highly asymmetric loading scenarios the structural characteristics of the dome would remain essentially the same. The complexity of the external load could be as important as the degree of static indeterminacy in determining the essential nature of the structure: whether it remains resilient like a tensile structure or buckles and implodes like a thin spherical shell.

Fuller's and Wallis' interpretations are nevertheless, remarkably similar. Both men sought to combine the advantages of the stressed skin with the use of the material in concentrated form, as the "islanded struts," as oppose to dispersed or spread out form (Fuller, 1975; *Flight*, 1936). The established theory of shell analogies applied to the analysis of stress distribution in braced domes indicates that only the shell thickness and dome dimensions are of interest in analysing the nonlinear response of the spherical shell to various loading conditions (Makowski, 1984; Timoshenko and Woinowsky-Krieger, 1959). The nonlinear effects described by Wallis and Fuller suggest that for geodesic domes there are more important structural principles involved which are not accounted for by this theory. An alternative theory based on the analogy between geodesic domes and pneumatically inflated structures could form the basis for developing new analytical and numerical methods for the nonlinear analysis of geodesic domes.

1.5 Applications

Buckminster Fullers' aim in developing geodesic domes was to bring about inexpensive mass-producible structures. Despite the great popularity of geodesic domes during the 50's and 60's and the great number of architects, engineers and industrialists who supported Fullers campaign, the vision of a new era in which the whole of humanity would benefit from the mass-production of prefabricated geodesic domes, was far from the reality of the late 20th century. Fuller's most ambitious predictions, including visions of an entire city contained within a single spherical dome, have been viewed sceptically by structural engineers. It has been often said of Fuller that he was an eccentric futurist, and an iconoclast. Some of his more sensationalist proposals reflect the currents of thought and artistic trends of his time and help to explain why his ideas gained such popularity. However, it would appear that geodesic domes simply fell out of fashion during the 1980's. The true potential of the geodesic dome remained unrealised as social, economic and political influences seemed to have an overwhelming influence on technological developments (Makowski, 1984).

Today, there is a greater potential for architects and engineers to develop lightweight, efficient structures in light of the impending climate crisis and need to address the global challenges faced by humanity. Fuller's design philosophy and heuristic approach are more relevant today than ever. In laying the foundations for his "design science," Fuller can be viewed as a man before his time. Although his insights into the complexity of structure and patterns to be found in nature have inspired new technologies including bioengineering, nanotechnology and adaptive structures, the development of geodesic domes is still viewed as one of his greatest contributions. The future development of geodesic domes may not be exactly as Fuller envisaged, however, there is no reason why the impact on humanity of geodesic domes and tensegrity structures should not live up to and even exceed expectations. As Fuller surmised, by employing force distributions similar to those found in atoms, molecules and crystals, geodesic domes would turn out to be the lightest, strongest and cheapest constructions ever made. Although the architecture of the cell cytoskeleton and structure of fullerene molecules had not been discovered and elucidated until after Fullers death, these structures and models now form the basis for nature inspired structures and further transformations of the geodesic dome.

Whereas the focus in early developments of geodesic domes was to build as big as possible, today there is a greater emphasis on structural efficiency and functionality. Although a spherical dome is the most efficient shape for enclosing a given volume in space, for terrestrial applications, large spherical domes are generally not the most efficient structures, where the

ground surface area enclosed is of greater importance than the enclosed volume and internal supports are permitted. For this reason, modular structures and clusters or arrays of spherical domes are seen as the lightweight, efficient structures of the future. Cabled structures, which have received greater attention and been developed further by tensegrity scientists and engineers in recent years, will no doubt be of great importance in the future development of lightweight structures. By combining cabled structures with the structural geometry of geodesic domes, innovative, lightweight dome structures are currently being developed. Adaptive and deployable structures are also at the forefront of technology, combining efficient robotics and control systems with lightweight tensegrity structures, in order to achieve greater functionality and adaptability for specialist applications.

The long history of greenhouse farming and its prominence in technologically advanced nations, such as the Netherlands, is testament to the longevity and sustainability of the greenhouse system in agriculture, which operates on the principle of maximising use of natural resources and is continually evolving in line with technological developments. By developing highly efficient, deployable, modular structures, which are assembled on site to support a suspended array of spherical domes arranged in a regular pattern, large areas of arable farmland may be transformed into highly productive greenhouse farms. Extending the range of applications for greenhouse technology would help to solve problems of food security and contribute towards bringing an end to world hunger. In restoring vegetative ecosystems, reducing surface albedo and increasing the uptake of atmospheric carbon through plant photosynthesis, greenhouse technology could play a key role in restoring the atmosphere and biosphere by mimicking and enhancing the function of plants.

Modern, commercial greenhouse systems are integrated with innovative energy solutions, which improve energy efficiency, increase productivity and extend the range of climates in which greenhouse farming can successfully be applied. The semi-closed greenhouse, developed for the European climate, uses thermal energy storage technology in order to reduce energy consumption by providing a renewable source of heating in the winter months which is replenished in the summer from heat extracted from the greenhouse through mechanical cooling. Although ventilation is the most effective method of cooling in a semi-closed greenhouse, when the cooling load is lower, the internal atmospheric conditions may be controlled precisely using mechanical cooling and dehumidification, which considerably improves productivity. By maximising the capacity of a greenhouse as a solar collector it has been shown that significant amounts of renewable energy can be harvested from a fully-closed

or semi-closed greenhouse, which is simultaneously used for food production. The technology still requires further development in order to make energy producing greenhouses a commercially viable, sustainable alternative.

The potential of using greenhouse technology to bring life to the desert is finally being realised and applied on a large scale through innovative sustainable development projects, such as the Sahara Forest project, which continues to attract significant support and interest internationally. In the seawater greenhouse, optimal conditions for plant growth are achieved by driving warm, ambient air through a seawater saturated permeable mesh in order to achieve evaporative cooling and humidification. As a system which was inspired by the hydrological cycle, warm humidified air is finally passed through a condenser in order to produce fresh water, before being released back into the environment. The moisture which remains in this air may then be absorbed by hardy desert plants which grow around the greenhouse, thus, natural vegetative ecosystems may be restored. Arrays of seawater greenhouses are integrated with high power solar collectors which supply renewable electricity for powering the greenhouse systems.

1.6 Aims and Objectives

The focus of this dissertation is the structural design and optimisation of geodesic tensegrity structures. New design principles are elucidated through use of abstract reasoning, geometrical thinking and the development of innovative design solutions and structural systems. The geometrical, structural and theoretical principles, pertaining to all aspects of the design and analysis process are presented in detail.

In Chapters 2 and 6 an iterative design process is presented, culminating in the development of a new class of geodesic tensegrity structures. A number of practical tensegrity structures and structural systems are developed, focusing on a range of design applications related to agriculture and sustainable development.

In Chapters 3, 4 and 5 specialised computational and analytical methods are presented and developed further in order to perform the engineering design optimisation of tensegrity structures and geodesic tensegrity domes in particular. Extensive use is made of structural mechanics principles and mathematically rigorous derivations are included where appropriate. Emphasis is placed on the development of computational methods, efficient code

implementations and algorithms and a unified approach to tackling all analysis problems related to the design of tensegrity structures in general.

In Chapter 2, design intentions are presented by reviewing the design and development of geodesic domes and developing the intrinsic geometry for a new type of geodesic tensegrity dome structure. Methods for designing dome structures which cluster in 2-dimensions to form arrays of dome modules are presented. The analytical geometry and transformations required to generate the dome geometry is derived from first principles. Basic designs for deployable, modular structures are presented and the stability characteristics of various realisations are considered. Prototype designs and models are formulated for further development and analysis.

In Chapter 3, analytical models and computational matrix methods are developed for the structural analysis and optimisation of geodesic tensegrity domes. Computational methods based on the Singular Value Decomposition of the equilibrium matrix enable stress and deflection patterns to be determined for a general loading, while simultaneously giving access to any information of a static, kinematic or static/kinematic nature required for further analysis of tensegrity structures (Pellegrino, 1993). The choice of an appropriate coordinate system, suitable sets of variables for each structural element in the assembly, the setting up of the corresponding element equilibrium matrices, and the assemblage of these matrices into a global equilibrium matrix are presented in a general form. Illustrative examples include both planar reticulated assemblies and 3-dimensional frameworks corresponding to a dome substructure.

Chapter 4 reviews and explains the techniques used to analyse symmetric structures subject to a general loading. The full symmetry properties of a structure may be exploited using group representation theory in order to systematically simplify structural analysis (Kangwai et al. 1999). A general method is presented which is suitable for the analysis of dome structures with a high degree of symmetry. An application of the method is illustrated using simplified example structures which have the same symmetry properties as many of the dome structure designs presented in the report. By transforming the equilibrium matrix of a structure into a block diagonal form and applying substructuring techniques, it is clearly shown how the symmetry subspace methods may be integrated with the computational methods presented in Chapter 3 in order to systematically simplify the structural analysis. A novel approach is introduced in order to develop more efficient implementations of the symmetry subspace methods in computer code. By choosing an appropriate initial coordinate system for representing external variables, and developing new algorithms it is shown how it would be possible to simplify the

transformations to symmetry adapted variables significantly and generate more efficient implementations of the symmetry subspace methods.

Chapter 5 is concerned with the analysis of internal mechanisms and prestress states for tensegrity structures. After a brief review of rigidity theory, analytical methods are presented which may be applied in the structural analysis of statically and kinematically indeterminate assemblies, which poses higher order infinitesimal mechanisms. By analysing the equilibrium matrix of a structure in its reference configuration associated with the prestressed geometry, it is possible to determine the precise nature of the internal mechanisms of a structure and the stiffening effect due to prestressing (Pellegrino and Calladine, 1986; Pellegrino, 1990; Vassart et al. 2000). A general method is presented for simplifying the prestress optimisation problem for tensegrity structures by exploiting the symmetry of a structure (Yuan and Dong, 2003). The optimisation of cable prestress forces may then be carried out using linear programming techniques.

Chapter 6 presents the design and development of double-layer geodesic tensegrity domes and grids. A range of 3-dimensional tensegrity modules are presented and applied in the design of geodesic tensegrity dome structures. Methods of clustering domes and the design of dome honeycombs are developed further. Efficient dome modules and structural systems are developed for practical applications. By developing tensegrity modules based on designs by the artist, Kenneth Snelson, a new type of modular structural system is presented from which a range of geodesic tensegrity structures are derived.

In solving many of the practical problems which have hindered the development of tensegrity structures in applications and developing a range of efficient modular structures inspired by nature, geodesic tensegrity structures have the potential to revolutionise the world and set a benchmark in the design of lightweight, efficient structures.

1.7 References

Bauersfeld-Zeis-Jena, n.d. {Online image}. Retrieved September 2015 from http://simplydifferently.org/Geodesic_Dome_Notes?page=1.

Burkhardt, R. (2008). *A Practical Guide to Tensegrity Design*, 2nd edit. Cambridge, MA.

Edmondson, A.C. (1987). *A Fuller Explanation: The Synergetic Geometry of R. Buckminster Fuller*. Birkhauser: Boston.

Flight: the Aircraft Engineer and Airships (1936). January 16 edit., pp. 67-68. Flight International.

Fuller, R.B. and Applewhite, E.J. (1975). *Synergetics: Explorations in the Geometry of Thinking*. Macmillan Publishing Co. Inc.

Fuller, R.B. (1979). *Synergetics Portfolio*. R. Buckminster Fuller & Lim Chong Keat. Publishers: Philadelphia & Singapore.

Gough, M. (1998). In the Laboratory of Constructivism: Karl loganson's Cold Structures. *October*, 84, pp. 90-117.

Ingber, D.E., Madri, J.A. and Jameison, J.D. (1981). Role of basal lamina in the neoplastic disorganisation of tissue architecture. *Proc. Nat. Acad. Sci. USA*, 78, pp. 3901-3905.

Ingber, D.E. and Jameison, J.D. (1982). Tumour formation and malignant invasion: role of basal lamina. *Tumour Invasion and Metastasis* [ed. Liotta L.A. and Hart, I.R.], pp. 335-357. Martinus Nijhoff: The Hague, Netherlands.

Ingber, D. E. and Jameison, J.D. (1985). Cells as tensegrity structures: architectural regulation of histodifferentiation by physical forces transducer over basement membrane. *Gene Expression During Normal and Malignant Differentiation* [ed. Anderson, L.C., Gahmberg, C.G. and Ekblom P.], pp. 13-32. Academic Press: Orlando, FL.

Ingber, D.E. (1993). Cellular tensegrity: Defining new rules of biological design that govern the cytoskeleton. *J. Cell. Sci.* 104, pp. 613-627.

Ingber, D.E. (2011). 1: *Geodesic form in the tensed cytoskeleton of a human cell* {Online image}. Retrieved September 2015 from <http://www.scholarpedia.org/article/Tensegrity>.

- Ingber, D.E. (2011). 2: *Spherical tensegrity cell model* {Online image}. Retrieved September 2015 from <http://www.scholarpedia.org/article/Tensegrity>.
- Ingber, D.E. and Landau, M. (2012). Tensegrity. *Scholarpedia*, 7(2):8344
- Kangwai, R.D., Guest, S.D and Pellegrino, S. (1999) An introduction to the analysis of symmetric structures. *Computers and Structures*, 71, pp. 671-688.
- Kenner, H. (1976). Geodesic math and how to use it. University of California Press, Berkeley.
- Kroto, H.W., Heath, J.R., O'Brien, S.C., Curl, R.F., and Smalley R.E. (1985). C60: Buckminsterfullerene. *Nature*, 318, pp. 162-163.
- Makowski, Z.S. (1984). Analysis, design and construction of braced domes. Granada Publishing.
- Motro, R. (1990). Tensegrity Systems and Geodesic Domes. *International Journal of Space Structures* [Special Issue on Geodesic Forms, ed. T.Tarnai], 5(3), pp. 343-354.
- Motro, R. (2006). Tensegrity: Structural Systems of the Future. Butterworth-Heinemann.
- Ohsaki, M. and Zhang, J. (2006). Stability conditions of prestressed pin-jointed structures. *International Journal of Non-Linear Mechanics*, 41, pp 1109-1117.
- Pellegrino, S. and Calladine, C.R. (1986) Matrix analysis of statically and kinematically indeterminate frameworks. *Int. J. Solids Structures*, 22(4), pp. 409-428.
- Pellegrino, S. (1990). Analysis of Prestressed Mechanisms. *Int. J. Solids Structures*, 26(12), pp. 1329-1350.
- Pellegrino, S. (1993). Structural computations with the singular value decomposition of the equilibrium matrix. *Int. J. Solids Structures*, 30(21), pp. 3025-3035.
- Rietmeijer, F.J.M. (2006). Natural Fullerenes and Related Structures of Elemental Carbon. *Developments in Fullerene Science*, 6. Springer, Netherlands.
- SL 1 Wooden Lattice framework*, n.d. {Online image} Retrieved September 2015 from <http://www.blimpinfo.com/history-2/this-mo-in-hist-ian/schutte-lanz/>.
- Snelson, K.D. (1965). *Wood X-Column* {Online image} Retrieved September 2015 from <http://www.tensegriteit.nl/e-xmodule.html>.

Snelson, K. D. (1965). *U.S. Patent No. 3,169,611*. Washington, DC: U.S. Patent and Trademark Office.

Snelson, K.D (2012). *What is tensegrity?*{Online} Retrieved September 2015 from <http://kennethsnelson.net/faq/>.

Soare, M.V. (1984) Investigation of the collapse of a large-span braced dome. *Analysis, design and construction of braced domes* [ed. Makowski, Z.S.], Granada Publishing. pp 161-174.

Stamenovic, D., Fredberg J.J., Wang N., Butler J.P., and Ingber D.E. (1996). A microstructural approach to cytoskeletal mechanics based on tensegrity. *J. Theor. Biol.* 181, pp. 125-136.

Timoshenko, S. and Woinowsky-Krieger, S. (1959). *Theory of plates and shells*. McGraw-Hill.

Tensegridad.es, 2010. *Proto-tensegrity by loganson* {Online image} Retrieved September 2015 from https://commons.wikimedia.org/wiki/File:Proto-Tensegrity_by_loganson.jpg.

Vassart, N., Laporte, R. and Motro, R. (2000). Determination of mechanism's order for kinematically and statically indetermined systems. *Int. J. Solids Structures*, 37, pp. 3807-3839.

Yuan, X.F. and Dong, S.L. (2003). Integral feasible prestress of cable domes. *Computers Structures*, 81, pp. 2111-2119.

Chapter 2 Geodesic Tensegrity Domes and Dome Honeycomb Structures

2.1 Geodesic domes

The geometry and topology of a geodesic dome is most easily described with reference to atlases or local charts. In fact, the geometry of the geodesic dome is obtained from a central projection of the points of a regular tessellation on the surface of a chart onto the surface of a sphere – the inverse process of projecting onto a map or chart. These local charts have a specific geometry and orientation with respect to the spherical surface. They correspond to polygons, which form the faces of a regular (or semi-regular) polyhedron with centre coincident with the centre of projection and the spherical surface is precisely the circumsphere of the polyhedron. This process of generating the dome geometry is known as “*geodesic subdivision*,” and results in the minimal distortion in the chart lattice structure, which is usually composed of equilateral triangles. The “*frequency*,” of subdivision refers to the number of lattice triangles which span an edge of the chart or polygon.

The inverse process of generating a chart or atlas for displaying globe topography is known as the “*Fuller projection*,” and was developed by Fuller in the 1950's. The “*Dymaxion Air-Ocean map*,” (Figure 2.1) is rendered by juxtaposing a grid of triangles on the globe and transferring the data to corresponding triangles on an unfolded icosahedron.

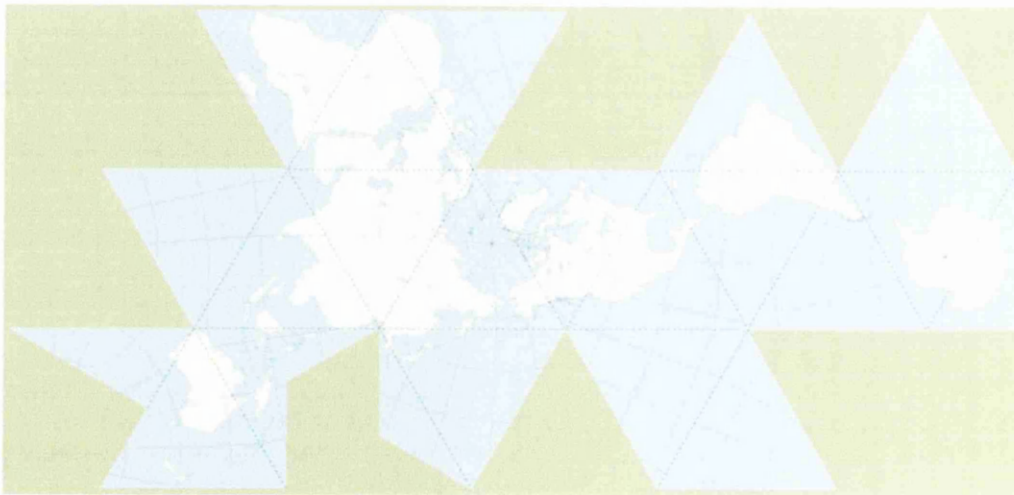


Figure 2.1: Map of the world in an unfolded Fuller projection, also known as the “*Dymaxion Air-Ocean World map*.” 1954 final version for an icosahedron, with folding lines. (Gaba, 2009)

The structural advantages of the geodesic dome are due to the relatively uniform stress distribution under normal loading conditions combined with the most efficient use of material. The use of a three way grid composed of almost uniform, equilateral triangles has proved to be a structurally efficient type of bracing for a wide range of skeletal structures. A defining feature of the geodesic dome is that the structural members follow geodesic curves which automatically generate the shortest possible lengths of members over the dome surface. For an arbitrary surface, a geodesic is similarly defined as the shortest path between any two points on the surface.

A particular feature of the geodesic subdivision is that within an area of the dome surface represented by a particular chart all the lattice nodes will lay along geodesic curves since the corresponding chart lattice is composed of intersecting straight lines. However, on the boundary between two charts or edge of the generating polyhedron it is generally not true that the continuity of the geodesic curves will be preserved. In other words, the direction of the geodesic curves will change as they traverse the chart boundary.

In the early development of geodesic domes, great circle systems were employed to preserve the continuity of geodesic curves in the structure as much as possible. For example, Buckminster Fuller proposed that although the maximum number of equilateral spherical triangles into which a sphere can be divided is 20, for domes of larger spans the medians of the spherical triangles could be used to generate an additional 15 great circles. The practice of using great circle systems to derive dome geometry was later abandoned in favour of geodesic subdivision or "*breakdown*," systems. In practice, it was found that a truly geodesic type of bracing based on great circles was insufficient for large span domes as it resulted in a lack of uniformity in the dome geometry and lead to an excessive slenderness ratio for certain members. (Makowski, 1984)

Compared with other types of braced dome a geodesic dome will usually give good stress distribution and shell stiffness combined with a relatively high strength to weight ratio. Using computer analysis, it can be shown that the relative strength of the geodesic dome can be between 1.4 to 2 times higher than that of other commonly used types of braced dome with comparable geometries (Richter, 1984). Despite this, geodesic domes are subject to the same problems of instability as other types of braced dome and also have a number of disadvantages, usually related to the cost of manufacture and construction.

The use of geodesic subdivision means that when a lattice of equilateral triangles is projected from a chart onto the sphere the resulting triangles will no longer be equilateral and the dome members will show slight variations in their lengths. Although these distortions are generally quite small, it is clear that as the frequency of subdivision or size of the dome increases, the number of different components and types of connector will also increase. This is reflected in the final price of the dome and for larger spans geodesic domes are often significantly more expensive than other dome structures.

A number of improvements were made to the geodesic dome over the second half of the 20th century. Various structural systems were developed which enabled mass production of geodesic domes with relatively few different types of components and high speed erection techniques. Among these systems appeared early geodesic tensegrity domes such as those developed by Jeffery Lindsay for his "*shell truss*," system, (Makowski, 1984) and stressed-skin geodesic domes, such as the Kaiser Aluminium stressed-skin domes developed by Donald Richter. Double-layer geodesic domes were developed in order to extend the span of a geodesic dome beyond that which was possible using a conventional single layer grid. A classic example of a large scale double-layer geodesic dome is the "*Montreal Biosphere*," built for the Expo '67, United States pavilion in 1967 (Figure 2.2). This three-quarter sphere, 76m in diameter, contains some 6000 connectors and 24000 tubular steel members arranged into a double-layer space grid.

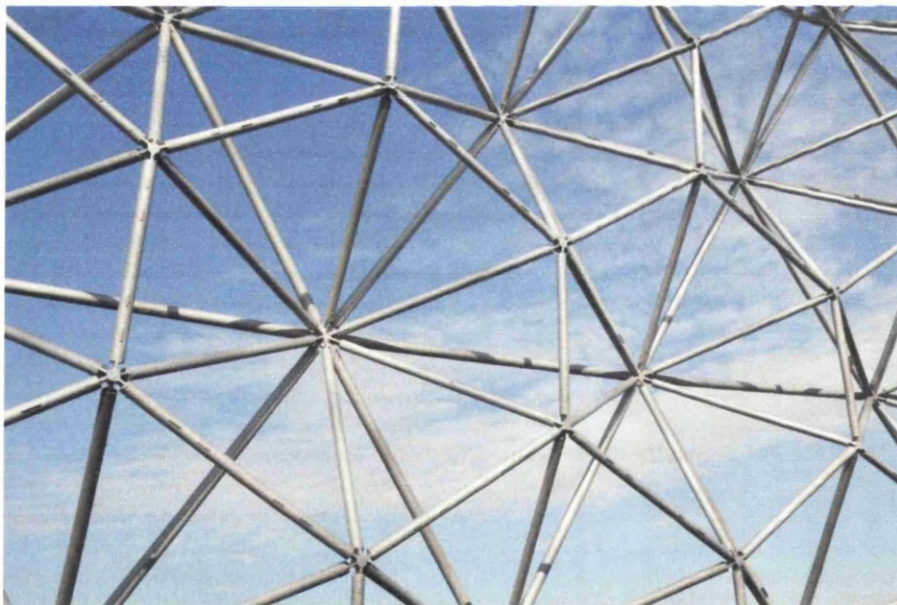


Figure 2.2: Structural details of the Montreal Biosphere as seen from the inside. (Butcher, 2011)

From 1964 onwards stressed-skin aluminium domes were developed further at Temcor Co. by D. Richter and his colleagues. One of the most successful developments in Temcor aluminium domes was the *"PolyFrame"* dome, which featured a lattice modified geodesic geometry using a single layer grid and an aluminium panel system which functioned as a tension membrane. To act as a membrane, the panel edge joints were clamped with a patented interlocking batten system that both sealed and held the edges. In 1982, Temcor built an aluminium dome with a record span of 126m and height of 40m to house the H-4 flying boat, otherwise known as the *"Spruce Goose."* The dome was designed by Don Richter and featured a single layer geodesic pattern based on the PolyFrame system. In 2006, Temcor built a similar dome, as a limestone storage facility for the Taiwan Cement Co. in Ho Ping, which is today the world's largest aluminium dome, measuring 136m in diameter.

2.2 Planar tessellations and linkages

The chart lattice structure, as obtained from a Fuller projection, is the most accurate 2D representation of the local geometry of a geodesic dome. Therefore, it is quite natural to consider planar tessellations which correspond to the chart lattice structure to represent the local dome structure away from chart boundaries and when the frequency of subdivision is relatively large. By manipulating the chart lattice structure and considering the basic structural characteristics of the corresponding dome lattice, the disadvantages of a purely triangular lattice are easily identified and alternative geometries are proposed for further investigation.

The chart structure for most geodesic domes built to date is based on the regular triangular tessellation. Consider an arbitrary linkage composed of a network of triangular trusses, which is topologically equivalent to a region of the planar triangular tessellation. The degree of static indeterminacy, s of the linkage satisfies the following inequality,

$$s \geq b - N \quad (2.1.1)$$

where b is the total number of bars and N is the number of degrees of freedom of the linkage. Equation (2.1.1) is an exact equality when the equilibrium matrix is of full rank and $b \geq N$ (see 3.1 for further details).

By considering a region of the triangular tessellation bounded by a hexagon, the analysis of the corresponding linkage will show that even when the number of triangles within the region is relatively small the linkage will be statically indeterminate. It also can be observed that as the

size of the hexagon increases the degree of static indeterminacy will increase quite rapidly. From this basic analysis it can be inferred that in general, geodesic domes are highly statically indeterminate structures except when the frequency of subdivision is quite small.

Although the geodesic dome may have many redundant elements, this was not generally seen as a disadvantage by dome engineers as the over bracing contributed to the stiffness of the structure. On the other hand, it has been recognised, in more advanced dome designs, that maintaining a purely triangular lattice structure is not necessarily the most efficient way of stiffening a dome structure. For example, in a double layer dome structure, such as that of the Montreal Biosphere, the inner layer of the dome is based purely on a hexagonal lattice structure, whereas the shell truss system developed by J. Lindsay is based on a trihexagonal lattice. Yet, these structural systems do not differ markedly from the triangular lattice structure. In the double layer dome the outer layer is still a triangular lattice and the hexagons in the trihexagonal lattice structure are braced by cables which lie in the triangular lattice planes. By taking a more radical step away from purely triangular lattice structures and introducing tensegrity principles it has been discovered that not only can more efficient dome structures be developed but also the cost disadvantages associated with geodesic dome structures can be reduced significantly.

A fundamental question in the theory of planar tensegrities is the following;

“What is the most efficient substructure that can be introduced to stabilise a flexible hexagonal lattice linkage?”

Here, reintroducing the triangular lattice, by stabilising each hexagon individually is the least efficient option, when all that is required is the stability of the structure as a whole. As a first step we might consider introducing some triangular bracing about particular nodes in such a way that hexagons become isolated within the structure as shown in Figure 2.3. Assuming the structure is composed of rigid pin-jointed bars, the bars within each triangular truss can be removed as they are now redundant elements (Figure 2.4). The structure is still unstable as the hexagonal and rectangular trusses are unstable. Hence, there are two possible alternatives; either to stabilise the hexagons or to stabilise the rectangles.

Notice that in the case only the hexagons are stabilised the structure is reduced to a unique, single degree of freedom mechanism, which can be visualised as a system of gears. In other words, the structure has a single mode of inextensional deformation, which corresponds to all the hexagons rotating in one direction simultaneously, to synchronise with the triangles, which

simultaneously rotate in the opposite direction. In addition, the relative rotation of the hexagons and triangles induce large amplitude uniform contractions and expansions in the lattice structure. Such flexible structures or materials could be developed further for applications in, for example, wave energy converters or pneumatically inflated structures.

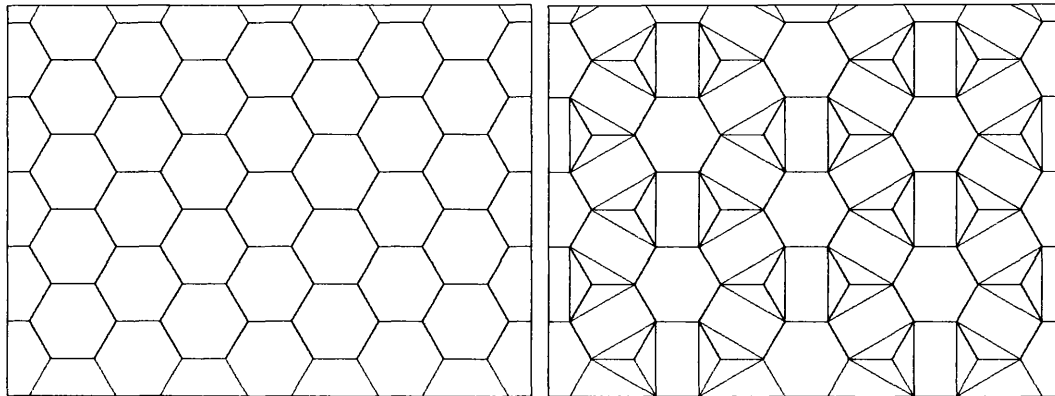


Figure 2.3: Hexagonal tessellation or lattice (left). Hexagonal lattice linkage with triangular bracing introduced (right).

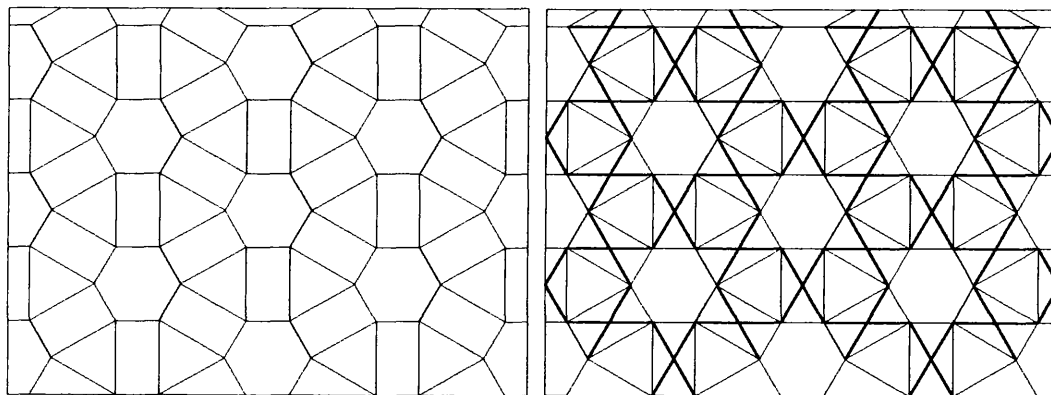


Figure 2.4: Unstable, open lattice linkage composed of hexagons and rectangles (left). The "*X-trihexagonal*," stable planar lattice structure composed of tensegric "*X-modules*" (right).

Alternatively, the stability of the rectangles in this planar lattice structure is sufficient to ensure the stability of the structure as a whole. By introducing the tensegrity "*X-module*," all members that were previously bars are converted into cables and the only struts in the structure are the diagonals which cross each rectangle. This structure is shown on the right of Figure 2.4 and represents the starting point for further development of geodesic tensegrity domes, which is the main topic of this dissertation project. This planar lattice structure will be called the

"*X-trihexagonal lattice*," or simply the "*X-trihex lattice*," due to the obvious similarity with the trihexagonal tessellation.

Although perfectly stable as a planar truss system, as a space truss the X-trihex lattice structure behaves as an under-constrained cabled structure and is only stable under tension. Additional bracing is required to stabilise the structure when used to form the primary structure of a dome or similar convex shape. Even when additional bracing is added the X-trihex lattice does not form a particularly efficient dome structure. It is unsuitable for larger span domes since the potential for snap through buckling is far greater than for a fully triangulated geodesic dome. More generally, simple X-modules do not have sufficient torsional rigidity and the abrupt changes in strut orientation do not allow for an efficient transfer of forces. Nevertheless, the geometry of the X-trihex lattice is a perfectly valid starting point for developing more efficient dome structures.

The derivation of the basic geometry of a geodesic dome by geodesic subdivision of the face of an octahedron is illustrated in Figure 2.5. It can be clearly seen that the use of the X-trihex chart lattice structure in place of a triangular lattice results in a dome structure which is unstable. However, it is fairly easy to stabilise this structure by adding a few additional tensegrity trusses and cables.

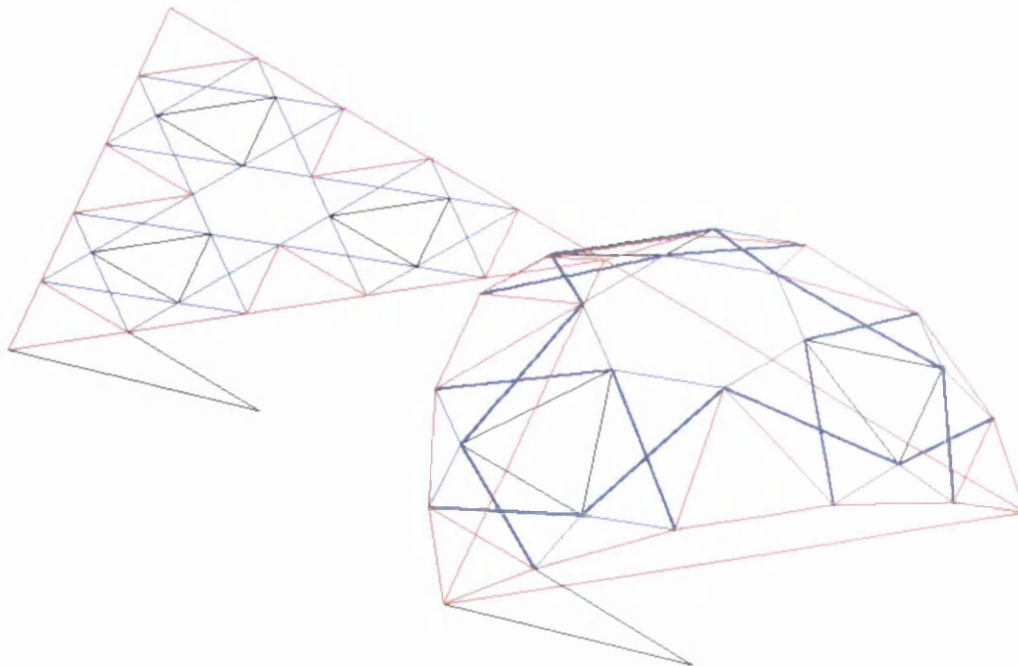


Figure 2.5: Geodesic subdivision of an octahedron face using the X-trihex lattice structure, illustrating the Fuller projection and X-trihex dome structure.

Initially we may consider replacing the X-modules in the basic lattice structure by more rigid 3-dimensional tensegrity modules to form a double layer tensegrity dome, mainly composed of cables. Additional cable sets would be added to form the outer and inner layers of the double layer dome and tensegrity trusses would form a matrix between the outer and inner layers to create a rigid, prestressable, lightweight space structure. Yet more efficient dome structures may be derived through modifying the basic X-trihex lattice structure using simple geometric transformations. A series of alternative lattice patterns have been proposed from which specific dome structural systems have been further developed.

Another structural characteristic of the X-trihex lattice linkage is that it has relatively few simple mechanisms which can be exploited in order to develop foldable or deployable structures. A viable folding mode or mechanism for a dome is one which results in a partial collapse of the dome but which preserves the symmetry of the dome as much as possible. Since several alternative mechanisms could be active simultaneously it is necessary to introduce additional bracing and support to the structure to enable it to fold in a safe and controlled manner. In addition, structural joints must be specially designed for strut to strut connections to allow for the relative rotation of structural units. Even though such joints may be more expensive than conventional rigid joints, the savings in construction costs and time taken to deploy or collapse a structure are believed to outweigh the additional engineering costs, when the intended purpose of the dome is as a temporary, mobile structure.

The design of a possible joint geometry, to allow for relative rotation of X-modules in a foldable X-trihex dome structure is illustrated in Figure 2.6. A cone is fixed to the end of each strut at an offset angle, such that the cone centreline is aligned with the cable along a particular fold line. The cones are lashed together using a high tensile strength material as cordage in such a way that the relative rotation of the two struts does not induce frictional rubbing of the binding or cause it to loosen. Essentially, the joint is designed to rotate as a smooth gear, with the cones as bearing surfaces and the cordage (typically steel strings) acting as a pulley under tension. This joint system ensures that the mechanism will not lock up as the struts rotate through a large angle. Details of joint mechanism design will not be discussed further as part of the preliminary investigation presented in this report.

Actively adaptive structures are a more recent development in the field of lightweight structures, and are designed to exploit the structures folding mechanisms in order to change the structural configuration, using simple actuators, in response to changes in external loading conditions. It can be shown that a symmetry preserving folding of a X-trihex lattice dome results in a more

structurally favourable configuration, allowing a dome to collapse safely, avoiding catastrophic failure or dynamic snap through buckling. More applicable in the development of large span braced domes are adaptive systems which actively control internal stresses as in, for example, stressed-skin domes or tensegrity domes. In principle, the distribution of internal stresses or self-stress could be manipulated using simple linear actuators, changing the stiffness of the structure in response to changing static or dynamic loads, without involving complex folding mechanisms or a change in the geometric configuration of the structure.

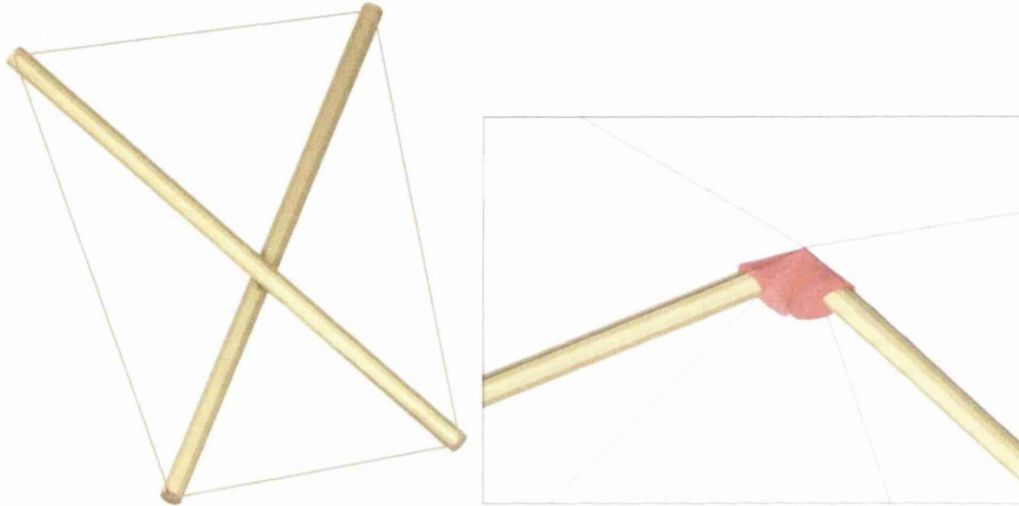


Figure 2.6: The "X-module" tensegrity (left), with details of strut to strut connections in the foldable, X-trihex dome (right).

Currently, adaptive systems are too costly and unreliable for widespread use in large scale structures; however, there is a particular instance where some degree of adaptability in a structure can be used to great advantage. For instance, when it is desired to assemble a modular structural system over uneven terrain, the ability to adjust the geometric configuration of each module to some extent to fit the given topology is another advantage of a foldable structure.

The folding mechanisms being considered here are based purely on the inextensional mechanisms of the X-trihex lattice linkage which result from out of plane motions. It can be clearly seen that any out of plane motions of the lattice nodes which originally coincide with the vertices of a hexagon will immediately destroy the six-fold symmetry of that hexagon. The maximum symmetry of the original structure we could hope to preserve during folding corresponds to 3-fold rotational symmetry about the centre of each hexagon. During folding, the structure will contract considerably, each hexagon shrinking to a singularity, while the X-

modules close about each triangle to form triangular prisms. The final configuration of the structure, when projected onto the plane, corresponds exactly to the regular triangular tessellation. The overall linear extents of a region of the lattice will reduce by a half during folding and this corresponds to an area reduction of 75%. The advantage of using this type of structural system for a foldable dome is that the volume reduction will be even greater and a very compact, rigid structure is obtained in the folded configuration (Figure 2.7).

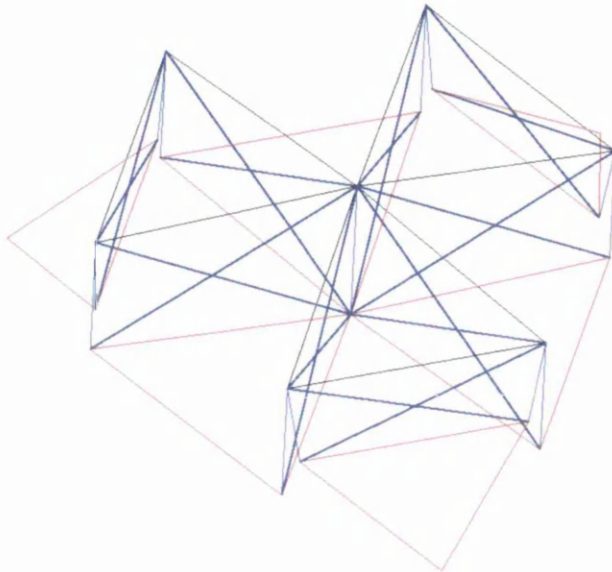


Figure 2.7:
Illustration of the dome of Fig. 2.5 in its folded configuration. When the structure is locked in this configuration, by introducing additional cables or lashings, an extremely stiff, mobile structure is obtained.

The geometrical configuration changes which occur during folding are closely related to polytope operations of contraction and expansion applied to the lattice structure. The X-trihex configuration represents the structure in its most expanded state. By contracting certain subsets of rectangles within the X-trihex structure; by reducing to zero the length of the shortest sides of each rectangle within the subsets; a sequence of alternative lattice structures is obtained which correspond to inhomogeneous, semi-regular planar tessellations (Figure 2.8). The limit of this sequence of contraction operations occurs when all rectangles have been converted to line segments, in which case the resulting structure corresponds to the regular triangular tessellation. Although the start and end points of this sequence of contraction or expansion operations correspond to a re-configuration of the X-trihex lattice linkage, in general, the inhomogeneous, transitional lattice structures obtained from the polytope operations cannot be similarly obtained from a re-configuration of the original structure and represent entirely new lattice structures. These alternative lattice structures will have markedly different structural characteristics from the original X-trihex lattice and in general, the rigidity and compactness of the structure will increase through contraction operations. It can be readily appreciated that the

inhomogeneous, semi-regular planar tessellations could be particularly useful in developing further the geometry of double-layer, geodesic tensegrity domes.

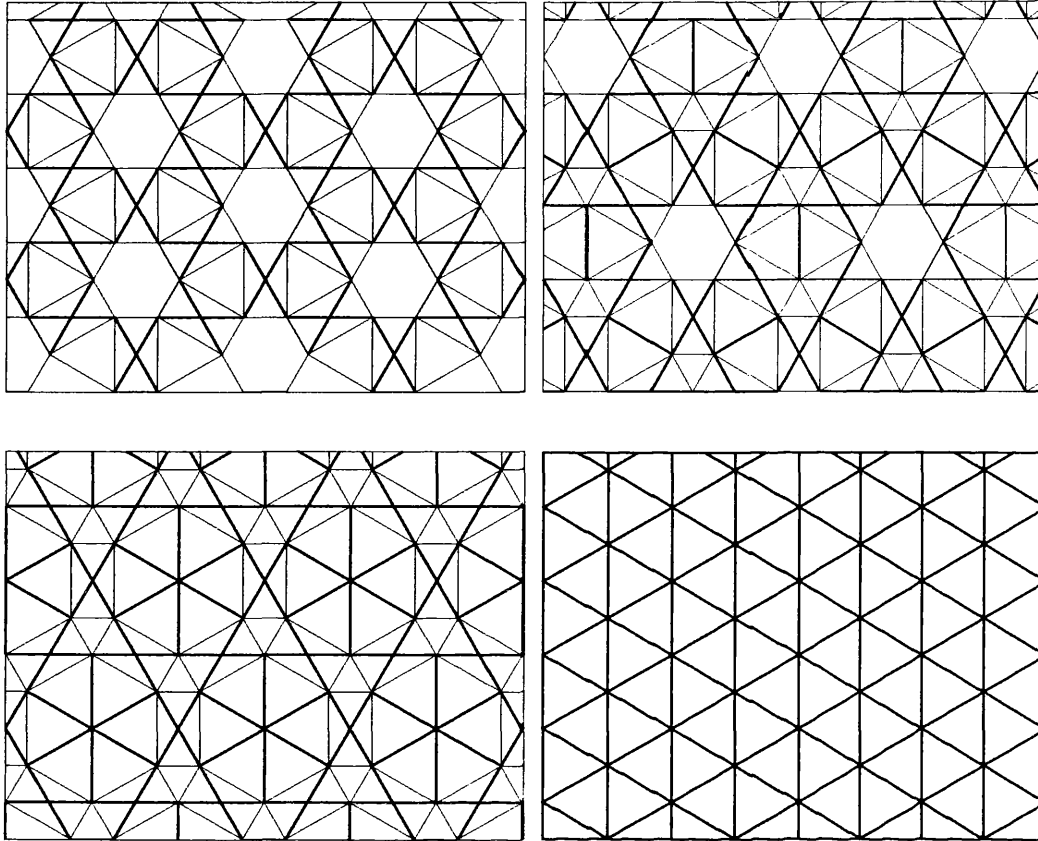


Figure 2.8: Polytope contraction operations applied to the X-trihex lattice (top, left), yield a sequence of inhomogeneous semi-regular tessellations (top, right and bottom, left), which finally converge to the regular triangular lattice (bottom, right).

2.3 Geodesic breakdown systems and coordinate geometry

2.3.1 *Breakdown systems*

Regular polyhedra, such as the octahedron or icosahedron are commonly used as generator volumes in deriving the geometry of a geodesic dome. The isocahedron dome is the most popular type of geodesic dome although other types of polyhedra, such as those obtained from the isocahedron or dodecahedron families, are commonly used for larger domes. (Motro, 1984)

It is possible to execute a geodesic breakdown on any polyhedron provided the non-triangular faces are first converted into triangles by introducing new vertices at the centre of each polygon to form pyramids. These vertices are obtained by projecting the central points of each non-triangular polygon onto the circumscribed sphere of the corresponding polyhedron. The polyhedron is then used to define the centre of projection, radius of the circumsphere and basic geometry of the charts or faces used for projecting lattice points. In general, each chart will form a planar triangular face and the breakdown system used will be the same on every chart.

For a geodesic dome, the chart lattice structure is simply obtained by subdividing each chart into a network of triangles according to the rules of the particular breakdown system being employed. A breakdown system is defined by the frequency of subdivision and is classified either "*Class I*," or "*Class II*," according to the following definition.

Class I subdivision

Lattice points are placed uniformly along the edges of the chart and divide each edge into a number of segments equal to the frequency of subdivision. Dividing lines, parallel to the chart edges, pass through the lattice points to form a regular triangular lattice which includes the chart edges.

Class II subdivision

A Class II subdivision is obtained by a simple transformation of a Class I triangular lattice. Additional lattice points are added at the centre of each triangle of the original lattice and a new set of dividing lines are introduced which coincide with the medians of the original lattice triangles. The dividing lines of the original lattice are discarded and the chart edges are not included. The frequency of the Class II subdivision is twice that of the original Class I lattice from which it is obtained.

The symbol 'v' is used to denote frequency. For example, a frequency of subdivision of 6 is abbreviated as '6v'. Figure 2.9 illustrates how a 6v Class II subdivision may be obtained from a 3v Class I subdivision according to the Class II subdivision rule. Clearly, only even numbered frequencies can be obtained with a Class II subdivision, whereas any frequency is possible for Class I.

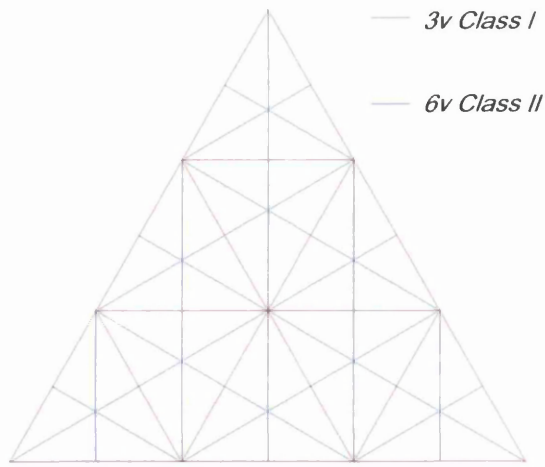


Figure 2.9:

Superposition of 3v Class I and 6v Class II subdivision of a triangular chart.

The geometric transformation of a Class I lattice used to generate a Class II subdivision can easily be generalised in order to obtain a higher frequency Class I lattice from a Class II lattice. By applying this transformation iteratively, a sequence of lattice patterns can be generated from an original, starting lattice. At each iteration step, the general transformation applied to the current lattice, obtained from the previous step, is described as follows:

Additional lattice points are added at the centre of each triangle of the current lattice and a new set of dividing lines are introduced which coincide with the medians of the current lattice triangles. The dividing lines of the current lattice are discarded.

The sequence of lattice patterns so obtained will alternate between Class I and Class II subdivisions and at every other step of the iteration process the frequency of subdivision goes up by a factor of 3. For example, if the original lattice is Class I and frequency X , the lattice obtained at the k^{th} step of the algorithm will have the following properties. If $k = 2n$ where $n \in \mathbb{N}$, the breakdown system obtained after the k^{th} iteration step will be Class I and frequency $Y = 3^n X$, else if $k = 2n - 1$, the lattice will be transformed to a Class II lattice with frequency $Z = (2 \times 3^{(n-1)})X$, after the k^{th} iteration step.

The sequences of lattice patterns generated by this transformation group are particularly useful for deriving the geometry of alternative chart lattice patterns, such as the X-trihex lattice and closely related patterns. It can be shown that a typical breakdown system for an X-trihex pattern can be derived as a combination of triangular lattice patterns obtained from several different standard breakdown systems. Figure 2.10 illustrates the simple process of constructing an X-trihex pattern from a sequence of triangular lattice patterns. The X-trihex lattice contains subsets of points and segments from each of the triangular lattices and the sequence of

triangular lattices are precisely those obtained from the first few iterations of the above transformation with 5v Class I as the original, starting lattice.

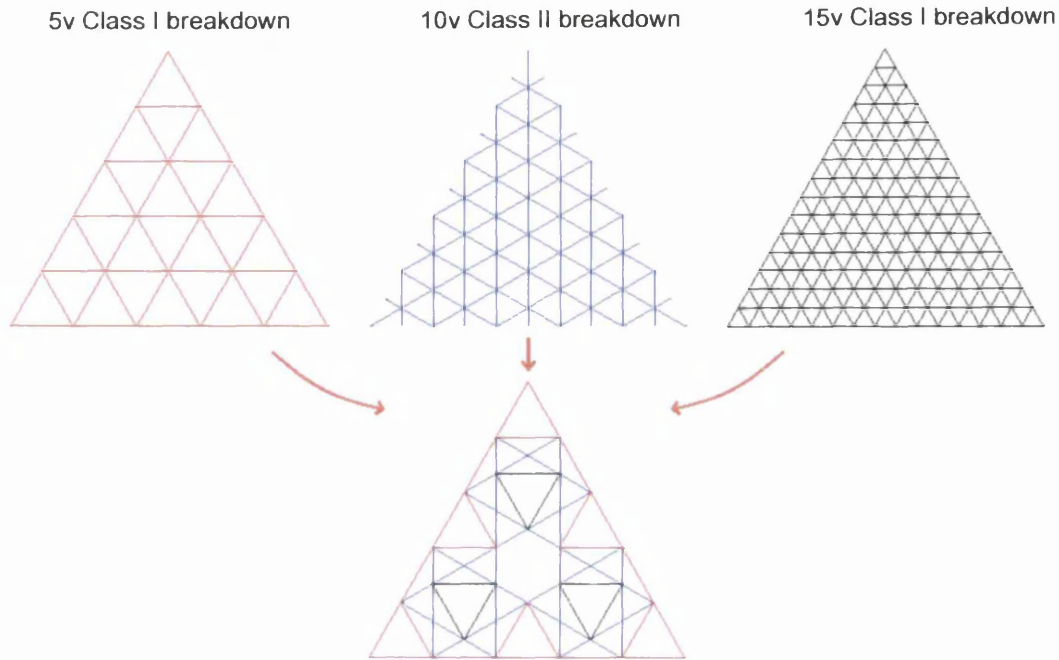


Figure 2.10: Constructing an X-trihex chart lattice from triangular lattices

The multi-frequency nature of the X-trihex chart lattice structure can be further exploited to create hybrid lattice structures composed of X-modules of varying scales. These patterns can be drawn in a similar way by combining points and segments from a larger sequence of triangular lattices derived from a common base lattice through iterative geometric transformations. Hybrid X-trihex lattice structures such as the one shown in Figure 2.11, enable a degree of flexibility in dome structure design that could not be achieved using conventional

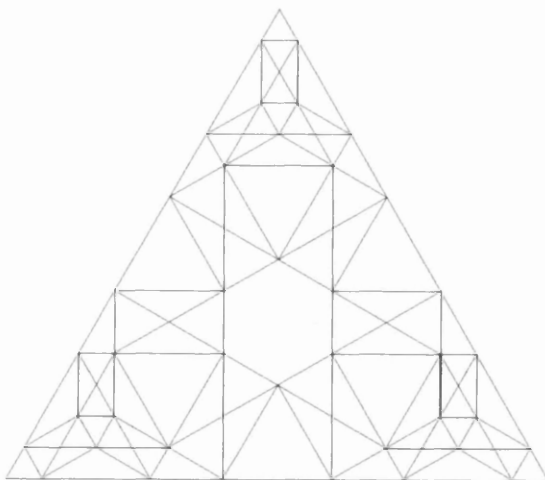


Figure 2.11:

Hybrid X-trihex chart lattice.

The lattice geometry can be derived as a multi-frequency breakdown using 5v Class I, 10v Class II, 15v Class I and 30v Class II triangular lattices.

triangular lattice patterns. This can be used to reduce the variability in strut lengths, characteristic of geodesic domes and to improve the stress distribution and structural characteristics of X-trihex lattice type domes. The improved lattice structure of Fig. 2.11 has been used as a basis for developing more practical dome structures.

2.3.2 *Coordinate systems and transformation equations*

The mapping which corresponds to a central projection of chart lattice points onto the circumsphere to obtain dome nodal coordinates is now described more fully with reference to suitable coordinate systems.

For simplicity, the octahedron is chosen as a generator for the geodesic subdivision and each chart corresponds to a triangular face of the octahedron. More general results may similarly be derived when an arbitrary polyhedron is chosen as a generator volume.

Let r denote the circumradius of the octahedron i.e. the distance from the centre of the octahedron to one of its vertices. Define a standard Cartesian coordinate system with origin at the centre of the octahedron, such that the positive z-axis passes through the centre of a face of the octahedron and one of the vertices of this triangular face lies in the x-z plane. The face centre height h of the octahedron is given by

$$h^2 = \frac{1}{3}r^2. \quad (2.2.1)$$

Hence, the particular face with z-axis as normal lies in the plane $z = \frac{1}{\sqrt{3}}r$. On this face, the x-y coordinates are used to define local coordinates on the chart lattice. The 5v Class I chart lattice is shown with local coordinate axis indicated in Figure 2.12.

A different set of local coordinates are used to define points on the surface of the circumsphere. In order to exploit rotational symmetry and simplify the projective mapping as much as possible, cylindrical polar coordinates, (ρ, θ, z) are chosen with azimuth angle, θ measured clockwise from the x-axis, to represent an arbitrary point on the sphere. Since the radius r of the sphere is given and $z > 0$ on the region of the sphere represented by the local chart, two coordinates are sufficient to uniquely define a point on the sphere. Hence, the local coordinates for lattice points on the sphere correspond to the planar, polar coordinates, (ρ, θ) .

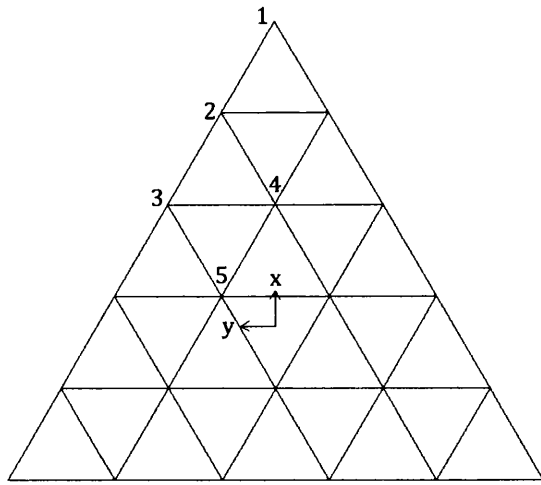


Figure 2.12:
5v Class I chart lattice, indicating local coordinates and node numbers.

The mapping from the (x, y) coordinates, representing chart lattice points, to corresponding points on the sphere, represented by polar coordinates (ρ, θ) , is defined, by the central projection from the centre of the octahedron, as follows.

Let (a_i, b_i) denote the (x, y) coordinates of chart lattice point i and (ρ_i, θ_i) denote the polar coordinates of the corresponding lattice point on the sphere. As the azimuth angles of all lattice points are invariant under a central projection,

$$\theta_i = \tan^{-1}\left(\frac{b_i}{a_i}\right) \quad (2.2.2)$$

If ρ'_i and r'_i denote radial distances from the face-centre and body-centre of the octahedron, respectively, to chart lattice point i , then the projected coordinate ρ_i is given by (similarity of triangles),

$$\rho_i = \frac{r}{r'_i} \rho'_i \quad (2.2.3)$$

Substituting for r'_i in terms of ρ'_i (by Pythagoras theorem), the following result is obtained;

$$\rho_i = \frac{r}{\sqrt{\left(\frac{h}{\rho'_i}\right)^2 + 1}} \quad (2.2.4)$$

In terms of the coordinates (a_i, b_i)

$$\left(\frac{h}{\rho'_i}\right)^2 = \frac{r^2}{3(a_i^2 + b_i^2)} \quad (2.2.5)$$

The original and transformed nodal coordinates for the mapping $(a_i, b_i) \rightarrow (\rho_i, \theta_i)$ may be derived in an analytic form and are displayed in Table 2.1 for the chart lattice points $i = 1, \dots, 5$, labelled in Figure 2.12, of the standard 5v Class I lattice.

Node index i	a_i/r	b_i/r	ρ_i/r	$\tan \theta_i$
1	$\sqrt{\frac{2}{3}}$	0	$\sqrt{\frac{2}{3}}$	0
2	$\frac{7}{5\sqrt{6}}$	$\frac{1}{5\sqrt{2}}$	$\sqrt{\frac{26}{51}}$	$\frac{\sqrt{3}}{7}$
3	$\frac{4}{5\sqrt{6}}$	$\frac{\sqrt{2}}{5}$	$\sqrt{\frac{14}{39}}$	$\frac{\sqrt{3}}{2}$
4	$\frac{4}{5\sqrt{6}}$	0	$\sqrt{\frac{8}{33}}$	0
5	$\frac{1}{5\sqrt{6}}$	$\frac{1}{5\sqrt{2}}$	$\sqrt{\frac{2}{27}}$	$\sqrt{3}$

Having obtained the coordinates of the 5 reference nodes, the coordinates of the remaining nodes are obtained from reflection or rotational symmetry. Two coordinates are sufficient to fix the position of a node on the sphere, since the radial distance from the origin is already given. Hence, the z-coordinates and Cartesian coordinates of all nodes can easily be obtained.

The coordinate transformations for a basic X-trihex chart lattice, based on a 5v Class I triangular lattice, may similarly be obtained in an analytic form. The transformation from chart geometry to dome geometry is illustrated in Figure 2.13. In this case only 4 lattice points need to be transformed from the chart as the remaining dome coordinates can be automatically generated from the 6-fold rotational symmetry and reflection planes of the dome. The coordinate transformations for the 4 nodes labelled in figure 2.13 are calculated in analytic form in Table 2.2.

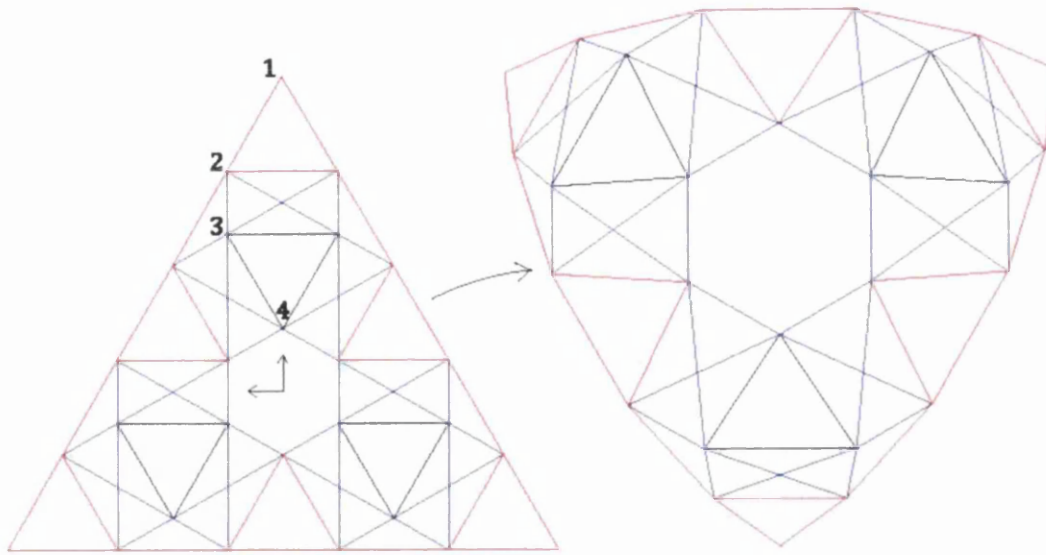


Figure 2.13: X-trihex chart lattice transformation under octahedral centre projection.

Node index i	a_i/r	b_i/r	ρ_i/r	$\tan \theta_i$
1	$\sqrt{\frac{2}{3}}$	0	$\sqrt{\frac{2}{3}}$	0
2	$\frac{7}{5\sqrt{6}}$	$\frac{1}{5\sqrt{2}}$	$\sqrt{\frac{26}{51}}$	$\frac{\sqrt{3}}{7}$
3	$\frac{1}{\sqrt{6}}$	$\frac{1}{5\sqrt{2}}$	$\sqrt{\frac{14}{39}}$	$\frac{\sqrt{3}}{5}$
4	$\frac{\sqrt{2}}{5\sqrt{3}}$	0	$\sqrt{\frac{2}{27}}$	0

The transformations from polar coordinates (ρ, θ) to 3-dimensional Cartesian coordinates (x, y, z) , for points on the circumsphere, are given by the following equations:

$$\frac{x}{r} = \frac{\rho}{r} \cos \theta \quad (2.2.6)$$

$$\frac{y}{r} = \frac{\rho}{r} \sin \theta \quad (2.2.7)$$

$$\frac{z}{r} = \sqrt{1 - \left(\frac{\rho}{r}\right)^2} \quad (2.2.8)$$

Measuring distances and angles

The distance between two points A and B in 3-dimensional space with cylindrical polar coordinates $\{\rho_A, \theta_A, z_A\}$ and $\{\rho_B, \theta_B, z_B\}$ may be measured using the following distance function;

$$d(A, B) = \sqrt{(z_A - z_B)^2 + \rho_A^2 + \rho_B^2 - 2\rho_A\rho_B(\sin \theta_A \sin \theta_B + \cos \theta_A \cos \theta_B)} \quad (2.2.9)$$

By substituting expressions for z_A and z_B for points A, B on the sphere in terms of ρ_A and ρ_B and expanding the brackets, the distance function on the sphere, S in terms of Cartesian coordinates may be expressed as,

$$d(A, B)_{on\ S} = \sqrt{2(r^2 - z_A z_B - y_A y_B - x_A x_B)} \quad (2.2.10)$$

Given a triangle of arbitrary shape, size and orientation with vertices at points A, B and C , the angle $\gamma = \angle BAC$, between the two sides meeting at A is given by the law of cosines as,

$$\cos \gamma = \frac{d(A, B)^2 + d(A, C)^2 - d(B, C)^2}{2d(A, B)d(A, C)} \quad (2.2.11)$$

Using the measures of distance and angle between the nodes of the dome model the lengths of struts, cables and the dimensions of planar faces of the dome can easily be obtained.

2.4 Basic geometry of the honeycomb dome

The geometries of the dome models considered here are all based on the geodesic subdivision of a face of the octahedron using various chart lattice types and breakdown frequencies. The advantages of using the octahedron as a generator volume as oppose to the more commonly used types of polyhedra for geodesic dome breakdown systems, such as the icosahedron or dodecahedron, are briefly described as follows.

Firstly, the octahedron is an important member of the family of space-filling polyhedra and is more suitable as a basis for deriving systems for clustering domes than are other commonly used types of polyhedra. The truncated octahedron is used as a basis for the simplest of space-filling systems and, apart from the cube, is the only polyhedron known to fill space alone. As the octahedron and truncated octahedron are so closely related, geodesic subdivision of these polyhedra often generate indistinguishable dome geometries. For example, it is known that a 3v Class I subdivision of an octahedron is identical to a 1v Class I subdivision of a truncated

octahedron. The truncated octahedron has been used as a basis for developing modular structures and systems for clustering triangulated domes, such as the "*Min-a-Max*," dome system (Pearce, 1984).

The system for clustering domes described in what follows is simpler than those based on space-filling polyhedra. In this case the advantage of the octahedron is simply that a dome with a reasonable span to rise ratio can be developed from the projection of a single face of the octahedron onto its circumsphere. The disadvantage of the higher level of distortion of the underlying chart lattice under central projection can often be overcome by considering modified chart lattice structures and developing double layer tensegrity dome systems, which allow a greater degree of flexibility in determining strut lengths. Another advantage of developing dome geometry from geodesic subdivision of a single polygonal face is that the radius of the sphere used to obtain the centre of projection can be chosen arbitrarily and need not correspond to the circumradius of a polyhedron. For simplicity, only breakdown systems based on the octahedron geometry will be discussed further.

Clustering patterns for domes in two dimensions are based on the regular or semi-regular tessellations, described previously. The hexagonal "*honeycomb*," is one of the most archetypal tiling patterns that can be seen in a variety of natural constructs and materials. The hexagonal tessellation is the preferred pattern to use for clustering domes over a planar surface and has a number of structural advantages over alternative clustering patterns. It is necessary to identify suitable truncation planes and modify the geometry of a geodesic dome to allow it to be used for clustering. The steps in developing the geometry of a dome to obtain a dome with a hexagonal profile that is suitable for clustering are now described in more detail.

As an example, the structure of the dome model shown in Fig. 2.13 and 2.5 is developed further. The symmetry substructure for this dome is shown on the left of Fig. 2.14 in plan view. The first modification to the basic dome structure is to introduce the tetrahedron shown on the right of Fig. 2.14. Nodes 2 and 6 and the foundation node, f of this particular dome are required to coincide with the vertices of a tetrahedron. Note that the edge length of the tetrahedron is determined by the length of edge 2-6, which is determined by the geodesic subdivision of the dome, so the only modification required is in the position of the foundation node. The triangle, 1-2-6 lies in a horizontal plane and forms a boundary between the three neighbouring domes and the tetrahedron which supports the structure and is connected to the foundation node.

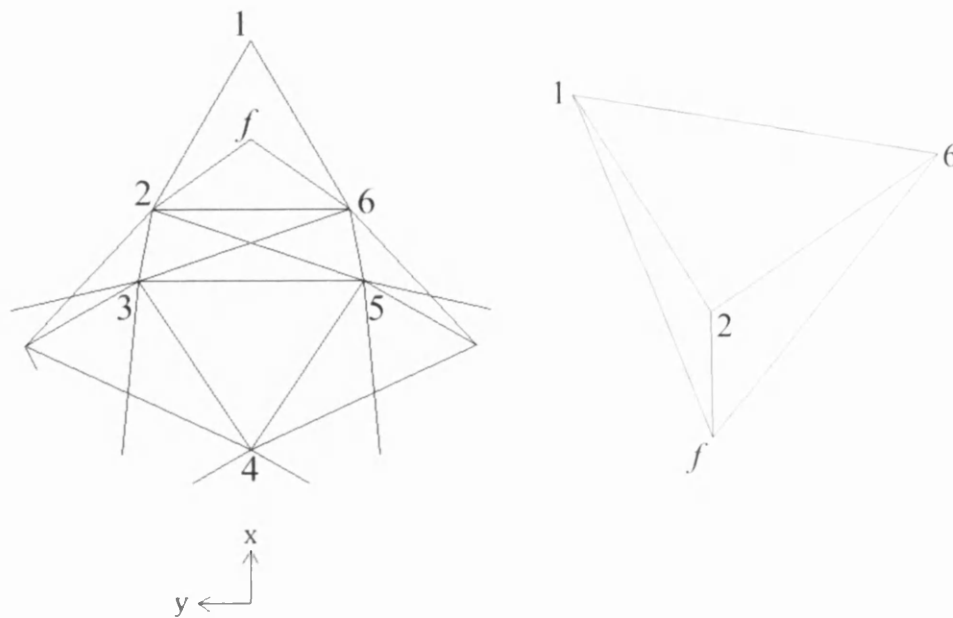


Figure 2.14: Symmetry substructure (right) for the X-trihex dome developed previously with the position of the foundation node, f adjusted to coincide with the vertex of a tetrahedron (left) to enable a dome with a hexagonal profile to be developed for dome clustering in a two dimensions.

It is clear that introducing the tetrahedron ensures that nodes 1, 2 and 6 each lie on the curves of intersection between neighbouring domical surfaces, however, the tetrahedron also has an important function structurally in stabilising the honeycomb structure and the synergy between domes and tetrahedrons results in a remarkably strong, lightweight structural system. Once the coordinates of nodes 2 to 6 are obtained from the geodesic geometry the remaining nodes of the dome model may be obtained by rotating the symmetry substructure about the central axis of the dome by angles of 60° , 120° , 180° , 240° and 300° . The resulting dome structure possesses the full six fold symmetry of the hexagon and when the foundation nodes are included the hexagonal profile of the dome is clearly evident, as shown in Figure 2.15.

The dome structure, represented in Fig. 2.15, illustrates how minor adjustments to the geometry, as obtained from geodesic subdivision, produces a dome with a hexagonal profile, which can be used for clustering in two dimensions. It is still necessary to develop the basic dome structure further and to generate a dome model which can be used for practical applications, since clearly, the dome structure represented in Fig. 2.15 is unstable as a reticulated assembly. Although this dome model can be improved by introducing additional

bracing, it is found that more fundamental changes to the structure are required in order to improve the stress distribution and stability characteristics of the dome.

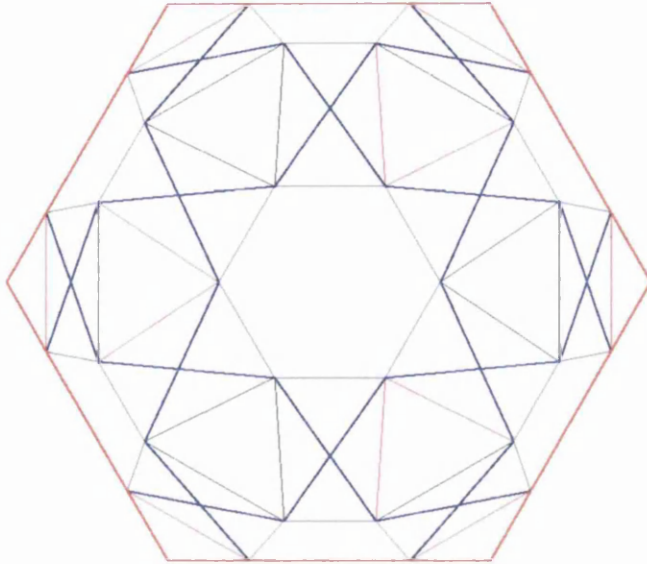


Figure 2.15:

Simplified model of an X-trihex lattice dome, developed for clustering in a hexagonal tiling pattern.

In order to illustrate how the nodal coordinates of the dome of Fig. 2.15 may be obtained analytically, it is convenient to work in the standard Cartesian coordinate system. Using the coordinate transformations (2.6), (2.7) and (2.8) applied to nodes 2, 3 and 4, whose polar coordinate representations are shown in Table 2.2, the following coordinate values are obtained in the global Cartesian coordinate system with origin at the centre of the octahedron (Table 2.3). Note that due to the orientation of the x-y coordinate axis, and symmetry of the structure, as shown in Fig. 2.14, the coordinate values of nodes 5 and 6 are simply obtained by reversing the sign of the y-coordinates of nodes 3 and 2, respectively.

Table 2.3: X-trihex dome global Cartesian coordinates			
Node index i	x_i/r	y_i/r	z_i/r
2	$\frac{7}{2}\sqrt{\frac{2}{51}}$	$\frac{1}{2}\sqrt{\frac{2}{17}}$	$\sqrt{\frac{25}{51}}$
3	$5\sqrt{\frac{1}{78}}$	$\sqrt{\frac{1}{26}}$	$\sqrt{\frac{25}{39}}$
4	$\sqrt{\frac{2}{27}}$	0	$\sqrt{\frac{25}{27}}$

From basic trigonometry it is found that the height, $hTetr$ of the tetrahedron is related to the edge length, $eTetr$ by the following formula;

$$hTetr = \sqrt{\frac{2}{3}} eTetr \quad (2.2.12)$$

Similarly, the inscribed radius, $sTetr$ of a triangular face of the tetrahedron is given by,

$$sTetr = \frac{1}{2\sqrt{3}} eTetr \quad (2.2.13)$$

Since the length of the edge of the tetrahedron is simply given by,

$$eTetr = 2y_2 = \sqrt{\frac{2}{17}} r \quad (2.2.14)$$

the coordinates of the foundation node i.e. the lowest point of the tetrahedron, are easily obtained from the above formulae.

Once the nodal coordinates are obtained for the symmetry element it is straight forward to deduce the overall dimensions of the dome. For example, the dome half-span, P for the dome of Fig. 2.15 is given by,

$$P = x_2 + \frac{1}{2\sqrt{3}} (2y_2) = 4 \sqrt{\frac{2}{51}} r \cong 0.79r \quad (2.2.15)$$

Similarly, the overall height, H is given by

$$H = z_4 - z_2 + hTetr = \left(\sqrt{\frac{25}{27}} - \sqrt{\frac{25}{51}} + \frac{2}{\sqrt{51}} \right) r \cong 0.54r \quad (2.2.16)$$

Finally, the remaining nodal coordinates of the dome are obtained by rotating the symmetry substructure about the centreline of the dome in angular steps of $\pi/3$ radians. The transformations are described analytically in terms of rotation matrices.

Given a particular node, i of the symmetry substructure we assemble the nodal coordinates in a column vector $\{X_i\}$, i.e.

$$\{X_i\} = \begin{Bmatrix} x_i \\ y_i \\ z_i \end{Bmatrix} \quad (2.2.17)$$

The rotation matrix, $[R]$ which pre-multiplies $\{X_i\}$ to apply a counter clockwise rotation about the centreline of the dome to the nodal point, i by an angle of $\pi/3$ radians is given by,

$$[R] = \begin{bmatrix} \cos \frac{\pi}{3} & -\sin \frac{\pi}{3} & 0 \\ \sin \frac{\pi}{3} & \cos \frac{\pi}{3} & 0 \\ 0 & 0 & 1 \end{bmatrix} \quad (2.2.18)$$

$$= \begin{bmatrix} \frac{1}{2} & -\frac{\sqrt{3}}{2} & 0 \\ \frac{\sqrt{3}}{2} & \frac{1}{2} & 0 \\ 0 & 0 & 1 \end{bmatrix}$$

It is convenient to group the nodal coordinate vectors, $\{X_i\}$ of the symmetry substructure in a matrix $[X_{R0}]$, such that the vectors, $\{X_i\}$ form the columns of the matrix $[X_{R0}]$ i.e.

$$[X_{R0}] = [\{X_1\}, \{X_2\}, \dots, \{X_j\}] \quad (2.2.19)$$

and the number of columns, j is equal to the number of nodes of the symmetry substructure.

The nodal coordinates for the entire dome structure may then be conveniently represented by a series of iterative matrices of the following form,

$$[X_{Rk}] = [R]^k [X_{R0}], \quad k = 0, 1, \dots, 5 \quad (2.2.14)$$

Each column of the matrices $[X_{Rk}]$, $k = 0, 1, \dots, 5$, uniquely represents the coordinates of a particular node.

2.4 Dome honeycombs; design concepts and functionality

The basic geometry of a network of dome modules arranged in a honeycomb structure is illustrated in Figure 2.16. The tetrahedrons which form around the points of intersection of three neighbouring domes are seen to be well proportioned and contribute to the overall stiffness of the structure. It may be possible to develop deployable dome modules which exploit simple folding mechanisms similar to those illustrated in Fig. 2.6 and 2.7. As shown in Fig. 2.16 the dome structure of Fig. 2.15 could, in principle be folded into a compact space truss. Exploiting such folding mechanisms could significantly reduce the time and energy required to deploy a dome honeycomb structure over a wide area. There is clearly a wide range of practical

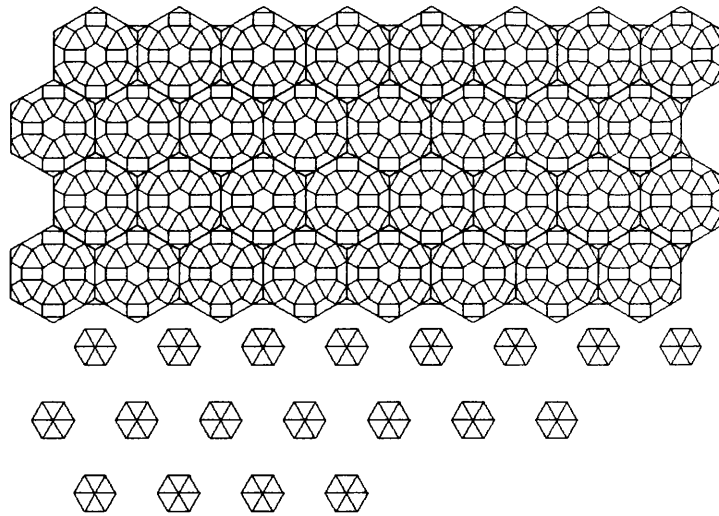


Figure 2.16:

Simplified dome modules assembled in a honeycomb structure. During the folding process each dome is disconnected from the honeycomb and folds inwardly. The bottom three rows show domes in a folded state.

applications for temporary or adaptable structures where the ease with which the structure can be deployed is an important design consideration.

More importantly, the overall cost of the structural system is strongly influenced by the structural efficiency and cost of manufacture. Clearly, the modular nature of the structure results in a significant reduction in the manufacturing costs due to economies of scale. It is usually required to make some compromise between structural efficiency and the ease with which a structure can be deployed. Since structural efficiency is of paramount importance and there are a range of important applications where the structure is only required to be static and need not be redeployed, the focus of the remainder of the report is the development of highly efficient modular structures.

The dome structure, represented in Fig. 2.15 and 2.16 is an example where, through oversimplification, the structural integrity is somewhat diminished in favour of achieving a relatively simple folding mechanism. As is common with all foldable domes of this type the mechanisms used for folding involve multiple degrees of freedom which must be controlled simultaneously. It is conceivable that additional poles could be used to support the structure during the folding operation and a pulley system could be devised to allow the dome to be collapsed manually, in a controlled manner. Even so, modelling the folding process and obtaining peak values for stresses and strains over a range of configurations is a highly complex and non-trivial problem.

The basic X-trihex dome structure of Fig. 2.15 was developed somewhat further by introducing sufficient additional bracing to stabilise the structure. As proof of concept, a model was built using straws for struts and stretch cord for cables (Figure 2.17). The cords were secured to the ends of the straws by passing through beads which were held at the ends of the straws by cords which passed through the centre of the straws. In this way the cords could be pre-tensioned in order to increase the rigidity of the X-modules which were assembled into the dome structure by attaching pairs of beads at each node to form flexible joints. The folding mechanism could be successfully modelled provided a small number of struts and cables were first disconnected around the outside of the dome to render the structure unstable. The use of flexible joints enabled the basic stability characteristics of the dome as a reticulated assembly to be ascertained.



Figure 2.17: Deployable, geodesic tensegrity dome model, mounted in a hexagonal box.

Simple, three dimensional tensegrity modules were used to stabilise the six quadrilateral regions along the outside edge of the dome. The short purple struts which appear to float at the

centre of these quadrilaterals are attached at each end to the four surrounding nodes by in-extensional filaments which are under tension. The advantage of such a simple method of bracing is that the joints are simplified and the strut sets form continuous chains without branching. As a structure with rigid joints, the dome structure of Fig. 2.17 is suitable for developing further as a lightweight, efficient structure. However, the dome model with flexible joints was found to be prone to snap through buckling instability. For this reason additional sets of cables were added as guy lines to brace the structure against the wooden hexagonal framework and the centres of the X-modules in the top layer are connected by cords across the centre of the dome. Even with this additional bracing in place the dome is still found to respond poorly under load although the shape and self weight of the structure are easily maintained.

It has been demonstrated using the basic dome model (Figure 2.17) how prestressing can increase the rigidity and therefore, improve the stability characteristics of the structure. In this basic model there are two basic types of prestress that can be applied. The local prestress corresponds to the pretensioning applied to the cables of each tensegrity module individually; whereas, the global prestress is applied to the structure as a whole via tensioning guy lines which prevent the structure from collapsing inwards. Clearly, the global prestress is more important for the overall rigidity of the structure and care should be taken in the design of a tensegrity structure to ensure that the forces induced by prestressing are fairly evenly distributed. If the structure is statically indeterminate and has a number of redundant elements, the internal cables of the structure could be used instead of external guy lines to apply the global prestress. Ideally, a tensegrity dome should be designed so that the prestressing results in a substantial increase in the stiffness of the structure without inducing excessively large forces in the members.

2.2 References

Butcher, S. (2011) *Biosphere structure, close up* {Online image}. Retrieved June 2015 from <https://simon.butcher.name/archives/2011/10/28/Montreal>

Gaba, E. (2009) *Fuller projection* {Online image}. Retrieved June 2015 from https://commons.wikimedia.org/wiki/File:Fuller_projection.svg

Makowski, Z.S. (1984) A history of the development of domes and a review of recent achievements world-wide. *Analysis, design and construction of braced domes* [ed. Makowski, Z.S.], Granada Publishing. pp 1-74

Richter, D.L. (1984) Developments in Temcor aluminium domes. *Analysis, design and construction of braced domes* [ed. Makowski, Z.S.], Granada Publishing. pp 521-538

Chapter 3 Structural Analysis of Tensegrity Domes by the Force Method

3.1 Structural computations with the singular value decomposition of the equilibrium matrix.

The equilibrium matrix of a structural assembly contains a wealth of static/kinematic information on that assembly and is required for standard structural computations by the Force Method. Although not as well established as the Displacement Method which employs the stiffness matrix of an assembly for structural computations, the Force Method has been developed further in recent decades, particularly for the analysis of tensegrity structures and deployable structures. An implementation of the Force Method based on the Singular Value Decomposition (SVD) of the equilibrium matrix has been proposed by Pellegrino (Pellegrino, 1993) and enables a wider range of analysis objectives and types of assemblies to be addressed within a unified computational framework.

A particular advantage of this method is that it makes it possible to answer any question of a static, kinematic or static/kinematic nature. For example, the rank of the equilibrium matrix is computed using the SVD and is required in order to correctly determine the static and kinematic properties of an assembly (Pellegrino and Calladine, 1986). The method is also particularly suitable for the analysis of tensegrity structures, where further information may be obtained from the SVD related to prestress patterns and the nature of inextensional mechanisms. For example, the nullspace of the equilibrium matrix represents the full set of independent states of self-stress of an assembly and is needed in the design of optimal states of prestress, to pretension all cables in a tensegrity framework (Motro, 1989; Pellegrino, 1993); while the left-nullspace of the equilibrium matrix represents the set of independent zero-energy modes, or inextensional mechanisms of an assembly, which are required for the kinematic simulation of motion of a mechanism (Kamman and Huston, 1984; Pellegrino, 1993). Some of these more specialized applications of the equilibrium matrix in the analysis of tensegrity structures will be discussed in more detail in Chapter 5.

Using the Singular Value Decomposition (SVD) of the equilibrium matrix, it is possible to develop an integrated computational framework which addresses the analysis objectives related to the design of tensegrity structures (Pellegrino, 1993). In the following formulation, the method

is applied to the analysis of reticulated assemblies although the method is easily generalised to the analysis of more general types of discrete structure (see (Pellegrino, 1993)).

Reticulated systems are pin jointed systems composed of linear members with bilateral or unilateral rigidity (bars, struts and cables). The loads are assumed to be applied at the nodal points where members meet without any moments or torques being transmitted through the joints. For a reticulated system with b elements, n nodes and k displacement constraints, the number of degrees of freedom for the whole system is $N = 3n - k$ (for a three-dimensional system). The nodal displacements and internal strains are assumed to be sufficiently small so that linear approximation theory may be applied. The governing equations are set up with reference to the original geometric configuration, in which the structure is subject to zero external loads or internal stresses.

The equilibrium equations, which express equilibrium between internal forces and applied loads for each degree of freedom of the system are represented in matrix form as:

$$[A]\{q\} = \{f\} \quad (3.1.1)$$

Here, $[A]$ is the $N \times b$ equilibrium matrix of the structure in its original geometric configuration, $\{q\}$ is the b -vector of tension coefficients and $\{f\}$ is the N -vector of external loads applied on nodes.

For member j :

$$q_j = \frac{T_j}{l_j^0} \quad (3.1.3)$$

where T_j is the axial force in member j , l_j^0 is the length of member j in its original, unstressed state.

The principle that any internal deformation is compatible with external displacements is expressed in the compatibility equations:

$$[A]^t\{d\} = \{e\} \quad (3.1.2)$$

where $[A]^t$ is the transpose of the equilibrium matrix $[A]$, $\{d\}$ is the N -vector of node displacements and $\{e\}$ is the b -vector of member elongation coefficients evaluated with respect to the original configuration.

For member j :

$$e_j = l_j^0 \Delta l_j = l_j^0 (l_j - l_j^0) \quad (3.1.4)$$

where l_j is the length of member j in a loaded state.

For linear-elastic material behaviour, the flexibility relations may be written in matrix form as,

$$\{e\} = \{e^0\} + [F]\{q\} \quad (3.1.5)$$

where $[F]$ is the $b \times b$ flexibility matrix, and $\{e^0\}$ is the vector of elongation coefficients associated with initial, unrestrained deformations that may be present when the internal stresses are equal to zero.

3.1.1 SVD of the Equilibrium matrix

For any matrix $[A]$ of dimension $N \times b$ and rank r , there exists:

- an $N \times N$ orthogonal matrix $[U] = [\{u_1\}, \dots, \{u_N\}]$
- a $b \times b$ orthogonal matrix $[W] = [\{w_1\}, \dots, \{w_b\}]$
- an $N \times b$ matrix $[V]$ with r positive elements v_{ii} ($i = 1, \dots, r$) on the leading diagonal, all other elements zero;

such that

$$[A] = [U][V][W]^t \quad (3.1.6)$$

The coefficients v_{ii} are the singular values of $[A]$ and the vectors $\{u_i\}$ and $\{w_i\}$ are, respectively, the i^{th} left singular vector and i^{th} right singular vector.

The columns of $[U]$ and $[W]$ give orthonormal bases for all four fundamental subspaces of $[A]$:

- The first r columns of $[U]$, denoted $[U^C] = [\{u_1\}, \dots, \{u_r\}]$, correspond to the column space of $[A]$.
- The last $N - r$ columns of $[U]$, denoted $[U^L] = [\{u_{r+1}\}, \dots, \{u_N\}]$, correspond to the left-nullspace of $[A]$.
- The first r columns of $[W]$, denoted $[W^R] = [\{w_1\}, \dots, \{w_r\}]$, correspond to the row space of $[A]$.
- The last $b - r$ columns of $[W]$, denoted $[W^N] = [\{w_{r+1}\}, \dots, \{w_b\}]$, correspond to the nullspace of $[A]$.

(3.1.7)

Assuming $r < \min(N, b)$ it can be shown from the definition of the SVD that the following relations are satisfied

$$[A]\{w_i\} = \begin{cases} v_{ii}\{u_i\} & i = 1, \dots, r \\ \{0\} & i = r + 1, \dots, b \end{cases} \quad (3.1.8)$$

$$[A]^t\{u_i\} = \begin{cases} v_{ii}\{w_i\} & i = 1, \dots, r \\ \{0\} & i = r + 1, \dots, N \end{cases} \quad (3.1.9)$$

3.1.2 *Physical interpretation*

For a general reticulated system let $m (\geq 0)$ denote the degree of kinematic indeterminacy i.e. the number of independent inextensional mechanisms. Similarly, the degree of static indeterminacy represents the number of independent states of self-stress, denoted by $s (\geq 0)$. The parameters m and s can be calculated, after determining the rank r of the equilibrium matrix, from the equations (Pellegrino and Calladine, 1986)

$$m = N - r = 3n - k - r \quad (3.1.10)$$

$$s = b - r \quad (3.1.11)$$

The column space of $[A]$ (abbreviated as $\text{Im } A$), gives the range of the load vector $\{f\}$ which can be supported in static equilibrium by the assembly in its reference configuration. From the compatibility equations (3.1.2) it follows that $\text{Im } A$ is also the vector subspace containing the range of displacement vectors $\{d^I\}$ which require the elongation of one or more bars (and don't have components in the direction of mechanisms). Such vectors, $\{d^I\}$ are defined as follows, $\{d^I\} \in \text{Im } A$.

Similarly, the row space of $[A]$ represents the possible states of stress in the assembly which are in equilibrium with the 'fitted' loads (restricted to $\text{Im } A$). The row space also provides a basis for bar elongations which are geometrically compatible.

In the special case when a structure is both statically and kinematically indeterminate i.e. $m > 0$ and $s > 0$, it follows that $\text{Ker } A$ and $\text{Ker } A^T$ (the nullspace and left-nullspace of $[A]$, respectively) are both non-empty subsets. These vector subspaces also have both kinematic and static interpretations.

From the equation,

$$[A]\{q^0\} = \{0\} \quad (3.1.12)$$

It follows that a self-stress state basis $\{q^0\}$ is a basis of the nullspace of $[A]$ i.e.

$$\{q^0\} \in \text{Ker } A \quad (3.1.13)$$

Similarly, for $m > 0$, particular values of $\{d\}$ for which $\{e\} = 0$ (at first order) can be found. This can be expressed as

$$[A]^T \{d^K\} = \{0\} \quad (3.1.14)$$

Hence, $\{d^K\} \in \text{Ker } A^T$ and the vectors $\{d^K\}$ represent the inextensional mechanisms of the system.

A general displacement $\{d\}$ can then be uniquely expressed as the sum of a displacement $\{d^K\}$ belonging to $\text{Ker } A^T$ and a displacement $\{d^I\}$ belonging to $\text{Im } A$:

$$\{d\} = \{d^K\} + \{d^I\} \quad (3.1.15)$$

3.1.3 *Formulae for structural computations*

Once the SVD of $[A]$ has been obtained, general equations for computing $\{q\}$, $\{e\}$ and $\{d\}$ due to given loads $\{f\}$ and initial strains $\{e^0\}$ are derived as follows (Pellegrino, 1993).

For kinematically indeterminate assemblies it is necessary to check that $\{f\}$ can be carried by the assembly i.e. that $\{f\}$ does not have components in the direction of mechanisms:

$$[U^L]^t \{f\} = \{0\} \quad (3.1.16)$$

If this condition is satisfied, the general solution of Eq. (3.1.1) is

$$\{q\} = \sum_{i=1}^r \frac{\{u_i\}^t \{f\}}{v_{ii}} \{w_i\} + [W^N] \{x\} \quad (3.1.17)$$

where the vector $\{x\}$ contains s free parameters.

The first term on the right-hand side of Eq. (3.1.17) is a stress system in equilibrium with $\{f\}$, written as a summation of stresses due to the components of $\{f\}$ in the directions of the first r left singular vectors of $[A]$ i.e. the columns of $[U^L]$. These individual stresses may be derived from Eq. (3.1.8) and by noting that the component of $\{f\}$ in the direction of $\{u_i\}$ is given by $\{u_i\}^t \{f\}$. The corresponding stress is obtained from the equilibrium equations (Eq. (3.1.8)) by multiplying the i^{th} equation in Eq. (3.1.8) by $\{u_i\}^t \{f\} / v_{ii}$.

The second term on the right-hand side of Eq. (3.1.17) is the general state of self-stress.

The value of $\{x\}$ is determined by a set of s compatibility equations: the strains $\{e\}$ must have zero components in the nullspace of $[A]$; which is also the subspace of incompatible strains;

$$[W^N]^t\{e\} = \{0\} \quad (3.1.18)$$

In terms of the matrices of the SVD, the system of compatibility equations in the standard Force Method of analysis is given by

$$[W^N]^t[F][W^N]\{x\} = -[W^N]^t \left([F] \sum_{i=1}^r \frac{\{u_i\}^t\{f\}}{v_{ii}} \{w_i\} + \{e^0\} \right) \quad (3.1.19)$$

(This equation may be derived by substituting Eq. (3.1.17) for $\{q\}$ into Eq. (3.1.5), then into Eq. (3.1.18))

After solving Eq. (3.1.19) for $\{x\}$, the final set of stresses is obtained from Eq. (3.1.17).

Then the strains are computed from Eq. (3.1.5) and finally the general solution of Eq. (3.1.2) is:

$$\{d\} = \sum_{i=1}^r \frac{\{w_i\}^t\{e\}}{v_{ii}} \{u_i\} + [U^L]\{y\} \quad (3.1.20)$$

Where the m components of $\{y\}$ are free to take any value. A unique solution to Eq. (3.1.20) may be determined using non-linear analysis or asymptotic methods as described in 5.2. In the case the structure is kinematically determinate, $[U^L]$ does not exist, hence if $m = 0$, the unique solution to Eq. (3.1.20) is given by,

$$\{d\} = \sum_{i=1}^r \frac{\{w_i\}^t\{e\}}{v_{ii}} \{u_i\} \quad (3.1.21)$$

3.2 Assembly of equilibrium matrices in cylindrical polar coordinates for reticulated assemblies.

For the purpose of structural analysis, a cylindrical polar coordinate system will be used, both to represent dome geometry and generate a basis for load/displacement vectors. The main advantage of this approach is that the coordinate system will have the same rotational symmetry as the structure. Consequently, the process of assembling the equilibrium matrix of the structure will be much simplified and analysis techniques which exploit the symmetry substructures will be much easier to implement. In addition, the nodal coordinates may be obtained directly from the transformation equations (Eq. (2.2.2) to (2.2.5)) from chart lattice coordinates to dome nodal coordinates introduced in Chapter 2. In Chapter 4, modern methods used to analyse symmetric structures subject to general loading conditions will be explored in

more detail. Here too, the initial choice of coordinate system is important in order to generate the symmetry-adapted variables of the problem and implement sub-structuring techniques as easily and efficiently as possible.

A method is presented for assembling the equilibrium matrix of a pin-jointed structure from element matrices, when a polar coordinate system is used to represent load vectors. For a rotationally periodic structure it is shown that such a choice of coordinates generates an equilibrium matrix which reflects the periodicity of the structure and is in a hyper-cyclic form. In setting up the equilibrium equations in cylindrical polar coordinates it is convenient to use a tension coefficient for each member as defined in Eq. (3.1.3). Then the corresponding measure of elongation of the member is an elongation coefficient as defined in Eq. (3.1.4).

Consider a reticulate assembly, which consists of a total of b elements, n nodes and k displacement constraints. An arbitrary node i is assigned a position vector, $\{P\}_i = \{\rho_i, \theta_i, z_i\}$ and an orthonormal set of basis vectors $\{\Omega_\rho\}_i$, $\{\Omega_\theta\}_i$ and $\{\Omega_z\}_i$ are associated with the node i . These basis vectors form a right handed system and are defined by the cylindrical polar coordinate system so that $\{\Omega_\rho\}_i$, $\{\Omega_\theta\}_i$ and $\{\Omega_z\}_i$ are unit vectors pointing in the direction of increasing ρ_i , θ_i , and z_i , respectively, at the given point i . It follows that the position vector, $\{P\}_i$ may be written as a linear combination of the basis vectors $\{\Omega_\rho\}_i$ and $\{\Omega_z\}_i$.

Load and displacement vectors are represented at node i by the local Cartesian coordinate system which has the same basis vectors $\{\Omega_\rho\}_i$, $\{\Omega_\theta\}_i$ and $\{\Omega_z\}_i$. For a structure which is cylindrically symmetric, the z -axis is chosen to coincide with the axis of symmetry and this ensures that the load and displacement vectors have the same rotational symmetry as the structure. The three equilibrium equations for an arbitrary, unconstrained node i are written as summations of the components of forces in the directions of the three basis vectors $\{\Omega_\rho\}_i$, $\{\Omega_\theta\}_i$ and $\{\Omega_z\}_i$, respectively. For example, if an element l connecting node i and j is under a tension T_l and the coordinates of node j in terms of the basis vectors $\{\Omega_\rho\}_i$, $\{\Omega_\theta\}_i$ and $\{\Omega_z\}_i$, with origin at node i are x_{ij} , y_{ij} , and z_{ij} , respectively, then the contribution of element l to the equilibrium equations at node i are simply,

$$\begin{aligned}\frac{x_{ij}}{L} T_l &= x_{ij} \omega_{ij}, \\ \frac{y_{ij}}{L} T_l &= y_{ij} \omega_{ij}, \\ \frac{z_{ij}}{L} T_l &= z_{ij} \omega_{ij},\end{aligned}\tag{3.2.1}$$

where $\omega_{ij} = \omega_{ji} = q_l$ is the tension coefficient and L is the length of element l .

The equilibrium equations at node i are written as a summation of all contributions from elements meeting at node i and external forces acting on node i . Hence, the three equations of equilibrium of forces at node i may be expressed in the following form;

$$\begin{aligned}\sum_j -x_{ij}\omega_{ij} &= f_{ix} \\ \sum_j -y_{ij}\omega_{ij} &= f_{iy} \\ \sum_j -z_{ij}\omega_{ij} &= f_{iz}\end{aligned}\tag{3.2.2}$$

where the summation is over nodes $j (\neq i)$ belonging to the elements which meet at node i and f_{ix} , f_{iy} and f_{iz} are the components of external force.

By considering equilibrium of forces at each unconstrained node a system of $(3n - k)$ equilibrium equations in b unknowns can be written and assembled in matrix form (Eq. (3.1.1)). Alternatively, the equilibrium matrix, $[A]$ may be assembled in columns from the element equilibrium vectors. The b unknowns in the equilibrium equations are the tension coefficients, hence each column of the matrix $[A]$ corresponds to a particular element. For an element l connecting nodes i to j , the corresponding column of $[A]$ has non-zero entries in rows $3i$ to $(3i + 2)$ and $3j$ to $(3j + 2)$. The non-zero values of the l^{th} column of $[A]$ are stored in the 6×1 element equilibrium vector, $\{A\}_l$ for element l . The process of assembling the global matrix $[A]$ from element vectors based on the element connectivities is more practical for use in a computer program.

The element equilibrium vector may be derived from the global nodal coordinates of the element as follows. A typical element, l connecting nodes i and j has global nodal coordinates $\{P\}_i = \{\rho_i, \theta_i, z_i\}$ and $\{P\}_j = \{\rho_j, \theta_j, z_j\}$ for nodes i and j , respectively. The element equilibrium vector is of the following form;

$$\{A\}_l = \begin{Bmatrix} -x_{ij} \\ -y_{ij} \\ -z_{ij} \\ -x_{ji} \\ -y_{ji} \\ -z_{ji} \end{Bmatrix}\tag{3.2.3}$$

The components of $\{A\}_l$ may be expressed in terms of the global nodal coordinates through the following analysis of the geometry. Figure 3.1 shows a typical element in plan view. The origin O

of the global coordinate system and polar angles θ_i and θ_j of the element nodes are indicated on the diagram. The x_i and y_i coordinate axes for the local Cartesian coordinate system at node i are aligned with the basis vectors $\{\Omega_\rho\}_i$ and $\{\Omega_\theta\}_i$ as shown.

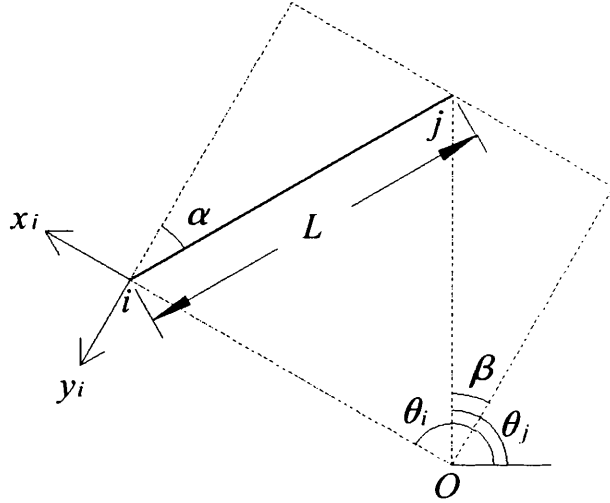


Figure 3.1:

A typical element in plan view with local and global coordinates indicated.

From figure 3.1, the following equalities are satisfied for the coordinates, x_{ij} and y_{ij} of node j in the local coordinate system at node i .

$$x_{ij} = -L \sin \alpha = \rho_j \sin \beta - \rho_i \quad (3.2.4)$$

$$y_{ij} = -L \cos \alpha = -\rho_j \cos \beta \quad (3.2.5)$$

Noting that,

$$\beta = \theta_j - \left(\theta_i - \frac{\pi}{2} \right) \quad (3.2.6)$$

the following equalities are satisfied;

$$\sin \beta = \sin \left(\theta_j - \theta_i + \frac{\pi}{2} \right) = \cos(\theta_j - \theta_i) \quad (3.2.7)$$

$$\cos \beta = \cos \left(\theta_j - \theta_i + \frac{\pi}{2} \right) = -\sin(\theta_j - \theta_i) \quad (3.2.8)$$

Let $\theta_{ij} = \theta_j - \theta_i$, then substituting Eq. (3.2.7) in (3.2.4) and Eq. (3.2.8) in (3.2.5) the following equations for the local coordinates in terms of global coordinates are obtained.

$$x_{ij} = \rho_j \cos \theta_{ij} - \rho_i \quad (3.2.9)$$

$$y_{ij} = \rho_j \sin \theta_{ij} \quad (3.2.10)$$

Similarly, the coordinates of node i with respect to node j satisfy the following equalities;

$$\begin{aligned}
 x_{ji} &= \rho_i \sin(\pi - \beta) - \rho_j \\
 &= \rho_i \cos \theta_{ij} - \rho_j
 \end{aligned}
 \tag{3.2.11}$$

$$\begin{aligned}
 y_{ji} &= -\rho_i \cos(\pi - \beta) \\
 &= -\rho_i \sin \theta_{ij}
 \end{aligned}
 \tag{3.2.12}$$

Finally, the components of the element equilibrium vector in global coordinates are given as follows;

$$\{A\}_l = \begin{Bmatrix} \rho_i - \rho_j \cos \theta_{ij} \\ -\rho_j \sin \theta_{ij} \\ z_i - z_j \\ \rho_j - \rho_i \cos \theta_{ij} \\ \rho_i \sin \theta_{ij} \\ z_j - z_i \end{Bmatrix}
 \tag{3.2.13}$$

The assembly of the equilibrium matrix is illustrated for the simple 2-dimensional reticulate assembly shown in Figure 3.2. In this case each unconstrained node has 2 degrees of freedom and the global equilibrium matrix is a square, 12×12 matrix.

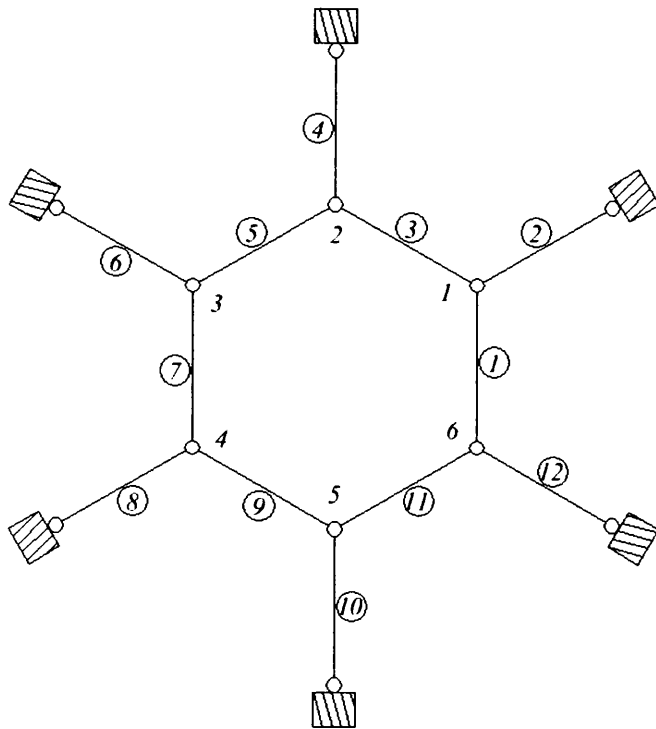


Figure 3.2:
A two-dimensional hexagonal cable structure with element numbers and unconstrained node numbers indicated.

The element equilibrium vectors for elements 1,3,5,7,9 and 11 are given by,

$$\{A\}_1 = \{A\}_3 = \{A\}_5 = \{A\}_7 = \{A\}_9 = \{A\}_{11} = \left\{ -\frac{1}{2}, \frac{\sqrt{3}}{2}, -\frac{1}{2}, -\frac{\sqrt{3}}{2} \right\}^t \quad (3.2.14)$$

and equilibrium vectors for elements attached to foundation nodes are given by,

$$\{A\}_2 = \{A\}_4 = \{A\}_6 = \{A\}_8 = \{A\}_{10} = \{A\}_{12} = \{1,0\}^t \quad (3.2.15)$$

The global equilibrium matrix is assembled from the element vectors according to the element connectivities. Thus, the equilibrium matrix, $[A]$ is the following hyper-cyclic matrix:

$$[A] = \begin{bmatrix} L & K & \dots & 0 \\ & L & K & \\ \vdots & & L & \ddots & \vdots \\ 0 & & & \ddots & \\ \vdots & & & & K \\ K & \dots & 0 & \dots & L \end{bmatrix} \quad (3.2.16)$$

in which

$$[K] = \begin{bmatrix} -1/2 & 0 \\ \sqrt{3}/2 & 0 \end{bmatrix}, \quad [L] = \begin{bmatrix} -1/2 & 1 \\ -\sqrt{3}/2 & 0 \end{bmatrix} \quad (3.2.17)$$

3.3 Matrix methods for computational analysis of tensegrity dome frameworks

To improve the structural characteristics of the basic X-trihex lattice dome composed of X-modules (Fig. 2.15 and 2.17), it is proposed to replace the flexible joint connections between X-modules with rigid joints. Furthermore, beams are to be joined together at their crossing points at the centre of each X-module by a "scissor hinge," or pin joint. Using three-dimensional frame analysis techniques based on the Force Method it is proposed to develop a finite element model to simulate the dome structure under various loading conditions. For simplicity, the equilibrium matrix for the X-truss is first derived for a 2-dimensional problem in polar coordinates. The matrix methods for analysis of the corresponding 3-dimensional problem are then developed to facilitate the computational analysis of a dome structure.

3.3.1 X-module element matrices in 2-dimensions

The global coordinate system used to represent forces applied at the four external nodes of the X-module is illustrated in Fig.3.3. At global node i , the generalised force vector, $\mathcal{F}_i = \{f_{ix}, f_{iy}, c_{iz}\}^t$ is represented in a right handed orthogonal coordinate system in which the x_i, y_i

and z_i coordinate axes are tangent to the ρ, θ and z coordinate curves, respectively, used to represent dome nodal coordinates with respect to origin O . The coordinate system used to represent the force vectors in the figure is also referred to as a polar coordinate system and the same coordinate system is used to represent nodal displacements.

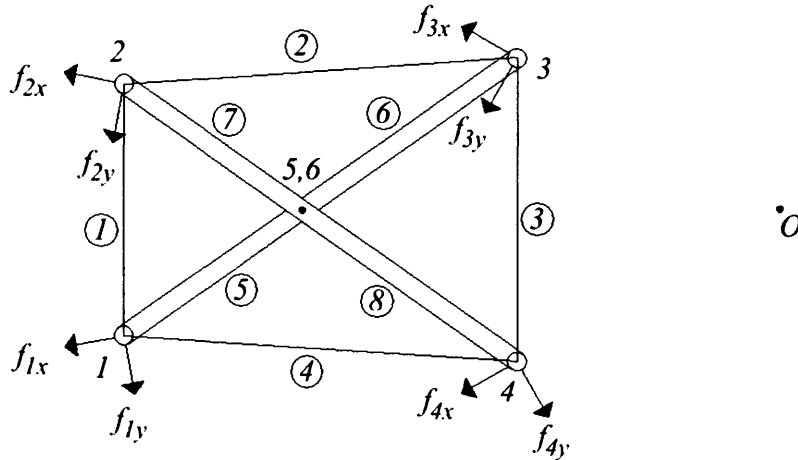


Figure 3.3: X-module composed of two beams joined by a scissor hinge and braced with cables. Each beam is modelled as two separate, fully connected beam elements. The nodes are numbered 1 to 6 and the elements are numbered 1 to 8 and circled. The polar coordinate system with origin at O is used to represent nodal force vectors.

Next, we consider the process of assembling macro-element matrices for the two-dimensional X-module from beam and cable element matrices. The equilibrium, compatibility and flexibility equations for the 2-D beam element ' l ' shown in Fig. 3.4(a), with respect to the local coordinate system $1, x, y$ defined in the figure are given by Eq. (3.3.1), (3.3.2) and (3.3.3) respectively.

$$\begin{bmatrix} 0 & -1 & 1 \\ L & 0 & 0 \\ 0 & -L & 0 \\ 0 & 1 & -1 \\ -L & 0 & 0 \\ 0 & 0 & L \end{bmatrix} \begin{Bmatrix} q_l \\ u_{1(l)} \\ u_{2(l)} \end{Bmatrix} = \begin{Bmatrix} f_{1x} \\ f_{1y} \\ c_{1z} \\ f_{2x} \\ f_{2y} \\ c_{2z} \end{Bmatrix} \quad (3.3.1)$$

$$\begin{bmatrix} 0 & L & 0 & 0 & -L & 0 \\ -1 & 0 & -L & 1 & 0 & 0 \\ 1 & 0 & 0 & -1 & 0 & L \end{bmatrix} \begin{Bmatrix} d_{1x} \\ d_{1y} \\ \eta_{1z} \\ d_{2x} \\ d_{2y} \\ \eta_{2z} \end{Bmatrix} = \begin{Bmatrix} e_l \\ \phi_{1(l)} \\ \phi_{2(l)} \end{Bmatrix} \quad (3.3.2)$$

$$\begin{bmatrix} L^3/AE & 0 & 0 \\ 0 & L^3/3EI_z & L^3/6EI_z \\ 0 & L^3/6EI_z & L^3/3EI_z \end{bmatrix} \begin{Bmatrix} q_l \\ u_{1(l)} \\ u_{2(l)} \end{Bmatrix} = \begin{Bmatrix} e_l \\ \phi_{1(l)} \\ \phi_{2(l)} \end{Bmatrix} \quad (3.3.3)$$

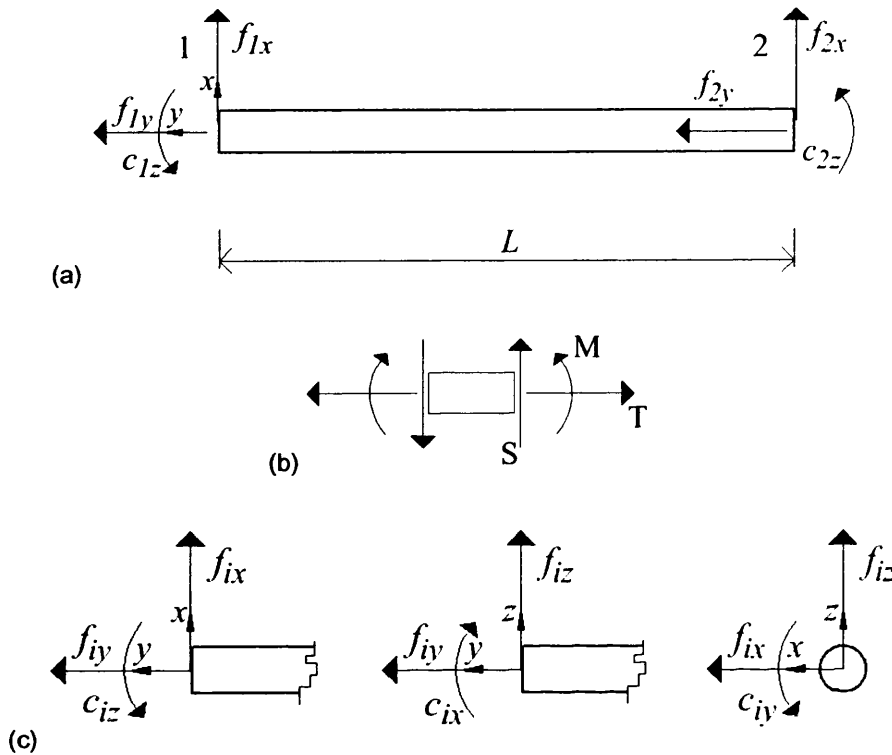


Figure 3.4: (a) Two-dimensional beam element with local coordinate system 1, x , y . (b) Sign convention for the positive stress resultants. The shear stress S does not appear explicitly in the formulation. (c) Local coordinate system for three-dimensional beam element with six degrees of freedom per node.

In equations (3.3.1) to (3.3.3) the generalised stress variables are the tension coefficient, q_l and the moment coefficients $u_{1(l)}$ and $u_{2(l)}$, representing the bending moments at the two ends of the beam. In terms of the actual bending moment, $M_{i(l)}$ at node i of a beam, the moment coefficient is expressed as $u_{i(l)} = M_{i(l)}/L$. The generalised strains corresponding to this choice of stresses include the elongation coefficient, e_l and the coefficients $\phi_{1(l)}$ and $\phi_{2(l)}$ which correspond to the actual rotations of end 1 and end 2 with respect to the beam axis, scaled by a factor of L . Note that the generalised external variables are represented by actual forces and displacements, for example, η_{1z} and η_{2z} are the actual rotations of joints 1 and 2 corresponding to the couples c_{1z} and c_{2z} . The sign convention used for external and internal variables are illustrated in Fig.3.4 (a) and (b), respectively.

Equations (3.3.1) and (3.3.2) are transformed to the global coordinate system of the X-module by pre-multiplying Eq. (3.3.1) by the following rotation matrix;

$$[R_l^z] = \begin{bmatrix} \Lambda_{ij} & 0 \\ 0 & \Lambda_{ji} \end{bmatrix} \quad (3.3.4)$$

where,

$$\Lambda_{ij} = \begin{bmatrix} \cos \alpha_{ij} & \sin \alpha_{ij} & 0 \\ -\sin \alpha_{ij} & \cos \alpha_{ij} & 0 \\ 0 & 0 & 1 \end{bmatrix} \quad (3.3.5)$$

$$\Lambda_{ji} = \begin{bmatrix} -\cos \alpha_{ji} & -\sin \alpha_{ji} & 0 \\ \sin \alpha_{ji} & -\cos \alpha_{ji} & 0 \\ 0 & 0 & 1 \end{bmatrix} \quad (3.3.6)$$

The angle α_{ij} corresponds to α in Fig. 3.1 and is the angle of orientation of element l with respect to the coordinate axis at node i . The angle α_{ji} is measured similarly with the roles of node i and j of the element reversed. From equations (3.2.4) to (3.2.8) the following identities are obtained:

$$\cos \alpha_{ij} = \frac{-\rho_j \sin \theta_{ij}}{L} \quad (3.3.7)$$

$$\sin \alpha_{ij} = \frac{\rho_i - \rho_j \cos \theta_{ij}}{L} \quad (3.3.8)$$

$$\cos \alpha_{ji} = \frac{\rho_i \sin \theta_{ij}}{L} \quad (3.3.9)$$

$$\sin \alpha_{ji} = \frac{\rho_j - \rho_i \cos \theta_{ij}}{L} \quad (3.3.10)$$

Substituting Eq. (3.3.7) and (3.3.8) into (3.3.5) and Eq. (3.3.9) and (3.3.10) into (3.3.6) the rotation matrices may be expressed in terms of the nodal coordinates as follows;

$$\Lambda_{ij(l)} = \frac{1}{L} \begin{bmatrix} -\rho_j \sin \theta_{ij} & \rho_i - \rho_j \cos \theta_{ij} & 0 \\ \rho_j \cos \theta_{ij} - \rho_i & -\rho_j \sin \theta_{ij} & 0 \\ 0 & 0 & L \end{bmatrix} \quad (3.3.11)$$

$$\Lambda_{ji(l)} = \frac{1}{L} \begin{bmatrix} -\rho_i \sin \theta_{ij} & \rho_i \cos \theta_{ij} - \rho_j & 0 \\ \rho_j - \rho_i \cos \theta_{ij} & -\rho_i \sin \theta_{ij} & 0 \\ 0 & 0 & L \end{bmatrix} \quad (3.3.12)$$

It is convenient to introduce the following short-hand notation for the equilibrium matrix, in the global coordinate system

$$\begin{bmatrix} A_{1(l)} \\ A_{2(l)} \end{bmatrix} \{\sigma_l\} = \begin{Bmatrix} \mathcal{F}_1 \\ \mathcal{F}_2 \end{Bmatrix} \quad (3.3.13)$$

Where the two sub matrices, of size 3×3 , correspond to the “start” and “end” nodes of the member, respectively. The external force components have been grouped together by node and stress variables are represented by the vector $\{\sigma_l\}$.

The full system of equilibrium equations for the X-module (Fig.3.3) in a general configuration defined by the nodal coordinates is represented by the following matrix equation. For analysis of the X-module as a 2-dimensional assembly there are a total of 18 generalised stress variables which can be grouped into 4 sets of 1, each corresponding to a cable element, 4 sets of 3, each corresponding to a beam element, and a final set of 2 corresponding to the scissor hinge. The two equilibrium sub-matrices of a particular element are assembled in the global equilibrium matrix such that the row position matches the particular joint of the X-module to which each sub-matrix refers, and the column position matches the element number.

$$\left[\begin{array}{ccccccccc} A_{1(1)} & & & & & & & & \\ & A_{2(2)} & & & & & & & \\ & & A_{3(3)} & & & & & & \\ & & & A_{4(4)} & & & & & \\ & & & & A_{5(5)} & & & & \\ & & & & & A_{6(6)} & & & \\ & & & & & & A_{7(7)} & & \\ & & & & & & & A_{8(8)} & \\ & & & & & & & & A_{9(9)} \end{array} \right] \begin{Bmatrix} q_1 \\ q_2 \\ q_3 \\ q_4 \\ \{\sigma_5\} \\ \{\sigma_6\} \\ \{\sigma_7\} \\ \{\sigma_8\} \\ \{\sigma_9\} \end{Bmatrix} = \begin{Bmatrix} \mathcal{F}_1 \\ \mathcal{F}_2 \\ \mathcal{F}_3 \\ \mathcal{F}_4 \\ \mathcal{F}_5 \\ \mathcal{F}_6 \end{Bmatrix} \quad (3.3.14)$$

The beams 5 and 6 are fully connected at joint 5 and beams 7 and 8 are fully connected at joint 6. Neither forces nor couples can be applied at joints 5 and 6 which are collocated, hence $\mathcal{F}_5 = \mathcal{F}_6 = \{0,0,0\}^t$. As the X-module is rigidly connected to other structural units at its external joints, forces and couples may be applied at these joints.

The equilibrium sub-matrices for cable elements (elements 1 to 4) are column vectors corresponding to the first column of the beam equilibrium matrix (Eq. 3.3.1). Thus, for a general cable element, the element equilibrium matrix in global coordinates is given by,

$$\begin{Bmatrix} A_{i(l)} \\ A_{j(l)} \end{Bmatrix} = [R_l^z] \begin{Bmatrix} 0 \\ L \\ 0 \\ 0 \\ -L \\ 0 \end{Bmatrix} = \begin{Bmatrix} \rho_i - \rho_j \cos \theta_{ij} \\ -\rho_j \sin \theta_{ij} \\ 0 \\ \rho_j - \rho_i \cos \theta_{ij} \\ \rho_i \sin \theta_{ij} \\ 0 \end{Bmatrix} \quad (3.3.15)$$

The unknown components of force exerted through the scissor hinge, by joint 6 onto joint 5 are denoted by R_x and R_y . These are represented as stress variables corresponding to the scissor hinge, i.e.

$$\{\sigma_9\} = \begin{Bmatrix} R_x \\ R_y \end{Bmatrix} \quad (3.3.16)$$

The contributions of the scissor hinge to the global equilibrium matrix are easily obtained as follows;

$$\begin{bmatrix} A_{5(9)} \\ A_{6(9)} \end{bmatrix} = \begin{bmatrix} -1 & 0 \\ 0 & -1 \\ 0 & 0 \\ 1 & 0 \\ 0 & 1 \\ 0 & 0 \end{bmatrix} \quad (3.3.17)$$

3.3.2 X-module element matrices in 3-dimensions

For the analysis of a dome structure the X-modules are represented in a general three-dimensional configuration and the global coordinates correspond to the cylindrical polar coordinates used to represent dome geometry. In addition there will be up to 6 degrees of freedom at each unconstrained joint and the 6 components of internal stress for a beam element will include a torque and an additional bending moment at each node. For a typical beam element the local coordinate system used to represent the external forces and moments applied at node i is illustrated in Fig.3.4(c).

Additional matrix equations are given below to represent the equilibrium, compatibility and flexibility equations for the remaining degrees of freedom and stress/strain components of the three-dimensional beam element. Thus, equations (3.3.1) and (3.3.18) form the complete set of equilibrium equations for the beam element. Similarly, equations (3.3.2) and (3.3.19) are the compatibility equations and (3.3.3) and (3.3.20) are the flexibility equations.

$$\begin{bmatrix} 0 & -L & 0 \\ L & 0 & 0 \\ 0 & 1 & -1 \\ 0 & 0 & L \\ -L & 0 & 0 \\ 0 & -1 & 1 \end{bmatrix} \begin{Bmatrix} t_i \\ v_{1(i)} \\ v_{2(i)} \end{Bmatrix} = \begin{Bmatrix} c_{1x} \\ c_{1y} \\ f_{1z} \\ c_{2x} \\ c_{2y} \\ f_{2z} \end{Bmatrix} \quad (3.3.18)$$

$$\begin{bmatrix} 0 & L & 0 & 0 & -L & 0 \\ -L & 0 & 1 & 0 & 0 & -1 \\ 0 & 0 & -1 & L & 0 & 1 \end{bmatrix} \begin{Bmatrix} \eta_{1x} \\ \eta_{1y} \\ d_{1z} \\ \eta_{2x} \\ \eta_{2y} \\ d_{2z} \end{Bmatrix} = \begin{Bmatrix} \delta_i \\ \theta_{1(i)} \\ \theta_{2(i)} \end{Bmatrix} \quad (3.3.19)$$

$$\begin{bmatrix} L^3/GJ & 0 & 0 \\ 0 & L^3/3EI_x & L^3/6EI_x \\ 0 & L^3/6EI_x & L^3/3EI_x \end{bmatrix} \begin{Bmatrix} t_i \\ v_{1(i)} \\ v_{2(i)} \end{Bmatrix} = \begin{Bmatrix} \delta_i \\ \theta_{1(i)} \\ \theta_{2(i)} \end{Bmatrix} \quad (3.3.20)$$

The stress variables include the torque (per unit length) t_i and the moment coefficients $v_{1(i)}$ and $v_{2(i)}$ representing internal moments at nodes 1 and 2 associated with rotations in the y - z plane (local coordinates). The set of generalised strains include the rotation coefficient δ_i associated

with the angle of twist of the beam and the two coefficients $\theta_{1(l)}$ and $\theta_{2(l)}$ represent the rotation angles in the y - z plane of ends 1 and 2 of the beam, respectively, with respect to the central axis. (The strain coefficient associated with a rotation is obtained by multiplying the rotation angle by the length of the element.) The nodal forces and displacements follow the same notation introduced previously and the sign convention used is illustrated in Fig.3.4(c). For a beam element connecting nodes i and j the internal torque at node i is positive in an anticlockwise sense when viewed from node i towards j . The sign convention for the internal strain variables agrees with the sign convention for corresponding stress variables.

For notational convenience the beam element equilibrium matrices in local coordinates are partitioned as follows. The superscripts I and II identify sub-matrices corresponding to the two sets of equilibrium equations, Eq. (3.3.1) and (3.3.18), respectively.

$$\begin{bmatrix} A_{1(l)}^I \\ A_{2(l)}^I \end{bmatrix} = \begin{bmatrix} 0 & -1 & 1 \\ L & 0 & 0 \\ 0 & -L & 0 \\ 0 & 1 & -1 \\ -L & 0 & 0 \\ 0 & 0 & L \end{bmatrix} \quad (3.3.21)$$

$$\begin{bmatrix} A_{1(l)}^{II} \\ A_{2(l)}^{II} \end{bmatrix} = \begin{bmatrix} 0 & -L & 0 \\ L & 0 & 0 \\ 0 & 1 & -1 \\ 0 & 0 & L \\ -L & 0 & 0 \\ 0 & -1 & 1 \end{bmatrix} \quad (3.3.22)$$

The full set of equilibrium equations for a beam element in 3-dimensions are then represented in the following form;

$$\begin{bmatrix} A_{1(l)}^I & 0 \\ 0 & A_{1(l)}^{II} \\ A_{2(l)}^I & 0 \\ 0 & A_{2(l)}^{II} \end{bmatrix} \begin{Bmatrix} q_l \\ u_{1(l)} \\ u_{2(l)} \\ t_l \\ v_{1(l)} \\ v_{2(l)} \end{Bmatrix} = \begin{Bmatrix} f_{1x} \\ f_{1y} \\ c_{1z} \\ c_{1x} \\ c_{1y} \\ f_{1z} \\ f_{2x} \\ f_{2y} \\ c_{2z} \\ c_{2x} \\ c_{2y} \\ f_{2z} \end{Bmatrix} \quad (3.3.23)$$

The equilibrium equations (3.3.23) are transformed to the global coordinate system in two stages. Firstly, the local coordinates are transformed by applying a rotation about the nodal x -axis at each node of the element. The rotation angle, λ_l is measured as the slope angle of the element l with respect to the horizontal plane in global coordinates. The angle λ_l is positive if

the element slopes upwards from node i to node j , where i and j are the “start” and “end” nodes of the element, respectively.

In order to transform the equilibrium equations, the two equilibrium sub-matrices in Eq. (3.3.23) are individually pre-multiplied by the rotation matrix $[R_l^x]$ which transforms the external variables of the system by rotating the coordinate system at each node, about the (local) x -axis by an angle λ_l . The matrix $[R_l^x]$ is given by;

$$[R_l^x] = \begin{bmatrix} 1 & 0 & 0 & 0 & 0 & 0 \\ 0 & \cos \lambda_l & 0 & 0 & 0 & \sin \lambda_l \\ 0 & 0 & \cos \lambda_l & 0 & -\sin \lambda_l & 0 \\ 0 & 0 & 0 & 1 & 0 & 0 \\ 0 & 0 & \sin \lambda_l & 0 & \cos \lambda_l & 0 \\ 0 & -\sin \lambda_l & 0 & 0 & 0 & \cos \lambda_l \end{bmatrix} \quad (3.3.24)$$

The values of the coefficients of the rotation matrix $[R_l^x]$ may be computed as follows;

$$\cos \lambda_l = \frac{1}{L} \sqrt{L^2 - (z_j - z_i)^2} \quad (3.3.25)$$

$$\sin \lambda_l = \frac{1}{L} (z_j - z_i) \quad (3.3.26)$$

The beam element equilibrium matrices are transformed to the global, cylindrical polar coordinate system by applying a final rotation about the z -axis at each node, which aligns the x and y coordinate axis at each node with the global r and θ coordinate axis, respectively. The rotation matrix which pre-multiplies the first equilibrium sub-matrix in Eq. (3.3.23) corresponding to node 1 of the element is given by;

$$[R_{(1)l}^z] = \begin{bmatrix} \Lambda_{ij} & 0 \\ 0 & \Lambda_{ij} \end{bmatrix} \quad (3.3.27)$$

where

$$[\Lambda_{ij}] = \frac{1}{L \cos \lambda_l} \begin{bmatrix} -\rho_j \sin \theta_{ij} & \rho_i - \rho_j \cos \theta_{ij} & 0 \\ \rho_j \cos \theta_{ij} - \rho_i & -\rho_j \sin \theta_{ij} & 0 \\ 0 & 0 & L \cos \lambda_l \end{bmatrix} \quad (3.3.28)$$

Similarly, the rotation matrix which pre-multiplies the second equilibrium sub-matrix in Eq. (3.3.23) corresponding to node 2 of the element is given by;

$$[R_{(2)l}^z] = \begin{bmatrix} \Lambda_{ji} & 0 \\ 0 & \Lambda_{ji} \end{bmatrix} \quad (3.3.29)$$

where

$$[\Lambda_{ji}] = \frac{1}{L \cos \lambda_l} \begin{bmatrix} -\rho_i \sin \theta_{ij} & \rho_i \cos \theta_{ij} - \rho_j & 0 \\ \rho_j - \rho_i \cos \theta_{ij} & -\rho_i \sin \theta_{ij} & 0 \\ 0 & 0 & L \cos \lambda_l \end{bmatrix} \quad (3.3.30)$$

Finally, the complete set of transformations of the equilibrium matrix for a beam element from local to global coordinates may be represented by the following matrix expressions, which give the global equilibrium sub-matrices as transformations of the local equilibrium sub-matrices.

$$[A_{1(l)}] = [R_{(1)l}^z][R_l^x] \begin{bmatrix} A_{1(l)}^I & 0 \\ 0 & A_{1(l)}^{II} \end{bmatrix} \quad (3.3.31)$$

$$[A_{2(l)}] = [R_{(2)l}^z][R_l^x] \begin{bmatrix} A_{2(l)}^I & 0 \\ 0 & A_{2(l)}^{II} \end{bmatrix} \quad (3.3.32)$$

The two global equilibrium sub-matrices, $[A_{1(l)}]$ and $[A_{2(l)}]$ are now 6×6 matrices, corresponding to the “start” and “end” node of the beam element, respectively.

The equilibrium equations for the three-dimensional beam element in global coordinates may then be represented in the general form given by Eq. (3.3.13), where the two equilibrium sub-matrices are given by Eq. (3.3.31) and (3.3.32), and the internal stress and external force variables in global coordinates are, respectively,

$$\{\sigma_l\} = \begin{Bmatrix} \sigma_l^I \\ \sigma_l^{II} \end{Bmatrix} = \begin{Bmatrix} q_l \\ u_{1(l)} \\ u_{2(l)} \\ t_l \\ v_{1(l)} \\ v_{2(l)} \end{Bmatrix} \quad (3.3.33)$$

$$\{\mathcal{F}_1\} = \begin{Bmatrix} \mathcal{F}_1^I \\ \mathcal{F}_1^{II} \end{Bmatrix} = \begin{Bmatrix} f_{1x} \\ f_{1y} \\ c_{1z} \\ c_{1x} \\ c_{1y} \\ f_{1z} \end{Bmatrix} \quad (3.3.34)$$

$$\{\mathcal{F}_2\} = \begin{Bmatrix} \mathcal{F}_2^I \\ \mathcal{F}_2^{II} \end{Bmatrix} = \begin{Bmatrix} f_{2x} \\ f_{2y} \\ c_{2z} \\ c_{2x} \\ c_{2y} \\ f_{2z} \end{Bmatrix} \quad (3.3.35)$$

Using the above notation the equilibrium equations for the X-module in 3-dimensions can easily be assembled element by element and has the exact same form as Eq. (3.3.14).

The cable element equilibrium vectors may be obtained from the first column of the beam equilibrium matrix. Hence, the two equilibrium sub-matrices for a cable element in a three-dimensional configuration with “start” and “end” nodes i and j , respectively are given by;

$$\begin{Bmatrix} A_{i(l)} \\ A_{j(l)} \end{Bmatrix} = \begin{bmatrix} R_{(1)l}^z & 0 \\ 0 & R_{(2)l}^z \end{bmatrix} \begin{bmatrix} R_l^x & 0 \\ 0 & R_l^x \end{bmatrix} \begin{Bmatrix} 0 \\ L \\ 0 \\ 0 \\ 0 \\ 0 \\ 0 \\ 0 \\ 0 \\ 0 \end{Bmatrix} = \begin{Bmatrix} \rho_i - \rho_j \cos \theta_{ij} \\ -\rho_j \sin \theta_{ij} \\ 0 \\ 0 \\ 0 \\ z_i - z_j \\ \rho_j - \rho_i \cos \theta_{ij} \\ \rho_i \sin \theta_{ij} \\ 0 \\ 0 \\ 0 \\ z_j - z_i \end{Bmatrix} \quad (3.3.36)$$

For a check of consistency Eq. (3.3.36) is seen to be in agreement with the element equilibrium vector given in Eq. (3.2.13) for a reticulate assembly.

In three-dimensions the scissor hinge will transfer a three-dimensional force vector from joint 6 to onto joint 5. This force is represented as a generalised strain in the equilibrium equations, given by,

$$\{\sigma_9\} = \begin{Bmatrix} R_x \\ R_y \\ R_z \end{Bmatrix} \quad (3.3.37)$$

The contribution of the scissor hinge to the equilibrium matrix of the X-module (Eq. 3.3.14) is easily obtained as the following two sub-matrices;

$$[A_{5(9)}] = \begin{bmatrix} -1 & 0 & 0 \\ 0 & -1 & 0 \\ 0 & 0 & 0 \\ 0 & 0 & 0 \\ 0 & 0 & 0 \\ 0 & 0 & -1 \end{bmatrix} \quad (3.3.38)$$

$$[A_{6(9)}] = \begin{bmatrix} 1 & 0 & 0 \\ 0 & 1 & 0 \\ 0 & 0 & 0 \\ 0 & 0 & 0 \\ 0 & 0 & 0 \\ 0 & 0 & 1 \end{bmatrix} \quad (3.3.39)$$

A method for reducing the global equilibrium matrix of a pantograph element, similar to the X-module used in the example above, is presented in (Pellegrino, 2001). The matrix reduction may be applied when several of the external couples and loads within the structure have been set equal to zero, i.e. when rigid joints are replaced by pin joints.

It is possible to assemble the global equilibrium matrix for the entire dome structure from the global equilibrium matrices of each X-module or substructure of the assembly; however, by exploiting the symmetry of the dome structure, considerable time and computational effort can be saved by analysing only the symmetry substructure. The application of group representation theory in order to reduce the equilibrium matrix of a symmetric structure to a block diagonal form

is discussed in Chapter 4. Reducing the equilibrium matrix to a block diagonal form significantly reduces the computational cost required to perform the SVD required for structural analysis. In addition, substructuring techniques can be employed so that the full equilibrium matrix never needs to be generated.

3.4 References

Kamman, J.W. and Huston, R.L. (1984). Dynamics of constrained multibody systems. *J. Appl. Mech.* 51, pp. 899-903.

Motro, R. (1989). Tensegrity systems – latest developments and perspectives. In *Proc. 10 Years of Progress in Shell and Spatial Structures, 30th Anniversary of IASS*, Madrid, Spain [ed. F. del Pozo and A. de las Casas]. IASS.

Pellegrino, S. and Calladine, C.R. (1986) Matrix analysis of statically and kinematically indeterminate frameworks. *Int. J. Solids Structures*, 22(4), pp. 409-428.

Pellegrino, S. (1993). Structural computations with the singular value decomposition of the equilibrium matrix. *Int. J. Solids Structures*, 30(21), pp. 3025-3035.

Pellegrino, S. (2001). Deployable Structures. *CISM Courses and Lectures*, no. 412. Springer-Verlag Wien.

Chapter 4 A Computational Framework for the Analysis of Symmetric Structures

By applying group representation theory to the analysis of symmetric structures it has been shown that for a structure with any type of symmetry, subjected to a general loading, considerable time and computational effort can be saved by separately analysing the symmetry substructures (Kangwai, 1997; Kangwai et al., 1999). Symmetry subspace methods are particularly suitable for the analysis of dome structures, which generally have a high degree of symmetry. The advantage of using symmetry subspace methods based on group representation theory is that the full symmetry properties of a structure may be exploited in order to systematically simplify the structural analysis.

The main type of symmetry that is relevant in the analysis of dome structures is cylindrical symmetry, i.e. symmetry operations, such as reflections or rotations, are defined with respect to the central axis of the dome. For example, a geodesic tensegrity dome, designed for clustering in two dimensions, will, at most, possess the 6-fold rotational symmetry and 6 reflection planes of the hexagon. These 12 symmetry operations constitute a symmetry group C_{6v} . Many of the dome structures considered in this report have this type of symmetry. For analysis of dome honeycomb structures the interactions between domes would need to be taken into account and a detailed analysis would require the structure to be analysed in its entirety. In this case, exploiting the symmetry of the structure to simplify the analysis would reduce the computational cost significantly and for large arrays of domes, methods similar to those used in crystallography would be more appropriate. Similarly, in the analysis of large individual dome structures, with many members, the cost of computation would be reduced significantly by applying symmetry subspace methods. Even for the analysis of basic dome structures the symmetry subspace methods can be adapted to enable structures to be analysed efficiently by hand with minimum computing requirements.

In the following presentation of symmetry subspace methods, emphasis is put on the choice of an appropriate initial coordinate system to represent load and displacement vectors in order to simplify the transformations to symmetry-adapted coordinates and derive more efficient algorithms for implementing the symmetry subspace method in coding. It is shown that the reducible representations of the symmetry group of a symmetric structure can be simplified significantly due to the particular choice of coordinate system.

Secondly, due to the symmetry of the structure, the matrix representations of symmetry groups in cylindrical polar coordinates are of a simplified form and data type. This simplified form of data can be exploited in computer implementation in order to automatically obtain the symmetry subspaces for the load and displacement vectors. The symmetry-adapted vector bases, represented in the cylindrical polar coordinate system, are used to transform the equilibrium matrix into a block diagonal form, which significantly reduces the complexity of the problem and amount of computation required for large symmetric structures.

The theoretical basis for symmetry subspace methods is given, following the formulation presented by Kangwai (1997) and Kangwai et al. (1999). An alternative method for generating the symmetry-adapted vector basis, which relies on the choice of initial coordinate system, is presented and the algorithms for implementing this in code are discussed. Finally, the advantage of using sub-structuring techniques to develop more efficient implementations of the symmetry subspace methods are briefly discussed, with reference to previous work by e.g. Kangwai (1997) and Bossavit (1986).

4.1 Symmetry group representations for structures with C_{6v} symmetry

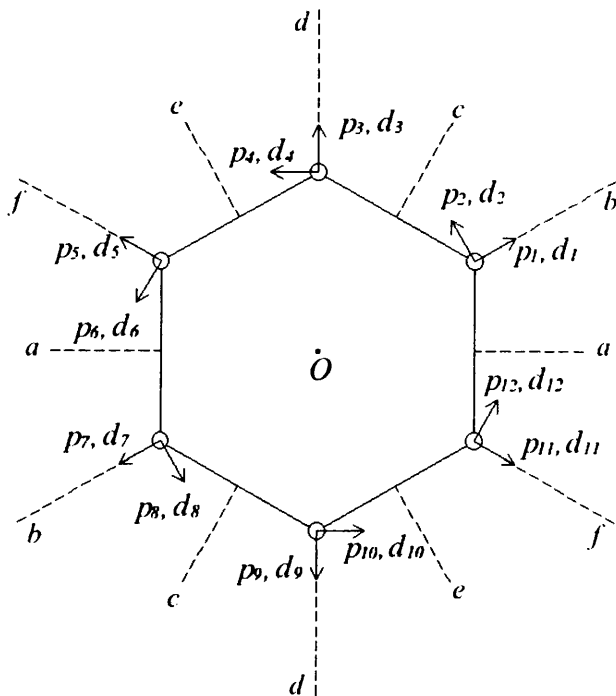


Figure 4.1:

External coordinate system and reflection symmetry planes for the structure of Fig. 3.2. The load and displacement vector components are labelled p_1 to p_{12} and d_1 to d_{12} , respectively and the corresponding basis vectors for the coordinate system are indicated by arrows at each node. The planes of reflection symmetry are labelled a to f .

Figure 4.1 illustrates the coordinate system used to represent components of the generalised displacement vector $\{d\}$ and load vector $\{p\}$ for the reticulate system of Fig 3.2. The 6 planes of reflection symmetry of the structure are indicated by dashed lines and are labelled a to f . The local coordinate systems used to represent nodal displacements and forces are Cartesian and the components of the generalised force or displacement vectors are comprised of nodal coordinate values arranged in cyclic order as shown in the figure. Recall, that the global, polar coordinate system with origin at O is used to represent nodal coordinates and define the direction of basis vectors for the 12-dimensional space in which load and displacement vectors are represented. This vector space is referred to as the “*external vector space*,” and is denoted by the symbol \mathbb{V}_p .

The hexagonal structure is transformed into an equivalent configuration by the following set of symmetry operations:

- 1) The identity, symmetry operation E .
- 2) Rotation by 60° about the origin O , symmetry operation C_6 .
- 3) Rotation by 120° about the origin O , symmetry operation C_6^2 .
- 4) Rotation by 180° about the origin O , symmetry operation C_6^3 .
- 5) Rotation by 240° about the origin O , symmetry operation C_6^4 .
- 6) Rotation by 300° about the origin O , symmetry operation C_6^5 .
- 7) Reflection in the vertical plane a , symmetry operation σ_a .
- 8) Reflection in the vertical plane b , symmetry operation σ_b .
- 9) Reflection in the vertical plane c , symmetry operation σ_c .
- 10) Reflection in the vertical plane d , symmetry operation σ_d .
- 11) Reflection in the vertical plane e , symmetry operation σ_e .
- 12) Reflection in the vertical plane f , symmetry operation σ_f .

These twelve operations $\{E, C_6, C_6^2, C_6^3, C_6^4, C_6^5, \sigma_a, \sigma_b, \sigma_c, \sigma_d, \sigma_e, \sigma_f\}$ constitute a symmetry group C_{6v} .

Once a coordinate system is attached to the structure, the symmetry operations may be represented as matrices which transform vectors defined in this coordinate system. For example, the matrix $[P(E)]$ which acts on load vectors to represent the identity operation, E is the 12×12 identity matrix. Similarly, for each symmetry operation (\cdot) , there is associated a matrix $[P(\cdot)]$, which transforms load vectors, $\{p\}$ and an identical matrix $[D(\cdot)]$ transforms the

displacement vectors, $\{d\}$. These matrices are called reducible matrix representations of the symmetry group C_{6v} .

Due to the particular choice of coordinate system used to represent load and displacement vectors, much of the symmetry of the structure is already reflected in the coordinate system and consequently, the reducible matrix representations are of a particularly simple form. In fact, all the reducible matrix representations in this coordinate system can be obtained by permuting the rows of the identity matrix, with the exception, that the even numbered rows of the matrices representing reflection operations are multiplied by a factor of -1. It follows, that the coordinate transformations due to a particular symmetry operation can be represented in a more compact form as a 12-vector which lists the order of the permutation and any sign changes that result from reflections. As will be shown, the use of these more abstract data types in computer code or hand calculation can significantly reduce the cost and time of decomposing the equilibrium matrix into a block diagonal form using symmetry subspace methods.

Any rotational symmetry operation that transforms the structure into an equivalent configuration simply results in a permutation in the indices or order of components of the force or displacement vectors. The permutation vectors $\{\mathcal{P}(\cdot)\}$ and $\{\mathcal{D}(\cdot)\}$ are used to represent transformed load and displacement vector component indices, respectively, under a symmetry operation (\cdot) . For the hexagonal structure (Fig. 4.1) the permutations of vector components due to the first 6 symmetry operations are given by the following permutations, where by convention, the 12th vector component index is represented by 0.

$$\begin{aligned}
 \{\mathcal{P}(E)\} &= \{\mathcal{D}(E)\} = \{1,2,3,4,5,6,7,8,9,10,11,0\} \\
 \{\mathcal{P}(C_6)\} &= \{\mathcal{D}(C_6)\} = \{11,0,1,2,3,4,5,6,7,8,9,10\} \\
 \{\mathcal{P}(C_6^2)\} &= \{\mathcal{D}(C_6^2)\} = \{9,10,11,0,1,2,3,4,5,6,7,8\} \\
 \{\mathcal{P}(C_6^3)\} &= \{\mathcal{D}(C_6^3)\} = \{7,8,9,10,11,0,1,2,3,4,5,6\} \\
 \{\mathcal{P}(C_6^4)\} &= \{\mathcal{D}(C_6^4)\} = \{5,6,7,8,9,10,11,0,1,2,3,4\} \\
 \{\mathcal{P}(C_6^5)\} &= \{\mathcal{D}(C_6^5)\} = \{3,4,5,6,7,8,9,10,11,0,1,2\}
 \end{aligned} \tag{4.1.1}$$

Although it is clear that there is a one-to-one correspondence between each permutation vector and the corresponding matrix representation for a particular symmetry group, it is more useful to express the symmetry group representations in an alternative form. Firstly, any permutation vector corresponding to a rotational symmetry operation may be obtained as a transformation of the identity permutation using clock arithmetic or *arithmetic modulo 12*.

Definition 3.1: *Modular arithmetic.*

Given two positive integers, b and n , the value of the integer, a , where $a = b \pmod{n}$ (abbreviated as $a = (b) \pmod{n}$), is the remainder obtained from dividing b by n . When b is a negative integer, we use the more general definition for the residual of a congruence relation, that is, $a = (b) \pmod{n} \Rightarrow$ (implies) a is the smallest positive integer such that $(a - b) = cn$, where c is a positive integer. In this case, a is called the residual.

In terms of modular arithmetic, the transformations which represent the symmetry operations C_6 to C_6^5 , may be expressed in the following form, where $\mathcal{P}_i(\cdot)$ denotes the i^{th} component of the vector $\{\mathcal{P}(\cdot)\}$.

$$\begin{aligned}
 \mathcal{P}_i(C_6) &= (\mathcal{P}_i(E) - 2) \pmod{12} && \text{for } i = 1, \dots, 12 \\
 \mathcal{P}_i(C_6^2) &= (\mathcal{P}_i(E) - 4) \pmod{12} && \text{for } i = 1, \dots, 12 \\
 \mathcal{P}_i(C_6^3) &= (\mathcal{P}_i(E) - 6) \pmod{12} && \text{for } i = 1, \dots, 12 \\
 \mathcal{P}_i(C_6^4) &= (\mathcal{P}_i(E) - 8) \pmod{12} && \text{for } i = 1, \dots, 12 \\
 \mathcal{P}_i(C_6^5) &= (\mathcal{P}_i(E) - 10) \pmod{12} && \text{for } i = 1, \dots, 12
 \end{aligned} \tag{4.1.2}$$

For the remaining 6 reflection symmetry operations, the permutation vectors must contain additional information about sign changes of vector components due to reflection. If a symmetry operation acting on the reference configuration results in a sign reversal of a particular basis vector, this is indicated by a negative sign before the transformed index value in the corresponding permutation vector. Thus, the permutation vectors for reflection symmetry operations are represented as follows:

$$\begin{aligned}
 \{\mathcal{P}(\sigma_a)\} &= \{\mathcal{D}(\sigma_a)\} = \{11, -0, 9, -10, 7, -8, 5, -6, 3, -4, 1, -2\} \\
 \{\mathcal{P}(\sigma_b)\} &= \{\mathcal{D}(\sigma_b)\} = \{1, -2, 11, -0, 9, -10, 7, -8, 5, -6, 3, -4\} \\
 \{\mathcal{P}(\sigma_c)\} &= \{\mathcal{D}(\sigma_c)\} = \{3, -4, 1, -2, 11, -0, 9, -10, 7, -8, 5, -6\} \\
 \{\mathcal{P}(\sigma_d)\} &= \{\mathcal{D}(\sigma_d)\} = \{5, -6, 3, -4, 1, -2, 11, -0, 9, -10, 7, -8\} \\
 \{\mathcal{P}(\sigma_e)\} &= \{\mathcal{D}(\sigma_e)\} = \{7, -8, 5, -6, 3, -4, 1, -2, 11, -0, 9, -10\} \\
 \{\mathcal{P}(\sigma_f)\} &= \{\mathcal{D}(\sigma_f)\} = \{9, -10, 7, -8, 5, -6, 3, -4, 1, -2, 11, -0\}
 \end{aligned} \tag{4.1.3}$$

Similarly, the transformations which express the permutation vectors in terms of the components of the identity permutation are of the following form;

$$\begin{aligned}
p_i(\sigma_a) &= \begin{cases} (-p_i(E)) \bmod 12 & \text{for } i \text{ odd} \\ -((2 - p_i(E)) \bmod 12) & \text{for } i \text{ even} \end{cases} \\
p_i(\sigma_b) &= \begin{cases} (2 - p_i(E)) \bmod 12 & \text{for } i \text{ odd} \\ -((4 - p_i(E)) \bmod 12) & \text{for } i \text{ even} \end{cases} \\
p_i(\sigma_c) &= \begin{cases} (4 - p_i(E)) \bmod 12 & \text{for } i \text{ odd} \\ -((6 - p_i(E)) \bmod 12) & \text{for } i \text{ even} \end{cases} \\
p_i(\sigma_d) &= \begin{cases} (6 - p_i(E)) \bmod 12 & \text{for } i \text{ odd} \\ -((8 - p_i(E)) \bmod 12) & \text{for } i \text{ even} \end{cases} \\
p_i(\sigma_e) &= \begin{cases} (8 - p_i(E)) \bmod 12 & \text{for } i \text{ odd} \\ -((10 - p_i(E)) \bmod 12) & \text{for } i \text{ even} \end{cases} \\
p_i(\sigma_f) &= \begin{cases} (10 - p_i(E)) \bmod 12 & \text{for } i \text{ odd} \\ -((-p_i(E)) \bmod 12) & \text{for } i \text{ even} \end{cases} \tag{4.1.4}
\end{aligned}$$

Note that in order for the transformations to form a true representation of the symmetry group C_{6v} it is necessary that the transformations form a group which has the same multiplication table as the abstract group C_{6v} . This requires a more general definition of the transformations which hold for compositions of symmetry operations.

The permutation vectors generated from sequences of symmetry operations leads to the following general definition, which expresses the new permutation $\{\mathcal{P}((\cdot) \circ (\cdot))\}$ in terms of components of the previous permutation $\{\mathcal{P}(\cdot)\}$, where $(\cdot) \circ (\cdot)$ signifies the composition of two symmetry operations, (\cdot) and (\cdot) .

$$p_i(C_6^\alpha \circ (\cdot)) = p_k(\cdot) \quad , k = (i - 2\alpha) \bmod 12 \quad \text{for } i = 0, \dots, 11 \tag{4.1.5}$$

$$p_j(\sigma_\beta \circ (\cdot)) = \begin{cases} p_l(\cdot) & , l = (2\beta - j) \bmod 12 & \text{for } j \text{ odd} \\ -p_l(\cdot) & , l = (2(1 + \beta) - j) \bmod 12 & \text{for } j \text{ even} \end{cases} \tag{4.1.6}$$

where $\alpha = 1, \dots, 5$ and $\beta = 0, \dots, 5$.

For consistency it is assumed that $p_0(\cdot)$ represents the 12th component of the vector, $\{\mathcal{P}(\cdot)\}$. Note that when the identity operation E is substituted for (\cdot) in Eq. (4.1.5) and (4.1.6), the transformations produce identical results to those of Eq. (4.1.2) and (4.1.4), however when a symmetry operation is chosen arbitrarily to represent (\cdot) , the results obtained are consistent with the multiplication rules for the group C_{6v} . Therefore the transformations form a consistent representation of the symmetry group C_{6v} .

invariant subspaces $\mathbb{V}_i^{(\mu)}$, each operated on by a particular irreducible representation, $\Gamma_i^{(\mu)}$ (Kangwai et al. 1999).

Table 4.1:

Irreducible representations of symmetry group C_{6v}

C_{6v}	E	C_6	C_6^2	C_6^3	C_6^4	C_6^5
$\Gamma^{(A_1)}$	1	1	1	1	1	1
$\Gamma^{(A_2)}$	1	1	1	1	1	1
$\Gamma^{(B_1)}$	1	-1	1	-1	1	-1
$\Gamma^{(B_2)}$	1	-1	1	-1	1	-1
$\Gamma^{(E_1)}$	$\begin{bmatrix} 1 & 0 \\ 0 & 1 \end{bmatrix}$	$\begin{bmatrix} 1/2 & -\sqrt{3}/2 \\ \sqrt{3}/2 & 1/2 \end{bmatrix}$	$\begin{bmatrix} -1/2 & -\sqrt{3}/2 \\ \sqrt{3}/2 & -1/2 \end{bmatrix}$	$\begin{bmatrix} -1 & 0 \\ 0 & -1 \end{bmatrix}$	$\begin{bmatrix} -1/2 & \sqrt{3}/2 \\ -\sqrt{3}/2 & -1/2 \end{bmatrix}$	$\begin{bmatrix} 1/2 & \sqrt{3}/2 \\ -\sqrt{3}/2 & 1/2 \end{bmatrix}$
$\Gamma^{(E_2)}$	$\begin{bmatrix} 1 & 0 \\ 0 & 1 \end{bmatrix}$	$\begin{bmatrix} -1/2 & -\sqrt{3}/2 \\ \sqrt{3}/2 & -1/2 \end{bmatrix}$	$\begin{bmatrix} -1/2 & \sqrt{3}/2 \\ -\sqrt{3}/2 & -1/2 \end{bmatrix}$	$\begin{bmatrix} 1 & 0 \\ 0 & 1 \end{bmatrix}$	$\begin{bmatrix} -1/2 & -\sqrt{3}/2 \\ \sqrt{3}/2 & -1/2 \end{bmatrix}$	$\begin{bmatrix} -1/2 & -\sqrt{3}/2 \\ -\sqrt{3}/2 & -1/2 \end{bmatrix}$
σ_a	σ_b	σ_c	σ_d	σ_e	σ_f	
1	1	1	1	1	1	
-1	-1	-1	-1	-1	-1	
1	-1	1	-1	1	-1	
-1	1	-1	1	-1	1	
$\begin{bmatrix} 1 & 0 \\ 0 & -1 \end{bmatrix}$	$\begin{bmatrix} 1/2 & \sqrt{3}/2 \\ \sqrt{3}/2 & -1/2 \end{bmatrix}$	$\begin{bmatrix} -1/2 & \sqrt{3}/2 \\ \sqrt{3}/2 & 1/2 \end{bmatrix}$	$\begin{bmatrix} -1 & 0 \\ 0 & 1 \end{bmatrix}$	$\begin{bmatrix} -1/2 & -\sqrt{3}/2 \\ -\sqrt{3}/2 & 1/2 \end{bmatrix}$	$\begin{bmatrix} 1/2 & -\sqrt{3}/2 \\ -\sqrt{3}/2 & -1/2 \end{bmatrix}$	
$\begin{bmatrix} 1 & 0 \\ 0 & -1 \end{bmatrix}$	$\begin{bmatrix} -1/2 & \sqrt{3}/2 \\ \sqrt{3}/2 & 1/2 \end{bmatrix}$	$\begin{bmatrix} -1/2 & -\sqrt{3}/2 \\ -\sqrt{3}/2 & 1/2 \end{bmatrix}$	$\begin{bmatrix} 1 & 0 \\ 0 & -1 \end{bmatrix}$	$\begin{bmatrix} -1/2 & \sqrt{3}/2 \\ \sqrt{3}/2 & 1/2 \end{bmatrix}$	$\begin{bmatrix} -1/2 & -\sqrt{3}/2 \\ -\sqrt{3}/2 & 1/2 \end{bmatrix}$	

A geometrical interpretation of the symmetry adapted coordinates is given by Kangwai et al. (1999) and Kangwai (1997). Furthermore, it has been shown by Kangwai et al. (1999) or Healey and Treacy (1991) that it is possible to split the vector spaces \mathbb{V}_p or \mathbb{V}_f of a symmetric structure into symmetry subspaces which each correspond to a row of the irreducible representations of the group. The notation used to describe symmetry subspaces is presented as follows. (Kangwai et al., 1999)

Firstly, the subspace $V^{(\mu)}$ of V , which corresponds to a particular type of symmetry of the structure, is represented as a summation of irreducible invariant subspaces $V_i^{(\mu)}$, i.e.

$$V^{(\mu)} = V_1^{(\mu)} + V_2^{(\mu)} + \dots + V_{\alpha_\mu}^{(\mu)} \quad (4.2.2)$$

Secondly, the subspaces $V^{(\mu)}$ which correspond to $\Gamma^{(\mu)}$ bigger than 1×1 , are further split into subspaces, each of which correspond to a particular row of the representation $\Gamma^{(\mu)}$. It is these subspaces which are referred to as the symmetry subspaces, $V^{(\mu)i}$.

The symmetry subspaces, $V^{(\mu)i}$ may be represented by basis vectors in the original coordinate system of the vector space V and consequently, the symmetry-adapted coordinates are never used directly in calculations. As a result of the great orthogonality theorem, it can be shown that the basis vectors for the symmetry subspaces can be generated automatically in the original coordinate system using only the matrices of the reducible and irreducible representations of the corresponding symmetry group. (Kangwai et al., 1999)

In its simplest form, the great orthogonality theorem states that each one-dimensional irreducible representation or particular component of a higher-dimensional irreducible representation is orthogonal to every other one-dimensional irreducible representation or component of a higher-dimensional representation.

Here, it is understood that a one-dimensional irreducible representation or component of a higher-dimensional irreducible representation can be represented by a vector whose length is equal to the number of symmetry operations of the symmetry group and whose components correspond to specific symmetry operations. We use the symbol $\{\Gamma_{ij}^{(\mu)}\}$ to denote the vector corresponding to the i, j component of a higher-dimensional irreducible matrix representation $\Gamma^{(\mu)}$. The validity of the great orthogonality theorem can be easily verified for a particular symmetry group and a proof is given by Flurry, (1980).

Kangwai et al. (1999) present the following method for obtaining the basis vectors for the symmetry subspaces based on the great orthogonality theorem.

Corollary 4.1:

- 1) Consider a linear combination of the matrices of a reducible representation, where each matrix is multiplied by the corresponding irreducible representation (or the i, j component of a higher-dimensional irreducible matrix representation) to obtain the projection operator matrix $[O_{ij}^{(\mu)}]$.

2) The column space of $[O_{ij}^{(\mu)}]$ will be the symmetry subspace $\mathbb{V}^{(\mu)i}$.

The validity of this result and physical interpretation of the basis vectors is discussed further by Kangwai et al. (1999) and Kangwai (1997).

4.2.2 Block-diagonal form of the equilibrium and flexibility matrices

In principle, any vector $\{\zeta\}$ in the space \mathbb{V} may be represented as a linear combination of the basis vectors $\{v_s\}$ $s = 1, \dots, n$ ($n = \dim(\mathbb{V})$) of the symmetry subspaces, $\mathbb{V}^{(\mu)i}$. Such a representation may be expressed as

$$\{\zeta\} = \sum_s \tilde{\alpha}_s \{v_s\} \quad (4.2.3)$$

where the components, $\tilde{\alpha}_s$ are called the symmetry-adapted coordinates of $\{\zeta\}$, and the collection of basis vectors $\{v_s\}$ are referred to as the symmetry-adapted basis. Note that the basis vectors are represented in the original coordinate system.

In matrix notation Eq. (4.2.3) can be expressed in the following form;

$$\{\zeta\} = [V]\{\tilde{\alpha}\} \quad (4.2.4)$$

Here, the orthogonal matrix $[V] = [\{v_1\}, \{v_2\}, \dots, \{v_n\}]$ is the transformation matrix, which transforms vectors from the symmetry-adapted basis to the original coordinate system. The matrix $[V]$, alternatively referred to as the symmetry-adapted vector basis, is assembled from the basis matrices $[V^{(\mu)i}]$ which represent the symmetry subspaces, $\mathbb{V}^{(\mu)i}$. The matrices $[V^{(\mu)i}]$ are obtained by applying Corollary 3.1, and the matrix $[V]$ is partitioned according to the symmetry subspaces. As an example, for the symmetry group C_{6v} the matrix $[V]$ may be partitioned as follows;

$$[V] = \left[\begin{array}{c|c|c|c|c|c|c|c} [V^{(A1)}] & [V^{(A2)}] & [V^{(B1)}] & [V^{(B2)}] & [V^{(E1)1}] & [V^{(E1)2}] & [V^{(E2)1}] & [V^{(E2)2}] \end{array} \right] \quad (4.2.5)$$

For a general symmetric structure it is possible, using group representation theory, to decompose the two vector spaces \mathbb{V}_p and \mathbb{V}_f of the structure into symmetry subspaces $\mathbb{V}_p^{(\mu)i}$ and $\mathbb{V}_f^{(\mu)i}$ and find the corresponding symmetry-adapted vector bases $[V_p]$ and $[V_f]$, respectively. The choice of a 'natural' coordinate system for representing the internal bar-force and bar-elongation vector space \mathbb{V}_f of a reticulate assembly is discussed by Kangwai and Guest (2000). In this particular coordinate system the reducible matrix representations of the symmetry

group of the structure are simply obtained by permuting the rows of the identity matrix. These permutation matrices can alternatively be represented by permutation vectors similar to those used to represent the symmetry operations of the example structure (Figure 3.3) in the external coordinate system.

Although the two vector spaces \mathbb{V}_p and \mathbb{V}_f will, in general, have different coordinate systems and be of different dimension, the partitioning of the matrices $[V_p]$ and $[V_f]$ according to the symmetry subspaces only depends on the symmetry group of the structure and, for a structure with C_{6v} symmetry, has the general form. Moreover, for a stable linear system, any load vector with the particular symmetry properties of symmetry subspace $\mathbb{V}_p^{(\mu)i}$, will induce bar-force and bar-elongation vectors from the corresponding symmetry subspace $\mathbb{V}_f^{(\mu)i}$, which has the same symmetry properties (Kangwai and Guest, 2000). It follows, that the equilibrium matrix $[A]$ can be block-diagonalised into independent submatrix blocks and the block-diagonal form of $[A]$ may be obtained by applying the transformation matrices $[V_p]$ and $[V_f]$ to corresponding load and bar force vectors $\{p\}$ and $\{f\}$ which appear in the equilibrium equation (3.1.1). Thus,

$$\{p\} = [V_p]\{\tilde{p}\} \quad (4.2.6)$$

$$\{f\} = [V_f]\{\tilde{f}\} \quad (4.2.7)$$

Substituting (4.2.6) and (4.2.7) into (3.1.1) and multiplying both sides by $[V_p]^t$ the desired, block-diagonal form of the equilibrium matrix is obtained;

$$\left([V_p]^t[A][V_f]\right)\{\tilde{f}\} = \{\tilde{p}\} \quad (4.2.8)$$

Hence, the symmetry-adapted equilibrium equation may be written as;

$$[\tilde{A}]\{\tilde{f}\} = \{\tilde{p}\} \quad (4.2.9)$$

where $[\tilde{A}] = \left([V_p]^t[A][V_f]\right)$ and the vectors $\{\tilde{f}\}$ and $\{\tilde{p}\}$ are defined in the symmetry adapted vector bases $[V_f]$ and $[V_p]$, respectively.

Similarly, the block-diagonal compatibility and flexibility matrices are given by;

$$[\tilde{A}]^t = \left([V_f]^t[A]^t[V_p]\right) \quad (4.2.10)$$

$$[\tilde{F}] = \left([V_f]^t[F][V_f]\right) \quad (4.2.11)$$

The symmetry-adapted equilibrium matrix $[\tilde{A}]$ consists of a number of independent submatrix blocks $[\tilde{A}^{(\mu)i}]$, each of which operate on a pair of symmetry-adapted load and bar-force vectors $\{\tilde{p}^{(\mu)i}\}$ and $\{\tilde{f}^{(\mu)i}\}$ in the corresponding symmetry subspaces $V_p^{(\mu)i}$ and $V_f^{(\mu)i}$. If the full symmetry of a structure is characterised by the symmetry group C_{6v} , the corresponding symmetry-adapted equilibrium matrix will be composed of 8 independent submatrix blocks. Since each matrix block may be solved individually to give the induced bar-force vectors in equilibrium with the applied load vectors, the original full problem (Eq. (3.1.1)) has been decomposed into 8 smaller sub-problems,

$$[\tilde{A}^{(\mu)i}]\{\tilde{f}^{(\mu)i}\} = \{\tilde{p}^{(\mu)i}\} \quad (4.2.12)$$

Each equation of the form (4.2.12), expresses the relationship between load and bar-force vectors which have a particular type of symmetry.

In practice, it is not necessary to compute the entire block-diagonal equilibrium matrix, since the equilibrium matrix blocks $[\tilde{A}^{(\mu)i}]$ can be calculated separately, and are given by;

$$[\tilde{A}^{(\mu)i}] = [V_p^{(\mu)i}]^t [A] [V_f^{(\mu)i}] \quad (4.2.13)$$

4.3 Assembly of symmetry-adapted vector basis matrices

Although the symmetry subspace method presented in this chapter is intended to reduce computational costs and simplify the static analysis of symmetric structures, there may be cases for which the additional cost of generating the symmetry-adapted vector basis, for a specific structure, outweighs the cost advantages. To address this problem it is necessary to develop the most efficient implementation of the method in computer code or hand calculation. Even so, for relatively small problems with low-order symmetry, the cost of decomposition and final superposition may not justify the approach (Zingoni, 2009).

The advantage of using the irreducible representations of a group directly in generating the symmetry subspaces is that the method is generally applicable to any structure with point-group symmetry and exploits the full symmetry of the structure to systematically simplify the analysis. However, for problems involving only one-dimensional irreducible representations, the symmetry subspaces can be found by a simpler and quicker method, called G-vector analysis, which uses the idempotents of a symmetry group. Since most problems of interest involve symmetry subspaces associated with higher order irreducible representations, the former

approach has a particular advantage, since these subspaces are split directly into smaller subspaces, without the additional considerations required in the G-vector method. (Kangwai et al., 1999; Zingoni, 2009)

In order to develop a general approach for the static analysis of symmetric structures which can be easily implemented in computer code, it is necessary to consider more efficient ways of generating the symmetry-adapted variables of a problem using the irreducible representations of a group. According to Corollary 4.1, the first step in generating the symmetry-adapted basis vectors is to assemble the projection operator matrices, $[O_{ij}^{(\mu)}]$. Although for more simple structures these matrices can be assembled and processed by hand, in the following, a more direct method is presented, which is also suitable for implementing in code and avoids the problem of storing and manipulating large, sparse matrices.

For any cyclically symmetric structure it is possible to assemble the projection operator matrices using permutation vectors similar to those used to represent the reducible matrix representations of the symmetry group C_{6v} for the example structure of Figure 3.3. However, it is first necessary to represent the permutation vectors in a format which is more suitable for manipulating in a computer program. Essentially, for a permutation vector of length n , representing the n degrees of freedom of a general symmetric structure, the n^{th} degree of freedom should be represented, in permutation vectors, by the values $\pm n$ as oppose to ± 0 , which were used previously for pedagogical reasons.

The following algorithm (Box 4.1) gives an efficient implementation for automatically generating the permutation vectors, $\{\mathcal{P}(\cdot)\}$ which represent the action of symmetry operations on vectors in the space V_p , for a structure with C_{6v} symmetry. For simplicity, the algorithm is sufficiently general to apply to any two-dimensional reticulate assembly with C_{6v} symmetry, for which there are two degrees of freedom at each unconstrained node and a total of n degrees of freedom. It is further assumed that the initial coordinate system is represented by basis vectors which coincide with those of the global, polar coordinate system, as described for the example structure (Figure 3.1, 3.2) and that no two nodes have the same polar angle.

$$p_1(C_6^\alpha) = \left(1 + \left(1 - \frac{\alpha}{6}\right)n\right) \bmod n$$

$$k_\alpha = n + 1 - p_1(C_6^\alpha)$$

$$p_j(C_6^\alpha) = \begin{cases} j - k_\alpha + n & \text{for } j = 2, \dots, k_\alpha \\ j - k_\alpha & \text{for } j = k_\alpha + 1, \dots, n \end{cases}$$

where $\alpha = 1, \dots, 5$

$$p_1(\sigma_\beta) = \left(\left(1 + \frac{\beta}{6}\right)n - 1\right) \bmod n$$

$$k_\beta = \frac{1}{2}(p_1(\sigma_\beta) + 1)$$

$$p_{2j-1}(\sigma_\beta) = \begin{cases} 2(k_\beta - j) + 1 & \text{for } j = 2, \dots, k_\beta \\ 2(k_\beta - j) + 1 + n & \text{for } j = k_\beta + 1, \dots, \frac{n}{2} \end{cases}$$

$$p_{2j}(\sigma_\beta) = -(p_{2j-1}(\sigma_\beta) + 1) \quad \text{for } j = 1, \dots, \frac{n}{2}$$

where $\beta = 0, \dots, 5$.

Box 4.1: "Algorithm 4.1": automatically generates permutation vectors which represent the symmetry group of a structure in the external polar coordinate system.

More complex algorithms can be designed to generate the symmetry group representations for more general, cyclically symmetric structures, such as three-dimensional structures with different element types and joint constraints. Provided the basis vectors for the external coordinate system coincide with the basis vectors of the global, polar coordinate system at each node, the reducible representations of the symmetry group of the structure can always be represented in a simplified form as a sequence of permutation vectors. Special care must be taken when any set of nodes have the same polar angle. In this case it is convenient to group nodes which have the same polar angle together, since their external vectors are transformed identically by any symmetry operation of the point group. Hence, for the purpose of generating the symmetry group representations, nodes which have the same polar angle are labelled with identical indices and it is required to renumber the remaining index values accordingly.

The first statement of Corollary 4.1 can be conveniently represented in matrix notation. If I_k denotes the k^{th} symmetry operation of the symmetry group for a structure, the projection operator matrices can be expressed in the following form;

$$[\mathbf{O}_{ij}^{(\mu)}] = \sum_k \{\Gamma_{ij}^{(\mu)}\}_k [\mathbf{P}(I_k)] \quad (4.3.1)$$

Alternatively, the projection operator matrix may be assembled column wise using permutation vectors, $\{\mathcal{P}(I_k)\} = \{\mathcal{P}_1(I_k), \dots, \mathcal{P}_l(I_k), \dots, \mathcal{P}_n(I_k)\}$. The following algorithm performs the assembly of the l^{th} column of the projection operator matrix, $[\mathbf{O}_{ij}^{(\mu)}]$ by iteration over the index k , which for the symmetry group C_{6v} ranges from 1 to 12. At the k^{th} iteration step the k^{th} component of (the i, j component of) an irreducible representation (corresponding to the k^{th} symmetry operation) is added (or subtracted) to a component, $[\mathbf{O}_{ij}^{(\mu)}]_{\alpha l}$ of the l^{th} column of $[\mathbf{O}_{ij}^{(\mu)}]$.

for $k = 1, \dots, 12$ {

$\alpha = |\mathcal{P}_l(I_k)|$;

$\beta = \frac{\mathcal{P}_l(I_k)}{\alpha}$;

$[\mathbf{O}_{ij}^{(\mu)}]_{\alpha l} = [\mathbf{O}_{ij}^{(\mu)}]_{\alpha l} + \beta \{\Gamma_{ij}^{(\mu)}\}_k$;

}

Box 4.2: "Algorithm 4.2": iterative assembly of the l^{th} column of the projection operator matrix from components of the irreducible representations using permutation vectors.

The relative efficiency of the new algorithm (Box 4.2) compared to the matrix version can be easily deduced by counting the number of basic numerical operations required to perform each version of the matrix assembly in code. In the form of Eq. (4.3.1) the assembly of the $n \times n$ projection operator matrix would require Kn^2 multiplications and Kn^2 additions, where K is the total number of symmetry operations of the group. Hence, the assembly of the matrix $[\mathbf{O}_{ij}^{(\mu)}]$ as a linear combination of the matrices $[\mathbf{P}(I_k)]$ would involve approx. $O(n^2)$ numerical operations, assuming there were no additional mechanisms in place to simplify the manipulation of sparse matrices. From Algorithm 4.1 it is clear that the parameters α and β need not be computed at each step of Algorithm 4.2 since by a small modification of Algorithm 4.1 they can be separated immediately and then used directly in Algorithm 4.2. Hence, only the third line within the for loop needs to be considered to determine the number of numerical operations required to perform the assembly of the matrix $[\mathbf{O}_{ij}^{(\mu)}]$. In this case there are K additions (or subtractions) per column

of the matrix, so the total number of operations required to perform the assembly of the matrix $\left[\mathbf{O}_{ij}^{(\mu)} \right]$ using Algorithm 4.2 is approx. $O(n)$.

The speed of Algorithm 4.2 can also be improved by implementing the outer loop, over the index l , in parallel i.e. the columns of the matrix can be assembled simultaneously using parallel programming techniques (or code vectorization in MATLAB). Also, in practice, it is not usually necessary to assemble the entire matrix $\left[\mathbf{O}_{ij}^{(\mu)} \right]$ since only the first few columns (or only one column) are required. Using symmetry arguments it is usually possible to know in advance the dimension of the column space of each matrix $\left[\mathbf{O}_{ij}^{(\mu)} \right]$ [Kangwai et al., 1999]. Algorithm 4.2 is in an ideal form for generating a sequence of vectors; the columns of $\left[\mathbf{O}_{ij}^{(\mu)} \right]$; for which an orthonormal basis can be generated automatically using, e.g. the Gram-Schmidt orthogonalization algorithm. Since the dimensions of the symmetry subspaces are known a priori, a useful stopping criterion for the algorithm is provided, so that all the columns of the matrices $\left[\mathbf{O}_{ij}^{(\mu)} \right]$ need never be generated.

Due to the particular choice of the initial coordinate system it is evident that the matrices $\left[\mathbf{P}(I_k) \right]$ would only contain signed integer data and in most cases the irreducible representations, $\left\{ \Gamma_{ij}^{(\mu)} \right\}$ can be scaled appropriately so that the values $\left\{ \Gamma_{ij}^{(\mu)} \right\}_k$ in eqn , can also be represented by integers. Hence the (scaled) matrices $\left[\mathbf{O}_{ij}^{(\mu)} \right]$ can be represented by signed integer data and generated using only integer operations. For large data sets, using the integer data type significantly increases the speed and efficiency with which the matrix column vectors can be generated by Algorithm 4.2.

4.4 Analysis of the symmetry sub-structure

By definition, a structure with symmetry properties consists of a repeating symmetry sub-structure, i.e. a segment that generates the entire structure by repetitions of itself. For example, for the structure of Figure 3.2, the elements 1 and 2 can serve as the repeating symmetry sub-structure. It was also shown, in section 3.2, that if a polar coordinate system was used to represent load and displacement vectors (Fig. 3.3), the equilibrium matrix of the structure had a simple, hyper-cyclic form. Intuitively it is clear that the rotational symmetry of the structure is reflected in the form of the equilibrium matrix due to the choice of coordinates. This can be

explained more rigorously when it is understood how the equilibrium matrix, $[A]$ of the entire structure can be generated from the equilibrium matrix, $[H]$ of the symmetry substructure.

Following the formulation presented by Kangwai (1997), for any symmetric structure, the equilibrium matrix of the entire structure may be written as a sum of matrices $[A_1], \dots, [A_q], \dots, [A_n]$ corresponding to the n repetitions of the symmetry sub-structure;

$$[A] = \sum_{q=1}^n [A_q] \quad (4.4.1)$$

where each matrix $[A_q]$ can be generated from $[H]$ by a coordinate transformation from the local to the global coordinate systems, for both the internal and external vector spaces.

Since the global equilibrium matrices $[A_q]$ operate on load vectors $\{p\}$ and bar-force vectors $\{f\}$, for each matrix $[A_q]$ there are associated transformation matrices $[Q_q]$ and $[S_q]$, such that;

$$\{p\} = [Q_q]^t \{p'\} \quad (4.4.2)$$

$$\{f\} = [S_q]^t \{f'\} \quad (4.4.3)$$

where $\{p'\}$ and $\{f'\}$ are corresponding vectors in the local coordinate system of the symmetry sub-structure. Combining Eq. (4.4.2) and (4.4.3) with the equilibrium equation $[H]\{f'\} = \{p'\}$ for the symmetry substructure gives;

$$[A_q] = [Q_q]^t [H] [S_q] \quad (4.4.4)$$

It is clear that the transformation matrices $[Q_q]$ and $[S_q]$ will be of the simplest form when the local vector coordinates are coincident with the global coordinate system after a rotation of the symmetry sub-structure. For example, using the polar coordinate system (Figure 3.3) to represent load vectors, the equilibrium matrix, $[H]$ for the sub-structure comprised of elements 1 and 2 of the hexagonal structure of Figure 3.2 may be assembled from the element vectors (Eq. (3.2.14) and (3.2.15)) and can be expressed as;

$$[H] = \begin{bmatrix} K \\ L \end{bmatrix} \quad (4.4.5)$$

where the sub-matrices $[K]$ and $[L]$ are given by Eq. (3.2.17).

Comparing with the global equilibrium matrix, $[A]$ given by Eq. (3.2.16) the form of the matrices $[A_q]$ can be immediately deduced. Furthermore, the particular choice of coordinates and element numbering generates the simplest form possible for the transformation matrices $[Q_q]$

and $[S_q]$. For example, the global matrix $[A_2]$ generated by an anticlockwise rotation of the symmetry sub-structure by 60° can be expressed as follows;

$$[A_2] = \begin{bmatrix} \check{0} & K & \dots & \check{0} \\ & L & \check{0} & \\ \vdots & & \check{0} & \check{0} \\ \check{0} & & & \check{0} \\ \vdots & & & \check{0} \\ \check{0} & \dots & \check{0} & \dots & \check{0} \end{bmatrix} = \begin{bmatrix} I & \check{0} \\ \check{0} & I \\ \vdots & \vdots \\ \check{0} & \check{0} \\ \vdots & \vdots \\ \check{0} & \check{0} \end{bmatrix} \begin{bmatrix} [K] \\ [L] \end{bmatrix} [\check{0} \quad I \quad \check{0} \quad \dots \quad \dots \quad \check{0}] \quad (4.4.6)$$

where,

$$[I] = \begin{bmatrix} 1 & 0 \\ 0 & 1 \end{bmatrix}, \quad [\check{0}] = \begin{bmatrix} 0 & 0 \\ 0 & 0 \end{bmatrix} \quad (4.4.7)$$

The corresponding transformation matrices are then given by,

$$[Q_2] = \begin{bmatrix} I & \check{0} & \check{0} & \dots & \dots & \check{0} \\ \check{0} & I & \check{0} & \dots & \dots & \check{0} \end{bmatrix} \quad (4.4.8)$$

$$[S_2] = [\check{0} \quad I \quad \check{0} \quad \dots \quad \dots \quad \check{0}] \quad (4.4.9)$$

The remaining sub-structure transformation matrices for the entire structure can be similarly derived and have the same basic form. These results can obviously be extended to any cyclically symmetric structure for which the coordinate systems have been appropriately chosen.

For structural analysis involving symmetry-adapted equilibrium matrices a more practical implementation of the symmetry subspace method is described in Kangwai (1997) in which simple sub-structuring techniques are applied to generate the equilibrium submatrix blocks, $[\tilde{A}^{(\mu)i}]$ directly from the equilibrium matrix of a repeating substructure. The derivation of this method is given as follows (as formulated by Kangwai (1997)).

Substituting Eq. (4.4.4) into (4.4.1) yields;

$$[A] = \sum_{q=1}^n [Q_q]^t [H] [S_q] \quad (4.4.10)$$

Hence, from Eq. (4.2.13) by substituting for $[A]$ the symmetry-adapted equilibrium blocks are expressed in terms of the substructure equilibrium matrix $[H]$ as;

$$[\tilde{A}^{(\mu)i}] = \sum_{q=1}^n [V_p^{(\mu)i}]^t [Q_q]^t [H] [S_q] [V_f^{(\mu)i}] \quad (4.4.11)$$

The matrices $[V_{p_q}^{(\mu)i}] = [Q_q] [V_p^{(\mu)i}]$ and $[V_{f_q}^{(\mu)i}] = [S_q] [V_f^{(\mu)i}]$ describe the transformation of load and bar-force vectors from the external and internal symmetry spaces $V_p^{(\mu)i}$ and $V_f^{(\mu)i}$ to the symmetry subspace $V_{p_q}^{(\mu)i}$ and $V_{f_q}^{(\mu)i}$, corresponding to symmetry sub-structure q . Using this notation, Eq. (4.4.11) can then be written as:

$$[\tilde{A}^{(\mu)i}] = \sum_{q=1}^n [V_{p_q}^{(\mu)i}]^t [H] [V_{f_q}^{(\mu)i}] \quad (4.4.12)$$

Thus, the independent blocks of the block-diagonalised equilibrium matrix can be calculated directly from the equilibrium matrix $[H]$ of a sub-structure, eliminating the need to assemble the full equilibrium matrix.

3.2 References

Bossavit A. (1986). Symmetry, groups and boundary value problems, a progressive introduction to noncommutative harmonic analysis of partial differential equations in domains with geometrical symmetry. *Comp. Meth. in App. Mech. and Engng*, 56, pp. 167-215

Healey, T.J. and Treacy J.A. (1991). Exact block diagonalisation of large eigenvalue problems for structures with symmetry. *Int. J. Numer. Meth. in Engng*, 31, pp. 265-285

Kangwai, R.D. (1997). The analysis of symmetric structures using group representation theory. Ph.D. thesis, University of Cambridge.

Kangwai, R.D., Guest, S.D and Pellegrino, S. (1999) An introduction to the analysis of symmetric structures. *Computers and Structures*, 71, pp. 671-688.

Kangwai, R.D. and Guest, S.D. (2000). Symmetry-adapted equilibrium matrices. *Int. J. Solids Structures*, 37, pp. 1525-1548.

Zingoni, A. (2009). Group-theoretic exploitations of symmetry in computational solid and structural mechanics. *Int. J. Numer. Meth. Engng*, 79, pp. 253-289

Chapter 5 Analysis of Internal Mechanisms, and Prestress States for Tensegrity Structures

5.1 Rigidity Theory

The stability and rigidity of cabled structures are largely determined by the feasibility of prestressing and overall level of prestress in the structure. An assignment of a scalar value to each member represents a prestress or self-stress, if there is a balance of forces at each vertex in the absence of external loads. In order for a tensegrity to have a “feasible” or “proper” self-stress, it is necessary that any prestressed cable should be in tension. If, in addition, struts are included, designed specifically to resist only compressive loads, a proper self-stress must be non-tensile on such members. A proper self-stress is “strict” if, in addition, the stress is non-zero on every strut and cable. Typically, the compressive members act as bars and may resist either tensile or compressive forces, in which case the self-stress may take any value that satisfies the equilibrium conditions.

5.1.1 *Infinitesimal rigidity*

In rigidity theory, there is a strong connection between self-stresses and rigidity which applies to tensegrities (Connelly and Whiteley, 1996). The notion of infinitesimal rigidity, which is equivalent to kinematic determinacy for a truss may be generalised to tensegrities by introducing the modified constraint equations for struts and cables. Using results from rigidity theory, it can be shown that a tensegrity is infinitesimally rigid, provided it admits a strict, proper self-stress and the corresponding truss, obtained by replacing each strut and cable by a bar is kinematically determinate (Roth and Whiteley, 1981; Demaine and O’Rourke, 2007). The following derivation of the theoretical principles of infinitesimal rigidity for tensegrity structures is adapted from (Demaine and O’Rourke, 2007).

For a truss, an infinitesimal mechanism is characterised by its property that any first order displacement of the vertices preserves the length of each bar to the first order. More generally, if we have a smooth motion of the vertices starting at some configuration at “time 0”, a first order infinitesimal mechanism is defined as the first derivative of the motion at time 0. A truss or linkage is said to be “infinitesimally rigid,” or “first order rigid,” if it has no infinitesimal mechanisms (excluding rigid body motions).

Similarly, first order rigidity for tensegrity structures may be defined as follows:

Definition 5.1 (Connelly and Whiteley, 1996):

“A tensegrity is first order rigid if the only smooth motion of the vertices, such that the extension of each member is compatible with the member constraints at first order, has its derivative at time 0 equal to that of a rigid body motion of the assembly”

The member constraints on an infinitesimal motion are derived as follows:

Suppose the initial configuration is given by a set of point vectors, where $\{p_i\}$ is the coordinate vector for node i . Similarly, a first order motion is assigned to each node and given by a velocity vector $\{v_i\}$. Then, the extension of a member, Δl_{ij} connecting vertices i and j , satisfies the following proportional relationship,

$$\begin{aligned}\Delta l_{ij} &\propto \{v_j\} \cdot (\{p_j\} - \{p_i\}) - \{v_i\} \cdot (\{p_j\} - \{p_i\}) \\ &= (\{v_j\} - \{v_i\}) \cdot (\{p_j\} - \{p_i\}) \\ &= (\{v_i\} - \{v_j\}) \cdot (\{p_i\} - \{p_j\}).\end{aligned}$$

Thus, the constraints on an infinitesimal motion for a tensegrity are given by;

$$\begin{aligned}(\{v_i\} - \{v_j\}) \cdot (\{p_i\} - \{p_j\}) &= 0 && \text{For each bar } (i, j) \\ (\{v_i\} - \{v_j\}) \cdot (\{p_i\} - \{p_j\}) &\geq 0 && \text{for each strut } (i, j) \\ (\{v_i\} - \{v_j\}) \cdot (\{p_i\} - \{p_j\}) &\leq 0 && \text{for each cable } (i, j)\end{aligned} \quad (5.1.1)$$

The following condition for a self-stress is equivalent to the matrix equation (3.1.12).

For each vertex i ,

$$\sum_j w_{ij} (\{p_j\} - \{p_i\}) = 0 \quad (5.1.2)$$

where the sum is taken over all j and $w_{ij} = w_{ji}$ represents the stress in the member connecting nodes i and j .

The principle of “first-order duality” expresses the close connection between self-stresses and infinitesimal rigidity. In mathematical terms the stress equilibrium constraints (5.1.2) are the dual linear program of the infinitesimal motion constraints (5.1.1). The physical interpretation of this is that every first order rigid tensegrity has a strict proper self-stress (Roth and Whiteley, 1981). In other words, any infinitesimally rigid tensegrity has a proper self-stress that is nonzero on every

strut and cable. The converse of this statement is not true, however. A strict proper self stress on each strut and cable only ensures that the members act like bars. For a tensegrity to be infinitesimally rigid, it is also necessary that the truss, obtained by replacing every cable and strut by a bar, is infinitesimally rigid. Hence, the necessary and sufficient condition for first order rigidity is given by the following theorem;

Theorem 5.1:

A tensegrity is infinitesimally rigid if and only if it has a strict proper self-stress and the corresponding truss (obtained by replacing every strut and cable by a bar) is infinitesimally rigid.
(Roth and Whiteley, 1981)

Based on this intuitive notion of rigidity the generalisation to higher order forms of rigidity is fairly straightforward. Provided that a tensegrity has a strict proper self-stress, the particular form of rigidity for the tensegrity is the same as that of the corresponding truss.

5.1.2 *Prestress stability and super stability*

Other important notions of stability such as prestress stability and super stability require more stringent tests which depend on the values of the stresses, the geometric configuration as well as material properties in the case of prestress stability. If a certain configuration of a structure is prestress stable, an energy function may be defined as the sum of the energies of all the members, and that function has a local minimum at the given configuration. A necessary condition for prestress stability is that the tangent stiffness matrix is positive semi-definite (Connelly and Whiteley, 1996). Super stability is a stronger form of stability which implies that the structure is both prestress stable and globally rigid, in the sense that there is no other configuration of the structure that does not violate distance constraints (Connelly, 1999).

According to Connelly, when a structure is super stable, increasing the prestress "stiffens" it; whereas if a structure is only prestress stable, increasing the prestress could lead to catastrophic failure. Therefore, the stability of super stable structures would appear to be independent of material properties, as can be verified from Connelly's definition of super stability (Connelly, 1999) which depends only on the stress matrix, Ω and affine motions. Based on Connelly's work, Ohsaki and Zhang investigated the stability conditions for prestressed pin-jointed structures and presented a new sufficient condition for stability of a kinematically indeterminate tensegrity (Ohsaki and Zang, 2006). In addition, it was found that a statically



indeterminate and kinematically determinate structure is stable only if the prestresses are small enough.

Much theoretical work in the fields of structural mechanics and applied mathematics has shown that a super stable structure is stable irrespective of the level of prestress if the yielding and buckling of members are neglected. Despite this, important counter examples are provided by Guest who explored how the stiffness of two example tensegrity structures changed as the level of prestress in a member varied (Guest, 2011). The example structures were both super stable, in the sense defined by Connelly (1999). The first was based on the classic 'expanded octahedron' tensegrity and was kinematically indeterminate; the second had the same arrangement of struts and cables with sufficient additional cables added to make it kinematically determinate. It was shown that, for high levels of prestress, the originally stable tensegrities could be made to have zero stiffness or indeed be made unstable.

5.1.3 Higher order mechanisms

Kinematically indeterminate reticulated systems admit mechanisms. These may be either finite mechanisms, which extend into finite motions without member deformations, or they may be infinitesimal mechanisms, which allow only infinitesimal displacements without deformations. A statically determinate assembly that is not first order rigid admits only finite mechanisms, and is unstable (Ohsaki and Zhang, 2006). However, a truss that is both statically and kinematically indeterminate can have infinitesimal mechanisms for which first order displacements are associated with second (or higher) order changes of length of the bars. As some energy is absorbed as the load increases, the assembly is said to have first (or higher) order stiffness and is stable. For a kinematically indeterminate tensegrity that has a strict proper self-stress it follows, (by direct analogy to Theorem 5.1,) that the stability characteristics of the tensegrity structure is the same as that of the corresponding truss (obtained by replacing each strut and cable by a bar).

The mechanism order definition is related to size order notions. The Euclidean norm of a vector $\{X\}$ of R^N is defined as

$$\|X\| = \left(\sum_{i=1}^N X_i^2 \right)^{1/2} \quad (5.1.3)$$

System member lengths l_j are considered as finite, and assumed to be of zero order. If ' 0_0 ' is used to denote terms of zero order then we write $l_j = 0_0$, $\forall j$, or

$$\|l\| = O_0 \quad \text{with } \{l\} = \{l_1, \dots, l_j, \dots, l_b\}^t \quad (5.1.4)$$

Higher order terms are defined recursively by the relation,

$$O_r = \xi O_{r-1} = \xi^r O_0, \quad (5.1.5)$$

where O_r means "order r " and ξ is a small positive constant much less than one ($\xi \ll 1$).

It is assumed that external loads create mechanism displacements $\{d^K\}$ of order one and orthogonal displacements $\{d^I\}$ of order greater than or equal to two:

$$\{d\} = \{d^K\} + \{d^I\} \quad \text{with } \|d\| = O_1, \|d^K\| = O_1 \text{ and } \|d^I\| \leq O_2. \quad (5.1.6)$$

The following definition of a higher order mechanism is written according to Koiter.

Definition 5.2 (Koiter, 1984):

"An infinitesimal mechanism is said to be of higher order, if there exists an infinitesimal motion such that no bar undergoes an elongation of lower than the third order"

A more precise definition of the order of a mechanism is based on the formulation submitted by Tarnai (Tarnai, 1984):

Definition 5.3 (Vassart et al. 2000):

"An internal mechanism is called mechanism of order r " ($r \geq 1$) if there exists infinitesimal node displacements (of the first order) such that member length variations are equal to zero until order r , but there does not exist infinitesimal node displacements such that member length variations are equal to zero at order $r + 1$."

5.1.4 Finite mechanisms

A statically determinate reticulate assembly which is also kinematically indeterminate will only possess finite mechanisms and is unstable. Finite mechanisms are characterised by nodal displacements which do not generate member length variations of any order. The identification of finite mechanisms associated with an assembly which is both statically and kinematically indeterminate is more problematic. A possible approach would be to express length variation coefficients $\{e\}$ in terms of the displacements $\{d\}$ and then attempt to solve the system $\{e\} = 0$. However, the system of equations, $\{e\} = 0$ reduces to a system of quadratic equations, which can not be solved easily (Vassart et al., 2000). A more practical approach given by Vassart et al. (2000) uses an iterative algorithm to search for the mechanism order value and by

introducing a stop criterion can detect finite mechanisms for most constructive reticulated systems. The disadvantage of this method is that it is inefficient and computationally expensive.

A more direct method for identifying finite mechanisms which applies to symmetric structures has been proposed by Kangwai and Guest (1999). Using group representation theory and symmetry arguments, it is possible to show that particular mechanisms of a symmetric structure must be finite. Unfortunately, it is not always possible to identify all finite mechanisms of a symmetric structure by this method.

5.2 Analysis of internal mechanisms for kinematically and statically indeterminate reticulated systems

A vector basis for the internal mechanisms of a reticulated system may be obtained from analysis of the equilibrium matrix of the system in its original configuration, as described in Chapter 3. However, the precise nature of the inextensional mechanisms can only be determined from analysis of the equilibrium matrix of the system in its reference configuration. Here, reference configuration is associated with the non loaded, but self-stressed geometry. Pellegrino and Calladine (1986) developed a simple algorithm to detect the presence of first-order stiffness in the self-stressed assembly and were able to answer some fundamental questions regarding the stiffening effects of self-stress in indeterminate structures. This method relies on the evaluation of so called product force vectors, associated with the inextensional mechanisms of a prestressable assembly (Pellegrino and Calladine (1986); (1984)). A more general method, suitable for analysis of internal mechanisms of any order has been developed by Vassart et al. (2000). In this method, the equilibrium equations with respect to the reference configuration are used explicitly.

A relatively simple analytic matrix method for determining the order of any mechanism of a reticulated system has been proposed by Vassart, Laporte and Motro (Vassart et al. 2000). This method enables most of the kinematically indeterminate and relatively complex systems to be processed with minimal computational effort. The order of a given mechanism as well as analytic expressions for mechanism trajectories are obtained through an iterative process, where at each step member length variations are evaluated at a higher order until the mechanism order is found. The algorithm is based on geometric arguments and structural mechanics principles and is derived using asymptotic methods and basic results from linear algebra.

5.2.1 Geometrical characterisation algorithm for mechanism order analysis

Following the formulation presented by Vassart et al. (2000), the equilibrium matrix $[A]$ is defined for a reticulate system in its reference configuration. Similarly, the vector of node displacements $\{d\}$, and the vector $\{e\}$ of length variation coefficients are both evaluated with respect to the reference configuration.

The geometrical characterisation of a higher order mechanism may be stated as follows:

Definition 5.4 (Vassart et al., 2000):

“A reticulated system admits a higher order mechanism, if, and only if, there exists in the vicinity of a mechanism $\{d^K\}$ (not equal to zero), a displacement $\{d^l\}$ ($\in \text{Im } A$) such as length variation coefficients $\{e\}$ are equal to zero until order two”

This is merely a restatement of Definition 5.2, however, by writing the geometric relationship between length variation coefficients $\{e\}$ and the displacement components $\{d^K\}$ and $\{d^l\}$ as a matrix equation and expanding both sides of this equation in an asymptotic series it can be shown that the condition for a higher order mechanism (Def. 5.4) is equivalent to the following vector-matrix expression. (Vassart et al., 2000)

$$\exists(\{d^K\}, \{d^l\}) \in (\text{Ker } A^t - \{0\} \times \text{Im } A) \text{ such as } \{e^{(2)}\} = [A]^t \{d^l\} + \frac{1}{2} [\Delta A_{d^K}]^t \{d^K\} = 0 \quad (5.2.1)$$

where $[\Delta A_{d^K}]$ is the matrix difference between the equilibrium matrix $[A^{\text{def}}(d^K)]$, in its deformed state under $\{d^K\}$, and the equilibrium matrix $[A]$ in its reference state:

$$[\Delta A_{d^K}] = [A^{\text{def}}(d^K)] - [A] \quad (5.2.2)$$

Terms of $[\Delta A_{d^K}]$ are simply obtained by replacing coordinates x_i in matrix $[A]$ by corresponding displacements d_{ix}^K .

The asymptotic expansion of a vector X may be written as

$$X = \sum_{\substack{a \geq a_0 \\ a \geq a_0}} X^{(a)} \text{ with } \|X^{(a)}\| = O_a \text{ or } X^{(a)} = 0, = 0 \quad (5.2.3)$$

where $X^{(a)}$ denotes the “a” order value of X .

Since $\{e^{(2)}\}$ represents the O_2 value of the vector $\{e\}$ and the term $[A]^t \{d^l\}$ is the same order as vector $\{d^l\}$, for the first equality in Eq. (5.2.1) to hold, the displacements $\{d^l\}$ must also be O_2 . Similarly, the mechanism vector $\{d^K\}$ is defined only at first order. Hence, Eq. (5.2.1) may be written with the order values indicated as,

$$\exists(\{d^{K(1)}\}, \{d^{I(2)}\}) \in (\text{Ker } A^t - \{0\} \times \text{Im } A)$$

$$\text{such as } \{e^{(2)}\} = [A]^t \{d^{I(2)}\} + \frac{1}{2} [\Delta A_{d^{K(1)}}]^t \{d^{K(1)}\} = \{0\} \quad (5.2.4)$$

where $\{d^{K(1)}\}$ is the first order main part of $\{d^K\}$ and $\{d^{I(2)}\}$ is the second order main part of $\{d^I\}$. If the system of equations $\{e^{(2)}\} = \{0\}$ has no solution in $\{d^{K(1)}\}$ and $\{d^{I(2)}\}$, except the trivial solution, then the reticulated system admits only first order mechanisms. Conversely, there exists at least one higher order mechanism, since length variation coefficients $\{e^{(2)}\}$, due to the displacement $\{d^{K(1)}\}$, are cancelled at order two by at least one displacement $\{d^{I(2)}\}$.

The system of equations is linear with respect to $\{d^{I(2)}\}$ components, but is quadratic with respect to those of $\{d^{K(1)}\}$. In order to obtain linear equations with independent variables, the displacement vectors are written as linear combinations of the basis vectors of their respective vector subspaces. Thus, mechanism $\{d^{K(1)}\}$ is defined as a linear combination of vectors $\{d^{K1}\}, \dots, \{d^{K\rho}\}, \dots, \{d^{Km}\}$, which constitute a basis of the vector subspace $\text{Ker } A^t$:

$$\{d^K\} = \sum_{\rho=1}^m \mu_\rho \{d^{K\rho}\} \quad (5.2.5)$$

with $\|d^{K\rho}\| = O_0$ and $|\mu_\rho| \leq O_1$.

The vector comprising all m independent variables μ_ρ is noted as $\{\mu\}$:

$$\{\mu\} = \{\mu_1, \dots, \mu_\rho, \dots, \mu_m\}^t \quad (5.2.6)$$

Similarly, the displacement vector $\{d^I\}$ is expressed as a linear combination of the basis $\{d^{I1}\}, \dots, \{d^{I\rho}\}, \dots, \{d^{Im}\}$ of the vector space $\text{Im } A$ as:

$$\{d^I\} = \sum_{p=1}^{r_A} u_p \{d^{Ip}\} \quad (5.2.7)$$

with $\|d^{Ip}\| = O_0$, $|u_p| \leq O_2$ and $\{u\} = \{u_1, \dots, u_p, \dots, u_{r_A}\}^t \quad (5.2.8)$

Hence, the displacement components $\{d^{K(1)}\}$ and $\{d^{I(2)}\}$ may be expressed as:

$$\{d^{K(1)}\} = \sum_{\rho=1}^m \mu_\rho^{(1)} \{d^{K\rho}\} \quad (5.2.9)$$

$$\{d^{I(2)}\} = \sum_{p=1}^{r_A} u_p^{(2)} \{d^{Ip}\} \quad (5.2.10)$$

Substituting in Eq. (5.2.4) a system of linear equations is obtained with b equations and $m + r_A = N$ unknowns, $\{\mu^{(1)}\}$ and $\{u^{(2)}\}$. If this system has no solution, the considered mechanism is

first order. In the case of at least a solution $(\{\mu^{(1)}\}, \{u^{(2)}\})$, solution vectors $(\{d^{K(1)}\}, \{d^{I(2)}\})$ may be determined. Having determined that mechanisms $\{d^K\}$ are of higher order, further iterations of the algorithm are performed in order to determine the precise order of the mechanisms and at each step higher order terms of the solution vectors are obtained as a solution to a linear system of equations (if it exists).

In general, after step $r - 1$, displacements $(\{d^{K^*}\}, \{d^{I^*}\})$ are known, which cancel length variations until order r , where

$$\{d^{K^*}\} = \sum_{a=1}^{r-1} \{d^{K(a)}\}, \quad \{d^{I^*}\} = \sum_{a=2}^r \{d^{I(a)}\}, \quad (5.2.11)$$

with $\{d^{K(a)}\} \in \text{Ker } A^t$ and $\{d^{I(a)}\} \in \text{Im } A$.

The objective of step r in the algorithm is to determine if there exists displacements $(\{D^K\}, \{D^I\})$, which cancel length variations at order $r + 1$, where

$$\{D^K\} = \sum_{\rho=1}^m \bar{\mu}_\rho \{d^{K\rho}\} \quad \text{and } \|D^K\| = O_r \text{ (or } D^K = 0) \quad (5.2.12)$$

$$\{D^I\} = \sum_{p=1}^{r_A} U_p \{d^{I\rho}\} \quad \text{and } \|D^I\| = O_{r+1} \text{ (or } D^I = 0) \quad (5.2.13)$$

If the system $\{e^{(r+1)}\} = 0$ of b equations in N unknowns, has at least a solution $(\{\bar{\mu}_\rho\}, \{U_p\})$, the new solution vectors are expressed as,

$$\{d^K\} = \{d^{K^*}\} + \{D^K\} \quad (5.2.14)$$

$$\{d^I\} = \{d^{I^*}\} + \{D^I\} \quad (5.2.15)$$

The matrix formulations for calculation of vector $\{e^{(r+1)}\}$ will depend on the value of r and contain terms involving the displacement components computed at previous steps of the algorithm. In general, for odd values of r ($r = 2\eta - 1$), the vector $\{e^{(r+1)}\}$ is obtained as a summation of $2r$ terms, given by;

$$\begin{aligned} \{e^{(r+1)}\} = & [A]^t \{D^I\} + [\Delta A_{d^{K(a)}}]^t \{D^K\} + \sum_{i=2}^{\eta-1} \left\{ [\Delta A_{d^{K(i)}}]^t \{d^{K(2\eta-i)}\} + [\Delta A_{d^{I(i)}}]^t \{d^{I(2\eta-i)}\} \right\} + \\ & \frac{1}{2} [\Delta A_{d^{K(\eta)}}]^t \{d^{K(\eta)}\} + \frac{1}{2} [\Delta A_{d^{I(\eta)}}]^t \{d^{I(\eta)}\} + \sum_{j=1}^{2\eta-2} \left\{ [\Delta A_{d^{K(j)}}]^t \{d^{I(2\eta-j)}\} \right\} \end{aligned} \quad (5.2.16)$$

For even values of r ($r = 2\eta$), the vector $\{e^{(r+1)}\}$ is given as a summation of $2r - 1$ terms;

$$\begin{aligned} \{e^{(r+1)}\} = & [A]^t \{D^I\} + [\Delta A_{d^{K(a)}}]^t \{D^K\} + \sum_{i=2}^{\eta} \left\{ [\Delta A_{d^{K(i)}}]^t \{d^{K(2\eta+1-i)}\} + [\Delta A_{d^{I(i)}}]^t \{d^{I(2\eta+1-i)}\} \right\} + \\ & \sum_{j=1}^{2\eta-1} \left\{ [\Delta A_{d^{K(j)}}]^t \{d^{I(2\eta+1-j)}\} \right\} \end{aligned} \quad (5.2.17)$$

These general expressions for evaluating length variation coefficients at order $r + 1$ may be derived from the asymptotic expansion for the exact expression for $\{e\}$ in terms of the $\{d^l\}$ and $\{d^k\}$. A more detailed formulation of the geometric characterisation algorithm and its application to simple reticulated systems is given by Vassart et al. (2000).

5.3 Prestress design and optimisation

5.3.1 *Theory of prestress design for tensegrity structures*

The purpose of prestressing a cabled structure is to increase its stiffness, thereby increasing the stiffness to weight ratio of the structure. This approach to prestress design is particularly important for stiffness dominated structures such as large span geodesic, tensegrity domes. In this case, the dome should be so designed, that prestressing increases the resistance to non-linear buckling. The criteria used to determine the level of prestress in a tensegrity structure depends on the nature of the structure in question and anticipated service loads. For kinematically indeterminate structures such as Geiger cable domes, the level of prestress will not only affect the geometric configuration, but also determine the load bearing capacity (Yuan and Dong, 2003). Kinematically determinate tensegrities will generally have a higher load bearing capacity and inherent stiffness in the absence of prestress forces, however, in this case it may be desirable to introduce sufficient prestress into the structure in order to resist non-linear buckling phenomenon.

For tensegrity structures which are initially quite flexible in the absence of prestressing it may be necessary to consider the influence of the prestressing on the dynamic response of the structure. A structure is said to be "mass-dominated," or "flexible," if the excitation frequencies due to dynamic loads are much higher than the natural frequencies of the structure that are easily excitable. On the other hand, a structure is "stiffness dominated," or "rigid," if the lowest natural frequencies of the structure are much higher than the excitation frequency. In between these two extremes there exists a condition of resonance in which the frequency of an excitation force equals the natural frequency. In this case very large vibrations build up, even if the excitation force is relatively low – especially if the force is applied near a point of maximum vibration in the natural frequencies mode shape and the level of damping is small. By increasing the level of prestress in a structure that is initially flexible, in the dynamical sense, the structure is brought closer to a condition of resonance. It is therefore necessary to consider the dynamic amplification factor when designing the optimal prestress for such structures. In the case where the structure is initially stiffness dominated, the prestressing will only reduce the

dynamic response of the structure and therefore, the dynamic response of the structure does not have to be considered in the design of optimal prestress. The inherent rigidity of kinematically determinate tensegrities suggests that these structures may be more suitable for practical applications involving static structures due to the lower level of optimal prestress and favourable dynamical characteristics.

5.3.2 *The integral feasible prestress optimisation algorithm*

The integral feasible prestress algorithm developed by Yuan and Dong (2003) was intended for the analysis of cable domes with a high degree of symmetry. By exploiting the symmetry of the structure, the number of independent self-stress modes could be reduced significantly. The integral feasible prestress state was then obtained as a solution to a multivariable least squares problem. Finally, by introducing the parameter of prestress level γ , the problem of optimal prestress design could be solved as a single variable optimisation problem.

The basic algorithm is described as follows:

By using the SVD of the equilibrium matrix (or otherwise), the basis vectors for the s independent states of self-stress are given by $\{w_1^N\}, \{w_2^N\}, \dots, \{w_i^N\}, \dots, \{w_s^N\}$, where $\{w_i^N\}$ denotes the i^{th} column of $[W^N]$ (see (3.1.7)).

A feasible prestress may be expressed as a linear combination of the w_i^N :

$$\begin{aligned} \{X\} &= \{w_1^N\}\alpha_1 + \{w_2^N\}\alpha_2 + \dots + \{w_s^N\}\alpha_s \\ &= [W^N]\{\alpha\}^t \end{aligned} \quad (5.3.1)$$

where $\{X\}$ is the unknown integral feasible prestress.

In order to preserve the symmetry of the structure in static equilibrium it is necessary to ensure that any group of members symmetric to one another through rotations and/or reflections about the symmetry axis of the structure, carry the same prestress forces. If there are τ groups of such members within a structure the integral feasible prestress for the entire structure can be expressed as

$$\{X\}_{b \times 1} = \{x_1, x_1, x_1, \dots, x_i, x_i, x_i, \dots, x_\tau, \dots, x_\tau\}^t$$

$$\begin{aligned}
&= \begin{bmatrix} 1 & 0 & 0 & 0 & 0 \\ 1 & \vdots & 0 & 0 & 0 \\ \vdots & 1 & \vdots & 0 & 0 \\ \vdots & 1 & 1 & \vdots & 0 \\ 0 & \vdots & 1 & 1 & \vdots \\ 0 & 0 & \vdots & 1 & 1 \\ 0 & 0 & 0 & \vdots & \vdots \\ 0 & 0 & 0 & 0 & 0 \end{bmatrix}_{b \times \tau} \begin{Bmatrix} x_1 \\ \vdots \\ x_i \\ \vdots \\ x_\tau \end{Bmatrix}_{\tau \times 1} \\
&= [\{\varepsilon_1\} \dots \{\varepsilon_i\} \dots \{\varepsilon_\tau\}] \begin{Bmatrix} x_1 \\ \vdots \\ x_i \\ \vdots \\ x_\tau \end{Bmatrix} \tag{5.3.2}
\end{aligned}$$

where ε_i is the base vector of members' internal force composed of unit stress in the i^{th} group and zero in the other $(\tau - 1)$ groups.

Substituting Eq. (5.3.2) into (5.3.1) for $\{X\}$ and letting $\alpha_1 = 1$ for simplicity, the following form of Eq. (5.3.1) is obtained;

$$\{w_2^N\}\alpha_2 + \dots + \{w_s^N\}\alpha_s - \{X\} = -\{w_1^N\}$$

or in matrix form

$$[\tilde{T}]\{\tilde{\alpha}\} = -\{w_1^N\} \tag{5.3.3}$$

where $[\tilde{T}]$ is the $b \times (s - 1 + \tau)$ matrix and can be denoted as $[\tilde{T}] = [\{w_2^N\}, \dots, \{w_i^N\}, \dots, \{w_s^N\}, -\{\varepsilon_1\}, -\{\varepsilon_2\}, \dots, -\{\varepsilon_\tau\}]$,

$\{\tilde{\alpha}\}$ is the unknown column vector, written as $\{\tilde{\alpha}\} = \{\alpha_2, \alpha_3, \dots, \alpha_s, x_1, x_2, \dots, x_\tau\}^t$

The least squares method by Householder transformations may be used to solve Eq. (5.3.3).

Assuming the columns of $[\tilde{T}]$ are linearly independent, the unique solution of the least squares problem can be obtained.

Once $\{\tilde{\alpha}\}$ is known, the unit integral feasible prestress $\{X\}$ is given by Eq. (5.3.2). Hence, the prestress of the dome can be expressed as

$$[T] = [X]\gamma \tag{5.3.4}$$

where $[T]$ is the integral feasible prestress and γ is defined as the parameter of prestress level.

The optimal prestress level γ could be found by a one dimensional searching method. It was assumed that if a cable became slack under a certain prestress level and range of external loads, the design of the dome had failed and the next iteration of the algorithm was performed

using a higher level of prestress. In addition there was a constraint on the nodal displacements and a lower bound for the strut stress in order to take account of the Euler buckling load. The aim of the optimisation problem was to find the minimum level of prestress that satisfied the member stress constraints.

5.3.3

Discussion and further applications

A potential problem with this algorithm is that it is assumed that the vector subspace of admissible prestress is one dimensional, i.e. that the integral feasible prestress is uniquely defined by a single parameter γ . In fact the complete set of unit integral feasible prestress vectors can be obtained more directly from the analysis of a symmetric structure using the symmetry adapted equilibrium matrix (Kangwai and Guest, 2000). The symmetry adapted equilibrium matrix is represented in block-diagonal form and the unit integral feasible prestress vectors are obtained as a basis for the nullspace of the equilibrium submatrix block corresponding to the first irreducible matrix representation $\Gamma^{(A_1)}$. Since the bar-force vector symmetry subspace $\mathbb{V}_f^{(A_1)}$, has the full symmetry properties of the structure, the self-stress modes present in this symmetry subspace also have the full symmetry properties of the structure (Kangwai and Guest, 2000).

For optimal prestress design of large span braced domes it would usually be required to consider the full non-linear response of the structure under various loading conditions. In this case, finding the optimal prestress level would be more computationally expensive. A basic non-linear analysis would involve an iteration of linear deflection analysis where at each step loads are applied to the structure in its displaced configuration in order to calculate deflections for the next configuration etc. A general matrix method for the analysis of a prestressed mechanisms and frameworks, subject to a general loading and taking account of the stiffening effect of prestressing (at first order) is presented by Pellegrino (Pellegrino, 1990).

5.4 References

Connelly, R. and Whiteley, W. (1996). Second-order rigidity and prestress stability for tensegrity frameworks. *SIAM J. Discrete Math*, 9(3), pp. 453-491.

Connelly, R. (1999). Tensegrity structures: why are they stable? *Rigidity Theory and Applications* [ed. Thorpe, M.F. and Dexbury, P.M.] , pp.47-54. Kluwer Academic/Plenum Publishers: Dordrecht, NY.

- Demain, E.D. and O'Rourke, J. (2007). Rigid Frameworks. In: Geometric Folding Algorithms, pp. 43-58. Cambridge: Cam. Univ. Press
- Guest, S.D. (2011). The stiffness of tensegrity structures. *IMA J. App. Math.* 76, pp. 57-66.
- Kangwai, R.D. and Guest, S.D. (1999). Detection of finite mechanisms in symmetric structures. *Int. J. Solids Structures*, 36, pp. 5507-5527.
- Kangwai, R.D. and Guest, S.D. (2000). Symmetry-adapted equilibrium matrices. *Int. J. Solids Structures*, 37, pp. 1525-1548.
- Koiter, W.T. (1984). On Tarnai's conjecture with reference to both statically and kinematically indeterminate structures. *Lab. Eng. Mechanics*, Report No. 788. Delft, Netherlands.
- Ohsaki, M. and Zhang J. (2006). Stability conditions of prestressed pin-jointed structures. *Int. J. Non-Linear Mechanics*, 41, pp. 1109-1117.
- Pellegrino, S. and Calladine, C.R. (1986) Matrix analysis of statically and kinematically indeterminate frameworks. *Int. J. Solids Structures*, 22(4), pp. 409-428.
- Pellegrino, S. (1990). Analysis of Prestressed Mechanisms. *Int. J. Solids Structures*, 26(12), pp. 1329-1350.
- Pellegrino, S. (1993). Structural computations with the singular value decomposition of the equilibrium matrix. *Int. J. Solids Structures*, 30(21), pp. 3025-3035.
- Roth, B. and Whiteley, W. (1981). Tensegrity frameworks. *Tran. Amer. Math. Soc.*, 265, pp. 419-446
- Tarnai, T. (1984). Comments on Koiter's classification of infinitesimal mechanisms. *Hung. Inst. Build. Sci.*, Budapest.
- Vassart, N., Laporte, R. and Motro, R. (2000). Determination of mechanism's order for kinematically and statically indetermined systems. *Int. J. Solids Structures*, 37, pp. 3807-3839.
- Vilnay, O. (1990). Cable nets and tensegric shells: analysis and design applications. *Ellis Horwood series in civil engineering*, Ellis Horwood Ltd., UK.
- Yuan, X.F. and Dong, S.L. (2003). Integral feasible prestress of cable domes. *Computers Structures*, 81, pp. 2111-2119.

6.1 Design of 3-dimensional tensegrity modules

6.1.1 *The tensegrity prism*

The tensegrity prism or “*T-prism*,” is illustrated in Figure 6.1. It is the simplest 3-dimensional tensegrity structure and is an example of a reticulate assembly that is both statically and kinematically indeterminate of degree 1. A particular feature of this type of structure is that the static and kinematic properties depend on the geometric configuration and relative lengths of struts and cables (Tarnai, 1980; Pellegrino and Calladine, 1986). For example, if we assume the struts are of equal length, the side tendons are of equal length and we allow the length ratio between these two structural elements to vary, while keeping the sum of their lengths constant, it can be shown that there is a unique geometric configuration for which the structure is both rigid and can be in a state of self-stress. This geometric configuration is represented in Fig. 6.1 for a left-handed screwed T-prism. Similarly, a right-handed screwed T-prism corresponds to the mirror image of this representation. The particular configuration of the T-prism results in a structure that is both kinematically and statically indeterminate and the single internal mechanism of the assembly is an infinitesimal mechanism (Tarnai, 1980). It is well known that the T-prism is a super-stable tensegrity and can be stiffened by prestressing (Connelly, 2009).

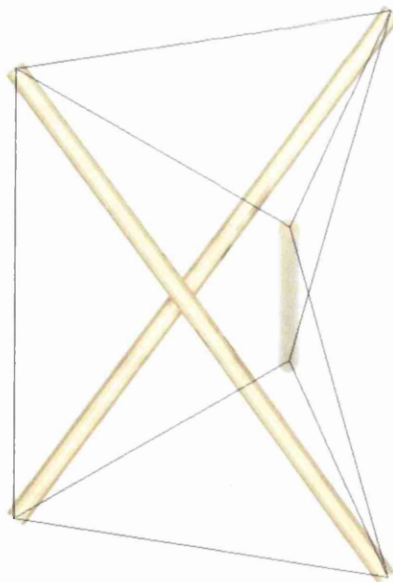


Figure 6.1: Tensegrity Prism

A simple “*form-finding*” method is presented by Burkhardt (2008) for finding the exact geometry of a T-prism when two parameters of the geometry, including the strut length and radius of the prism’s triangular ends have been preset. The problem reduces to a single parameter optimisation problem, in which the objective is to minimise side tendon lengths, subject to the preset geometrical constraints and symmetry constraints. The alternative approach is to fix the tendon lengths and then maximise strut lengths, subject to the symmetry constraints. The problem is formulated as follows, where the second approach is used.

It is convenient to represent the geometry of the T-prism in cylindrical polar coordinates as illustrated in Fig. 6.2. The origin is at the centre of the triangular base of the prism and the polar angle is measured anti-clockwise from the positive x -axis which passes through node A. The z -axis is coincident with the axis of symmetry and is equidistant from the 6 vertices of the t-prism. The nodal coordinates of the T-prism are represented algebraically in Table 6.1, where $\theta_{A'}$ denotes the polar coordinate of node A', ρ is the radial coordinate of the external nodes of the t-prism and h is the height of the T-prism.

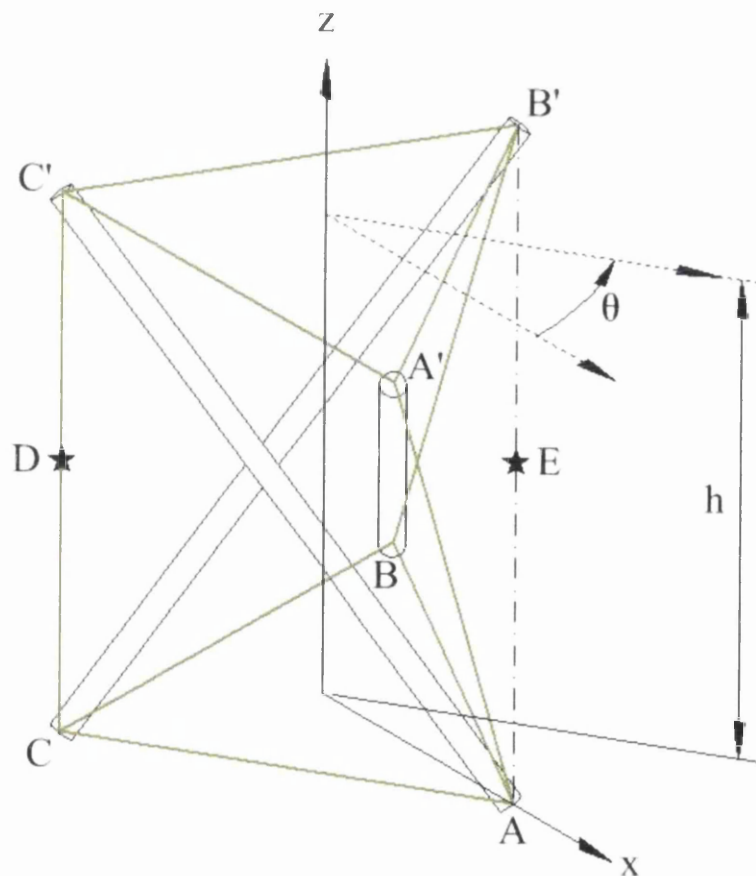


Figure 6.2: T-Prism: Cylindrical Polar Coordinates

The optimisation problem may be stated as follows:

Using the variables h and $\theta_{A'}$, maximise strut length $\mathfrak{S} = |\overline{AC'}|$ while maintaining the following constraints:

- Fixed triangle radius ρ
- Fixed side tendon length $\mathfrak{X} = |\overline{AA'}|$
- Strut symmetry constraints: $|\overline{AC'}| = |\overline{CB'}| = |\overline{BA'}|$
- Side-tendon symmetry constraints: $|\overline{AA'}| = |\overline{BB'}| = |\overline{CC'}|$

Point	Z	Radius	Angle
A	0	ρ	0
B	0	ρ	$2\pi/3$
C	0	ρ	$-2\pi/3$
A'	h	ρ	$\theta_{A'}$
B'	h	ρ	$\theta_{A'} + 2\pi/3$
C'	h	ρ	$\theta_{A'} - 2\pi/3$
D	$h/2$	$\rho \cos(\theta_{A'}/2)$	$\theta_{A'}/2 - 2\pi/3$
E	$h/2$	$\rho \left(\frac{1}{2} \cos(\theta_{A'}/2) - \frac{\sqrt{3}}{2} \sin(\theta_{A'}/2) \right)$	$\frac{\theta_{A'}}{2} + \frac{\pi}{3}$

In order to formulate the problem it is necessary to express the length of members in terms of the nodal coordinates. The length, \mathfrak{D} of a chord between two arbitrary points in space, Q and P , is represented in cylindrical polar coordinates by the following formula;

$$\mathfrak{D}^2 = |\overline{QP}|^2 = (z_Q - z_P)^2 + \rho_Q^2 + \rho_P^2 - 2\rho_Q\rho_P \cos(\theta_Q - \theta_P) \quad (6.1.1)$$

Since the vertices of the t-prism lie on the surface of a cylinder of radius ρ , substituting $\rho_Q = \rho_P = \rho$ in Eq. (6.1.1), the length (squared) of a strut or cable of the t-prism is expressed in the following form;

$$\mathfrak{D}^2 = (\Delta z)^2 + 2\rho^2(1 - \cos(\Delta\theta)) \quad (6.1.2)$$

where Δz denotes the difference in z -coordinate and $\Delta\theta$, the difference in θ -coordinate between the two ends of the member of length \mathfrak{D} .

Applying Eq. (6.1.2), the form-finding problem may be expressed as follows;

$$\underset{\theta_{A'}, h}{\text{maximise}} \quad \mathfrak{S}^2 = |\overline{AC'}|^2 = h^2 + 2\rho^2 - 2\rho^2 \cos\left(\frac{2\pi}{3} - \theta_{A'}\right) \quad (6.1.3)$$

$$\text{subject to} \quad \mathfrak{X}^2 = |\overline{AA'}|^2 = h^2 + 2\rho^2 - 2\rho^2 \cos \theta_{A'} \quad (6.1.4)$$

The problem is then transformed into a single parameter unconstrained optimisation problem by solving Eq. (6.1.4) for $h^2 + 2\rho^2$ and substituting into Eq. (6.1.3). Thus, the equivalent form of the problem is expressed as;

$$\underset{\theta_{A'}}{\text{maximise}} \quad \mathfrak{X}^2 + 2\rho^2 \cos \theta_{A'} - 2\rho^2 \cos\left(\frac{2\pi}{3} - \theta_{A'}\right) \quad (6.1.5)$$

The solution is obtained by setting the first derivative of the objective function (Eq. (6.1.5)) with respect to $\theta_{A'}$ equal to zero, thus;

$$-2\rho^2 \sin \theta_{A'} - 2\rho^2 \sin\left(\frac{2\pi}{3} - \theta_{A'}\right) = 0 \quad (6.1.6)$$

or

$$\sin \theta_{A'} = -\sin\left(\frac{2\pi}{3} - \theta_{A'}\right) = \sin\left(\theta_{A'} - \frac{2\pi}{3}\right) \quad (6.1.7)$$

Since the sine of two angles are equal when their sum is an odd multiple of π , there are two possible solutions of Eq. (6.1.7) for $\theta_{A'}$ in the range $-\pi \leq \theta_{A'} \leq \pi$ given by;

$$\theta_{A'} = \frac{1}{2}\left(\frac{2\pi}{3} \pm \pi\right) \quad (6.1.8)$$

Finally, the solution which corresponds to the maximum value of the objective function is;

$$\theta_{A'} = -\frac{\pi}{6} \quad (6.1.9)$$

The value obtained for $\theta_{A'}$ is substituted into the coordinate expressions in Table 6.1 to obtain the cylindrical polar coordinates of the T-prism, which now depend only on the two parameters ρ and h . We may also define a corresponding right-handed Cartesian coordinate system for the T-prism with the same origin and coordinate axis directions as indicated in Fig. 6.2. The Cartesian nodal coordinates of the t-prism are represented in Table 6.2.

Point	X	Y	Z
A	ρ	0	0
B	$-\frac{1}{2}\rho$	$\frac{\sqrt{3}}{2}\rho$	0
C	$-\frac{1}{2}\rho$	$-\frac{\sqrt{3}}{2}\rho$	0
A'	$\frac{\sqrt{3}}{2}\rho$	$-\frac{1}{2}\rho$	h
B'	0	ρ	h
C'	$-\frac{\sqrt{3}}{2}\rho$	$-\frac{1}{2}\rho$	h
D	$-\frac{(1+\sqrt{3})}{4}\rho$	$-\frac{3}{8}\rho$	$h/2$

6.1.2

Applications of the T-prism in dome design

The T-prism features as an important structural unit in more advanced geodesic tensegrity dome designs. By exploiting the synergy between the X-module and T-prism a range of new tensegrity space trusses have been developed. These specially designed tensegrity modules form the basic building blocks for a wide range of geodesic tensegrity type domes and lead to improvements both in the stability characteristics and overall structural integrity of the dome. 3-dimensional tensegrity modules are required, both in the development of large scale double-layer geodesic tensegrity domes and advanced deployable dome structures. Thus, the range of applications for; and realisable dome structures categorised as; geodesic tensegrity domes are considerably enhanced by introducing 3-dimensional tensegrity modules. A simple example is presented below to illustrate how 3-dimensional tensegrity modules are developed and incorporated in the design process.

First, we consider how to develop a dome structure based on the "*hybrid X-trihex*" lattice introduced in Chapter 2 (see Fig. 6.3). Recall, that the hybrid X-trihex lattice is very similar to the basic X-trihex lattice (Fig. 2.5 and 2.10) used in Chapter 2 to develop a basic dome structure composed of X-modules. In this case it is necessary that the assembly of three smaller X-modules which are shown to meet at nodes 3, 5 and 6 in Figure 6.3 form a rigid sub-structure. One option would be to introduce rigid joints between the struts meeting at nodes 3, 5 and 6. This situation could be improved by replacing the 6 struts of the sub-structure by 3 continuous curved beams that are prestressed by the cable net of the assembly and are lashed or pinned

together at their crossing points. An alternative approach is to transform the assembly of X-modules into a tensegrity space truss. This is achieved by expanding the triangle at the centre of the substructure to form a T-prism and exploiting some type of synergy with the surrounding X-modules to form a rigid, reticulate assembly.

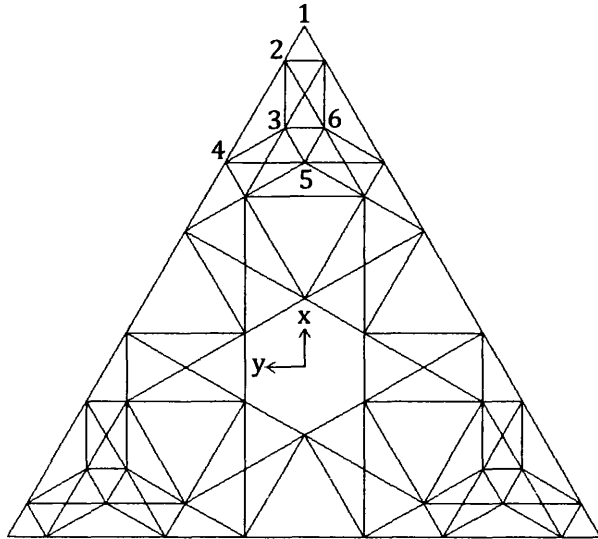


Figure 6.3: Hybrid X-trihex lattice

In its simplest form, the synergy between X-module and T-prism is exemplified in Snelson's assembly of 3 X-modules (Fig. 6.4) which appears in his original patents (Snelson, 1965).

In Figure 6.4, the form of the T-prism can be easily identified at the centre of the assembly, where the struts have now been replaced by the edges of the X-modules. A series of practically useful, rigid tensegrity modules can be derived by introducing additional cables to stabilise the assembly of Fig. 6.4, adjusting strut orientation and geometry, or even modifying the graph structure and introducing additional struts. In all of these structural mutations, as a general rule, the central T-prism will remain unchanged and by modifying the external structure a variety of different ways of incorporating the T-prism in structural design can be realised.

As a first step towards developing practically useful tensegrity space structures we must first consider the "*hybrid tensegrity prism*" illustrated in Figure 6.5. This tensegrity module is derived simply by introducing sufficient additional cables to stabilise Snelson's assembly of X-modules (Fig. 6.4). The synergy between X-modules and T-prism is now clearly apparent. The struts now lie within an annulus bounded by two concentric T-prisms of different radii. Notice also, that there is a phase difference of approx. $\pi/3$ radians in the angular orientation of the two T-prisms (Fig. 6.5) and the inner edge of an X-module replaces a strut of the internal T-prism, whereas the outer edge of an X-module coincides with a cable of the external T-prism. As a result of

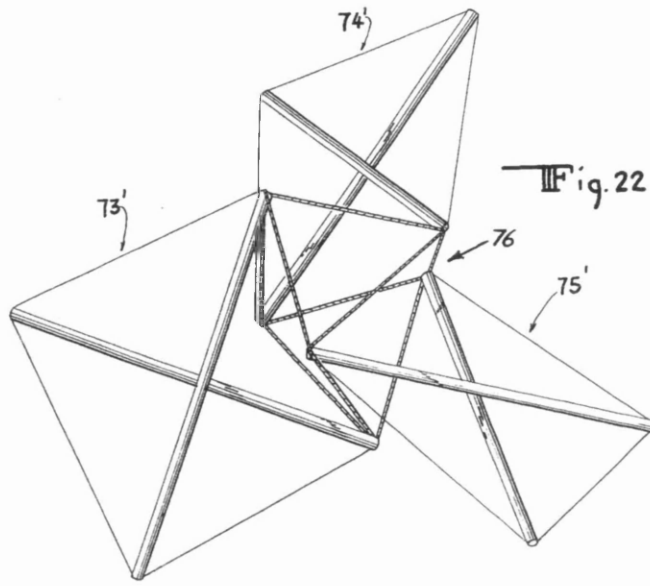


Figure 6.4: Kenneth Snelson, Assembly of 3 X-modules. (Snelson, 1965)

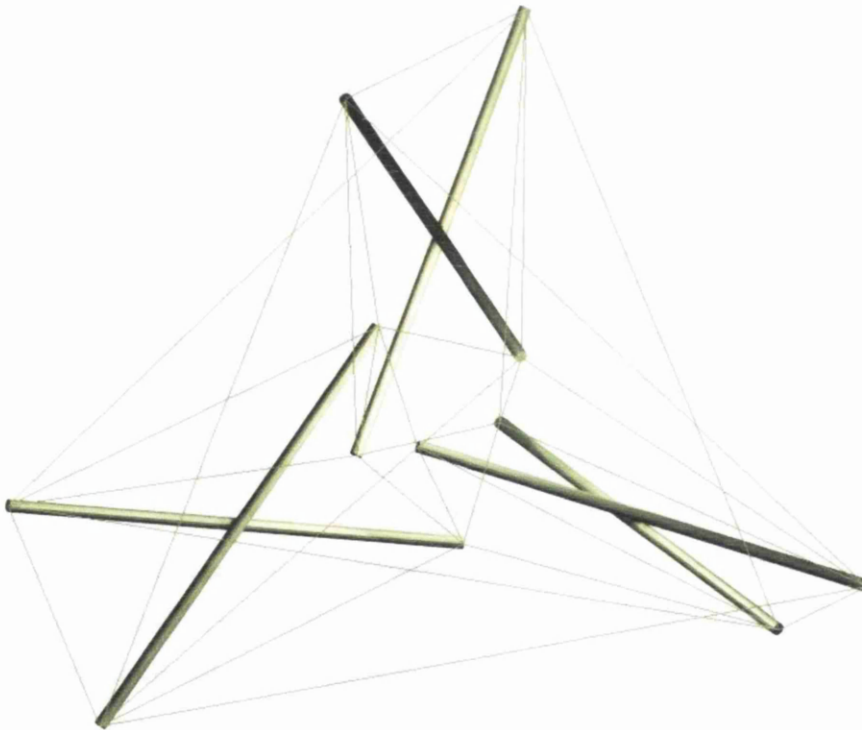


Figure 6.5: Hybrid tensegrity prism

symmetry it can be shown that provided the 3-fold rotational symmetry of the structure is maintained and the internal nodes of the annulus conform to the geometry of a T-prism, the external nodes of the annulus will also coincide with the nodes of a T-prism, regardless of the dimensions of the X-module. Hence, both the internal and external T-prism is in a prestressible configuration and the self-stress states are mutually dependent and integrated throughout the structural assembly.

The hybrid T-prism also has a number of structural advantages compared to the basic T-prism and can be used as a basis for developing more efficient, deployable space structures and domes. From the geometry it can be deduced that the hybrid T-prism is a structure with a relatively low density, i.e. mass per unit of enclosed volume. This is a result of the high proportion of cables to struts and the fact that the relative strut length has been approximately halved. Consequently, for struts with a given slenderness ratio, the volume of a hybrid T-prism will be approx. 8 times that of a basic T-prism which uses the same strut dimensions. It is also apparent that the hybrid T-prism has a favourable strut orientation for resisting side forces and, in fact, the strut orientation can be varied in order to perform an optimisation of the structure over a range of expected loads. Maintaining the symmetry properties of the structure, the geometric parameters involved in the optimisation could include the radius, height and/or orientation angle of the internal and/or external T-prism. When sufficiently prestressed the hybrid T-prism forms a resilient structure with good stiffness in all directions.

What is even more remarkable about this structure is that it is possible to build modular structures for spanning large areas by clustering the hybrid T-prism in 2-dimensions. Although the twist angle of a T-prism does not allow it to form a close packed honeycomb as would a regular triangular prism, the clustering pattern of the hybrid T-prism can easily be deduced from the symmetry and results in a structure consisting of alternating left-handed and right-handed screwed T-prisms interspersed with X-modules. The advantages of this particular clustering pattern and how it relates to the design of geodesic tensegrity domes will be discussed in more detail in section 6.3. In short, the hybrid T-prism is a tensegrity module that may be applied in the design and construction of large span, double-layer, planar or vaulted tensegrity grids and geodesic tensegrity domes. In all these structures the modules are clustered or assembled using the same basic clustering pattern or chart lattice structure. As a whole, these structures are characterised by a high degree of synergy and conform to the purest definition of a tensegrity as employed by Kenneth Snelson.

A simplified version of the hybrid T-prism is illustrated in Figure 6.6. In this alternative version the number of external cables has been reduced by 3 and the X-modules are set in a twisted configuration so that the external nodes lie in a common plane. This tensegrity module is intended for use in deployable dome structures; which deploy as a single structural entity; and adaptive structures. The advantage of this particular structural configuration is that the external cables coincide with the fold lines of the deployable structure. Typically, struts of neighbouring modules are connected by specially designed pin joints which allow a relative rotation of the two modules. A disadvantage of the structure shown in Fig. 6.6 is that, as the X-modules are no longer in the optimum configuration, the T-prism at the centre could collapse by nonlinear snap-through buckling. A simple solution to this problem would be to reintroduce the struts of the central T-prism, which would allow it to be prestressed, independently.

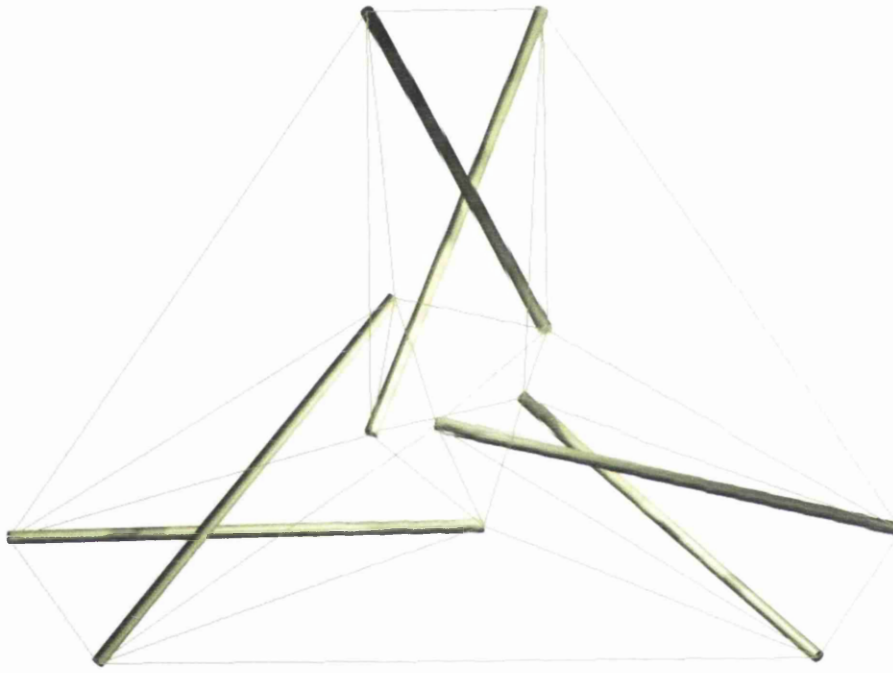


Figure 6.6: Simplified Hybrid T-prism

6.2 Design of a dome honeycomb structure

Next we consider how the T-prism may be integrated in the design of geodesic tensegrity domes and focus on the design of 3-dimensional tensegrity modules which have been developed specifically for applications in the design of geodesic tensegrity domes and dome honeycomb structures. As an example, we illustrate the process of designing tensegrity space trusses for a geodesic tensegrity dome based on the hybrid X-trihex chart lattice structure shown in Fig. 6.3. Furthermore, the design specifications of the dome require that it should have a hexagonal profile and is designed specifically for clustering in 2-dimensions to form a modular, dome honeycomb structure.

The transformation equations for obtaining dome nodal coordinates from chart lattice coordinates are given in Chapter 2, (Eq. (2.2.2) to (2.2.5)). The dome nodal coordinates are computed for nodes 2 to 5 in Fig. 6.3 and the results are shown in Table 6.3. Similarly, the transformations of dome nodal coordinates from a polar coordinate system to a Cartesian coordinate system are given in Chapter 2, (Eq. (2.2.6) to (2.2.8)). The Cartesian coordinates of nodes 2 to 6 in Fig. 6.3 are given in Table 6.4.

Node index i	a_i/r	b_i/r	ρ_i/r	$\tan \theta_i$
2	$\frac{3\sqrt{3}}{5\sqrt{2}}$	$\frac{1}{15\sqrt{2}}$	$\sqrt{\frac{122}{197}}$	$\frac{1}{9\sqrt{3}}$
3	$\frac{7}{5\sqrt{6}}$	$\frac{1}{15\sqrt{2}}$	$\sqrt{\frac{74}{149}}$	$\frac{\sqrt{3}}{21}$
4	$\frac{\sqrt{6}}{5}$	$\frac{2\sqrt{2}}{15}$	$\sqrt{\frac{62}{137}}$	$\frac{2}{3\sqrt{3}}$
5	$\frac{\sqrt{6}}{5}$	0	$\sqrt{\frac{18}{43}}$	0

Node index i	x_i/r	y_i/r	z_i/r
2	$9\sqrt{\frac{3}{394}}$	$\sqrt{\frac{1}{394}}$	$5\sqrt{\frac{3}{197}}$
3	$\sqrt{\frac{147}{298}}$	$\sqrt{\frac{1}{298}}$	$\sqrt{\frac{75}{149}}$
4	$3\sqrt{\frac{6}{137}}$	$2\sqrt{\frac{2}{137}}$	$\sqrt{\frac{75}{137}}$
5	$\sqrt{\frac{18}{43}}$	0	$\sqrt{\frac{25}{43}}$
6	$\sqrt{\frac{147}{298}}$	$-\sqrt{\frac{1}{298}}$	$\sqrt{\frac{75}{149}}$

Observing the chart lattice structure of Fig. 6.3 it can be seen that in order to facilitate dome clustering it would be convenient to allow node 4 (when projected onto the sphere) to lie along the curve of intersection with a neighbouring dome. Since node 4 is closer to the centre of the dome the curves of intersection will be drawn closer to the centre and as a result the dome span would be reduced slightly when compared with the basic X-trihex lattice dome illustrated in Fig. 2.15. As a result of clustering in a hexagonal lattice pattern, three domes will intersect about each foundation node. The dome half-span may be obtained from the geometry using the method introduced in Chapter 2. Thus, the dome half-span is computed from the coordinates of node 4 and is given by;

$$P = x_4 + \frac{1}{2\sqrt{3}}(2y_4) = \frac{22}{\sqrt{822}}r \cong 0.767338r \quad (6.2.1)$$

Notice that the dome half span is less than the x -coordinate of node 2 and so this node must be discarded when developing the final geometry of the dome. A simplified two-dimensional representation of the final dome geometry is illustrated in Figure 6.7.

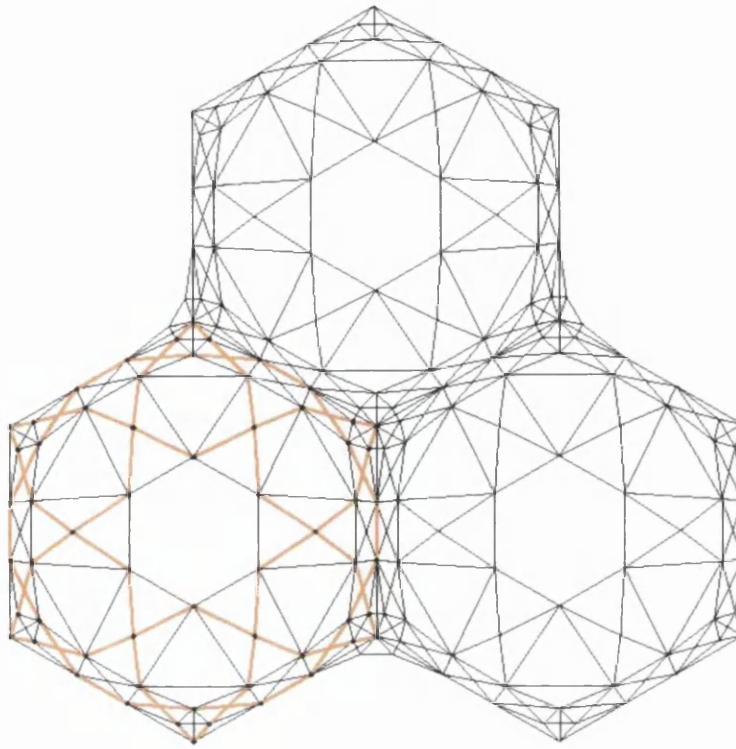


Figure 6.7: Hybrid X-trihex lattice dome clustering

Notice that each dome in Fig. 6.7 has a hexagonal profile and the position of each internal node of the dome is determined purely by the transformations from the chart lattice (Fig. 6.3) onto the circumsphere of the octahedron. The positions of struts, cables and nodes are indicated on the left of the figure and it is clear that, as a reticulate assembly composed of 2-dimensional modules, the dome structure would be highly unstable. This is why it is required to introduce 3-dimensional tensegrity modules in order to develop these designs further.

The process of designing 3-dimensional tensegrity modules for specific regions of a geodesic tensegrity dome will be illustrated using the following example. A substructure of the dome in Fig. 6.7 is highlighted in Fig. 6.8 as the region within the closed, dark polyline. It is intended to transform this substructure into a simple space truss which functions as a rigid, prestressible, tensegrity module. For simplicity, we assume boundary nodes do not change under this transformation, however, additional struts, cables and nodes may be added or subtracted, in the interior of the module, in order to stabilise it. It is found that the integrity and efficiency of the structure can be improved considerably by introducing a so called "*tensegrity joint*," described as follows.

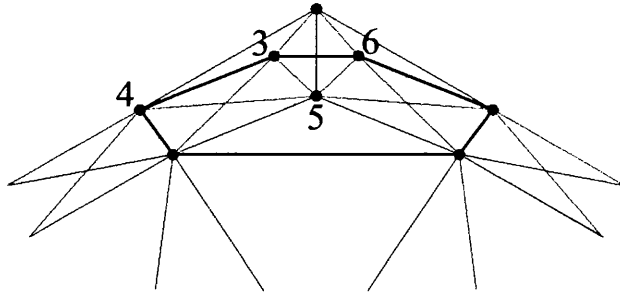


Figure 6.8:
Hybrid X-trihex lattice dome sub-structure

Since the three points 3, 5 and 6 (Fig. 6.8) form the vertices of a triangle in 3-dimensional space, it is evident that a T-prism could be scaled and oriented to fit this region. Observing the diagram of the T-prism given in Fig. 6.2, we assume a geometry for the T-prism can be found such that nodes B', D and A (Fig. 6.2) are coincident with nodes 3, 5 and 6 (Fig. 6.8), respectively, given in Table 6.4. (Note that node D is precisely at the mid-point of the cable connecting nodes C and C' (Fig. 6.2).) Now, it is fairly straight forward to determine a unique solution for the height, h and radius, ρ of the T-prism, given the geometry of the triangle 3-5-6. Since the triangle 3-5-6 is almost equilateral we can expect that the T-prism which fits this geometry will have reasonable dimensions. Exact calculations for the geometry of the T-prism are given below and the visual representations in Fig. 6.1 and 6.2 conform to this geometry.

From Fig. 6.2 and Table 6.1, the following expressions for chord length between the nodes A, D and A, B' of the T-prism are obtained by applying Eq. (6.1.1) and (6.1.2), respectively;

$$\begin{aligned} |\overline{AD}|^2 &= \frac{h^2}{4} + \rho^2 \left(1 + \cos^2 \left(\frac{\theta_{A'}}{2} \right) \right) - 2\rho^2 \cos \left(\frac{\theta_{A'}}{2} \right) \cos \left(\frac{\theta_{A'}}{2} - \frac{2\pi}{3} \right) \\ &= \frac{h^2}{4} + \rho^2 \left(2 + \cos \theta_{A'} - \frac{\sqrt{3}}{2} \sin \theta_{A'} \right) \end{aligned} \quad (6.2.2)$$

$$\begin{aligned} |\overline{AB'}|^2 &= h^2 + 2\rho^2 \left(1 - \cos \left(\theta_{A'} + \frac{2\pi}{3} \right) \right) \\ &= h^2 + \rho^2 (2 + \cos \theta_{A'} + \sqrt{3} \sin \theta_{A'}) \end{aligned} \quad (6.2.3)$$

Solving for ρ^2 and h^2 we obtain;

$$\rho^2 = \frac{\beta - 4\alpha}{3(\sqrt{3} \sin \theta_{A'} - \cos \theta_{A'} - 2)} \quad (6.2.4)$$

$$h^2 = \beta - \rho^2 (2 + \cos \theta_{A'} + \sqrt{3} \sin \theta_{A'}) \quad (6.2.5)$$

where $\alpha = |\overline{AD}|^2$ and $\beta = |\overline{AB'}|^2$.

Applying Eq. (2.2.10) we may express the chord lengths α , β in terms of the Cartesian coordinates of the triangle 3-5-6.

$$\alpha = |\overline{AD}|^2 = 2(r^2 - z_6z_5 - y_6y_5 - x_6x_5) = 2\left(1 - \frac{138}{\sqrt{19221}}\right)r^2 \quad (6.2.6)$$

$$\beta = |\overline{AB'}|^2 = 4y_3^2 = \frac{2}{149}r^2 \quad (6.2.7)$$

where r is the radius of the circumsphere of the dome.

Substituting values for $\theta_{A'}$, α and β from Eq. (6.1.9), (6.2.6) and (6.2.7), respectively into Eq. (6.2.4) and (6.2.5), gives the numerical values for ρ^2 and h^2 as;

$$\rho^2 = \frac{8\left(1 - \frac{138}{\sqrt{19221}}\right) - \frac{2}{149}}{3(\sqrt{3} + 2)}r = 2(2 - \sqrt{3})\left(\frac{595}{447} - \frac{184}{\sqrt{19221}}\right)r \quad (6.2.8)$$

$$h^2 = \left(\frac{2}{149} - 4(2 - \sqrt{3})\left(\frac{595}{447} - \frac{184}{\sqrt{19221}}\right)\right)r \quad (6.2.9)$$

Hence, the radius, ρ and height, h of the T-prism are computed as;

$$\rho \approx 0.0458r \quad (6.2.10)$$

$$h \approx 0.0960r \quad (6.2.11)$$

Since the T-prism does not have any planes of reflection symmetry there is a potential mismatch when the T-prism is introduced to stabilise the sub-structure of Fig. 6.8 which originally has a single plane of reflection symmetry. To preserve the symmetry of the sub-structure the following simple solution is proposed:

A right-handed screwed T-prism may be superimposed onto a left-handed screwed T-prism (Fig.6.9) by reflection of the T-prism of Fig. 6.2 in the plane containing the nodes A, B' and D.

By performing this superimposition of T-prisms a new tensegrity module is derived which is composed of 18 cables and 6 struts which cross each other in pairs. This tensegrity module is called the "Double T-prism," and it is characterised by two orthogonal planes of reflection symmetry. The Double T-prism is illustrated in Figure 6.9, where red struts and cables are used to identify the right-handed screwed T-prism and blue struts and cables identify the left-handed screwed T-prism.

Figure 6.10 illustrates how the Double T-prism may be integrated in the design of the dome sub-structure. A number of simplifications and alternative versions of this design have been proposed. One possibility is illustrated in Fig. 6.11 where the removal of two sets of struts from the interior of the Double T-prism is justified, since the forces in these struts can be resolved by the other structural members of the assembly.

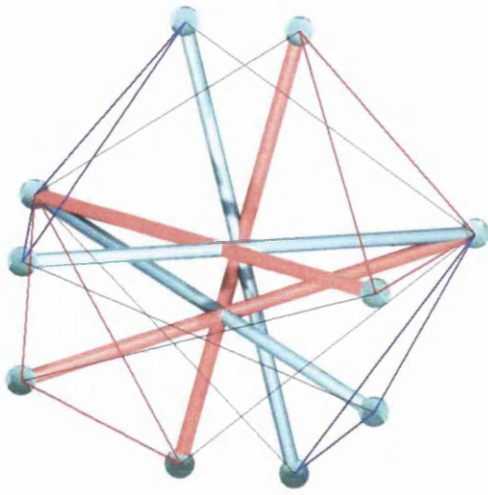


Figure 6.9: Double T-prism

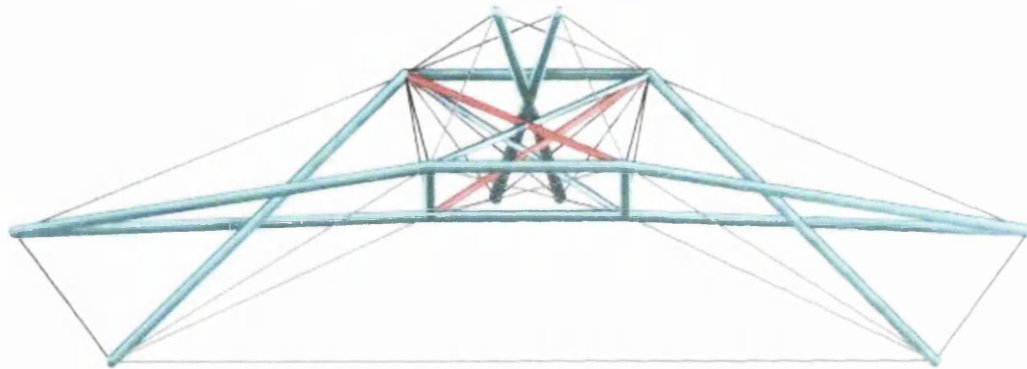


Figure 6.10: Application of the Double T-prism in dome sub-structure design.

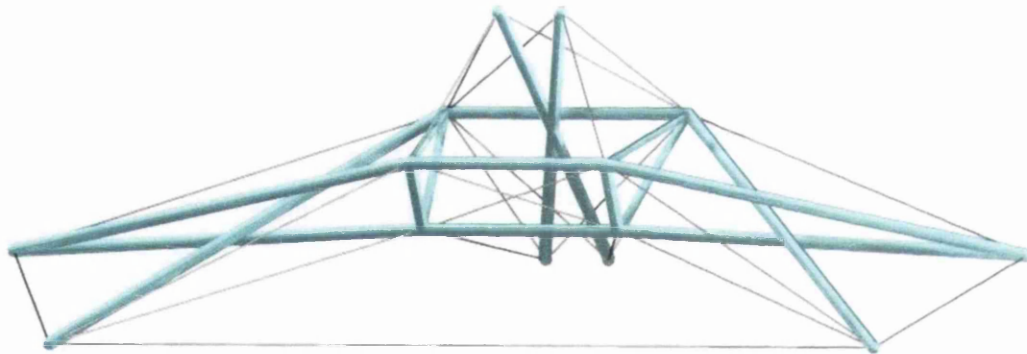


Figure 6.11: Dome sub-structure incorporating a simplified version of the Double T-prism.

In Fig. 6.10 and 6.11, the design intent is that the structure is stiffened by bracing the central X-frame against the cables which support it. There is also a structural advantage to maintaining the full height of the X-frame since it is required to rigidly join this sub-structure to the foundation column of the dome. An alternative version of the tensegrity module of Fig. 6.11 is illustrated in

Fig.6.12, in which it is attached to the foundation column of the dome via a rigid tensegrity truss system.

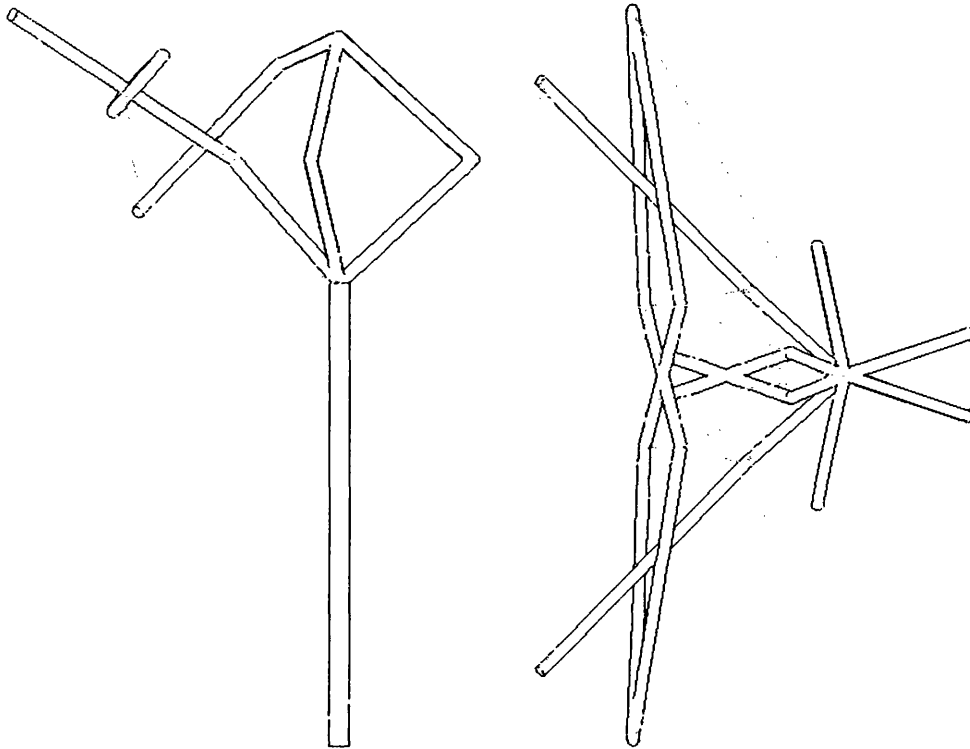


Figure 6.12: Plan and elevation of dome sub-structure attached to foundation

A small modification in the structural arrangement of Fig. 6.12 will be required when it is proposed to unite two or three domes about a particular foundation node to form a cluster of domes. In this case the sub-structure surrounding the foundation column will form a rigid, tetrahedral tensegrity module. As shown in Figure 6.13, the integrity of the structure surrounding the foundation support is substantially improved due to the strength and rigidity of the tetrahedron, which is an important feature of dome honeycomb structures.

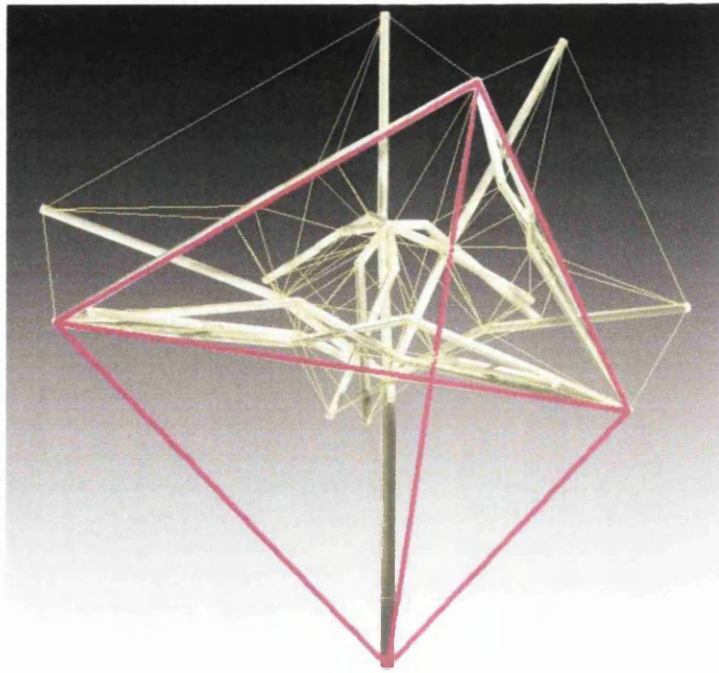


Figure 6.13: Rigid tensegrity tetrahedron provides a strong structural foundation where three domes coalesce within a dome honeycomb structure.

A complete dome structure based on the hybrid X-trihex lattice structure and designed for clustering in 2-dimensions is illustrated in Figure 6.14. It is readily appreciated that incorporating 3-dimensional tensegrity modules has improved the stability characteristics of the dome substantially. In particular, the development of a rigid sub-structure (Fig. 6.12) to attach the dome to the foundation support has improved the structural integrity and rigidity of the structure. The advantage of the hybrid X-trihex lattice pattern is also apparent, since changes in strut orientation between struts meeting at a particular node are less pronounced and the compressive forces are channelled more directly towards the foundation supports.

Several improvements have also been made to the dome superstructure. Shallow octahedral tensegrity modules replace the X-modules used in earlier dome designs and the central hexagon at the top of the dome has been stabilised by bracing the nodes of the hexagon against a central, vertical strut to form a simple tensegrity module. The dome superstructure is stiffened by a network of cables which sequentially connect the internal nodes of structural modules to form a double layer network of cables over the entire surface of the dome.

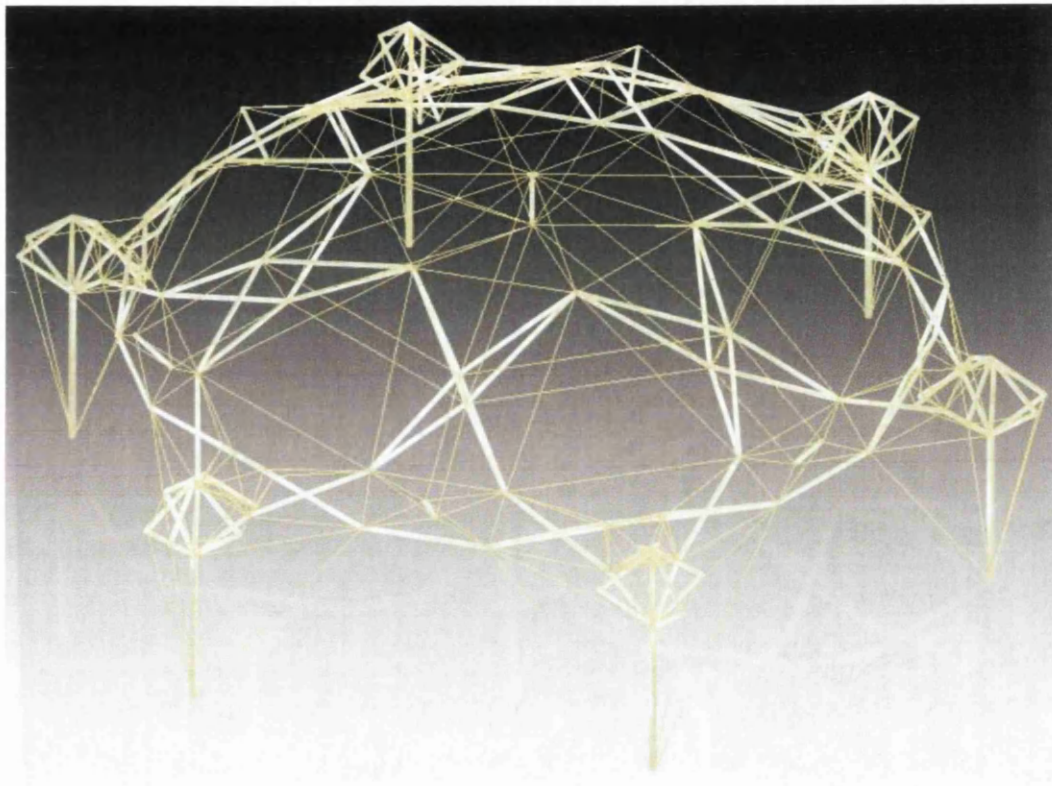
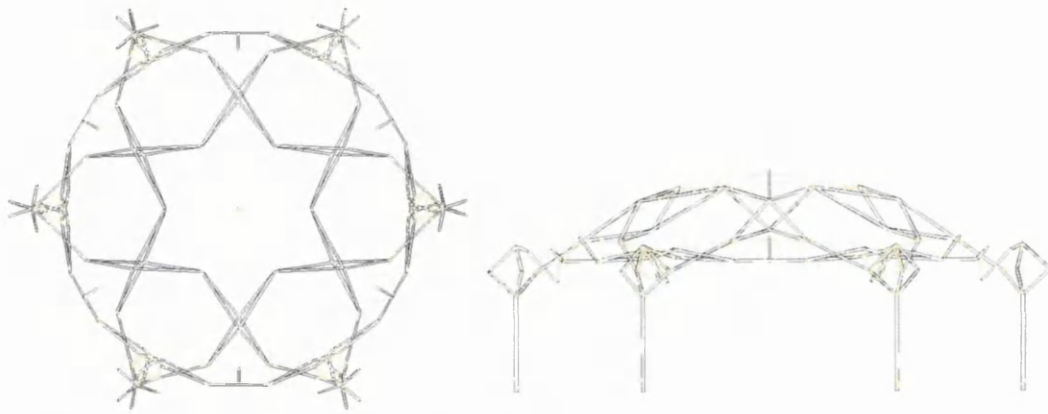


Figure 6.14: Geodesic tensegrity dome design – Plan, elevation and perspective view. A practical dome structure based on the hybrid X-trihex chart lattice.

The dome structure of Fig. 6.14 illustrates well how tensegrity principles may be applied in the design of simple frameworks and skeletal structures, however in order to develop dome structures for specific applications, further refinement and simplification of the design would be performed in parallel with detailed structural analysis and optimisation. Based on strut dimensions it is envisaged that the dome structure represented in Fig. 6.14 could be built with a diameter of between 6 to 12 meters. For a dome with a span of 12m the overall height of the

dome would be approx. 5m and a maximum head height of 3m would be achieved at the dome entrance or where two domes intersect.

A cluster of three domes is illustrated in Fig. 6.15. Within this larger structure, the structural integrity of the dome improves markedly due to the mutual interaction between neighbouring domes and synergy between the dome and tetrahedral unit (Fig. 6.13) at the centre of the cluster. The dome structure of Fig. 6.14 is designed specifically for clustering in a regular pattern and exploits the structural synergy to full advantage while ensuring the process of assembling domes to form a dome honeycomb structure is as simple and effective as possible. The range of applications and versatility of the dome are enhanced due to the structural efficiency and ease with which dome modules can be arranged to cover large areas.

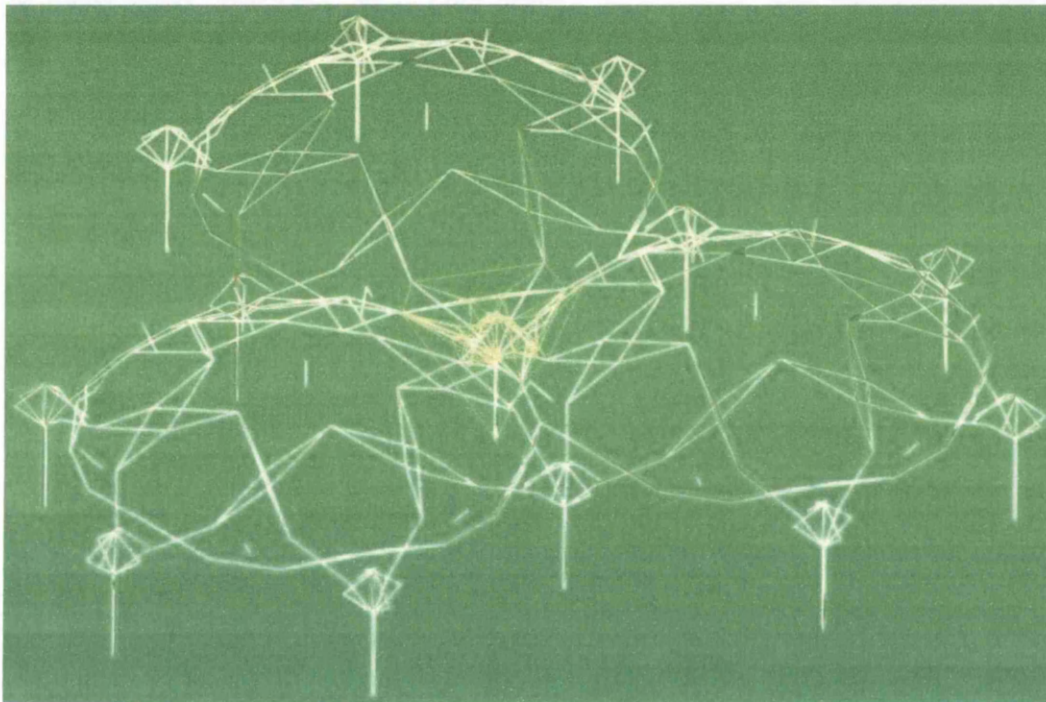


Figure 6.15: Dome honeycomb – cluster of three domes

The modular nature of the dome structure and light weight of structural modules makes it possible to assemble domes relatively quickly using simple, efficient construction techniques. For more specialist applications, where it is required to redeploy a dome or cluster of domes several times over the life cycle of the structure, deployable dome structures could be developed further by exploiting the simple folding mechanisms of the structure of Fig. 6.14. In this case it is required to develop specially adapted pin joints to securely join structural modules and allow a relative rotation during the folding operation. In Fig. 6.15 a foundation column may

be required to support up to three domes simultaneously. Therefore, a dome must first be disconnected from the supporting structure before the folding process can begin. A possible method of supporting the dome during the folding operation is illustrated in Figure 6.16.

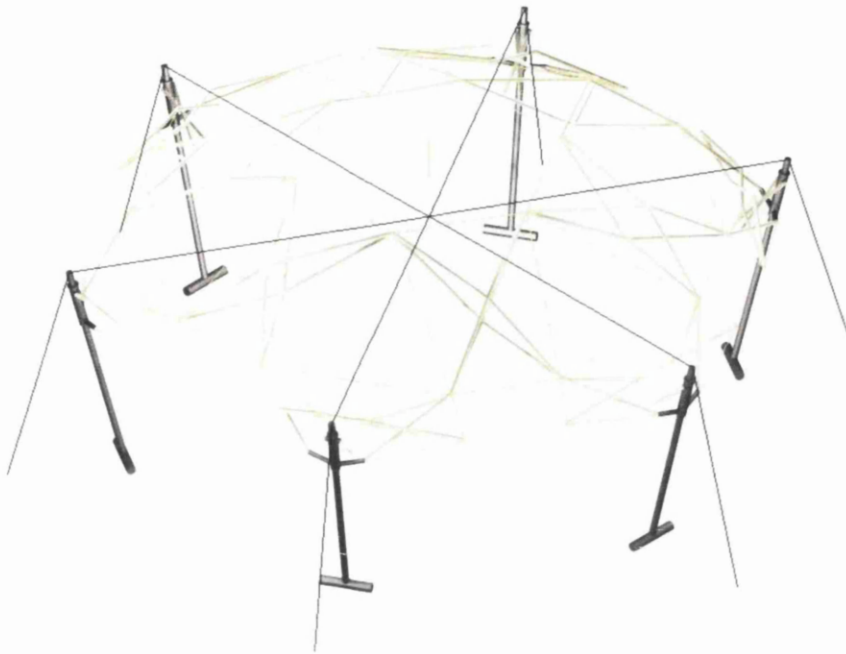


Figure 6.16: Collapsible dome: Possible method of supporting dome structure and controlling the folding operation, illustrated in the fully deployed dome configuration.

In the figure, a number of struts have been disconnected around the perimeter of the dome and certain cables are released in order to activate the folding mechanism. The props which are introduced to support the dome are rigidly attached to the dome sub-structure; however, movement along the axis of the prop is facilitated by a sliding mechanism or roller. A minimum of three small winches would be required to maintain tension in the cables which are connected to the props and a ratchet could be used to control the height of the slider on each prop during the folding operation.

The additional cost of modelling and engineering a dome structure which can be deployed in this way and the complexity of the control mechanisms make this alternative for developing rapidly deployable dome structures less attractive when compared with competing technologies. On the other hand, the range of applications and scope for developing geodesic tensegrity dome structures, which may be rapidly assembled from lightweight tensegrity modules and are attributed with remarkable structural characteristics, far exceeds that which may have been possible using conventional geodesic dome structures.

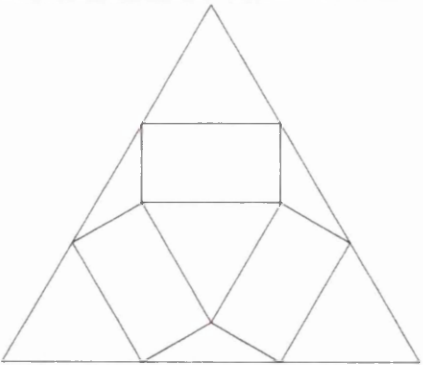
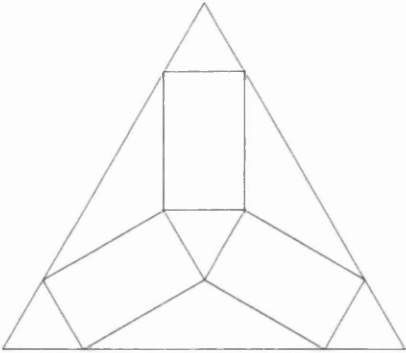
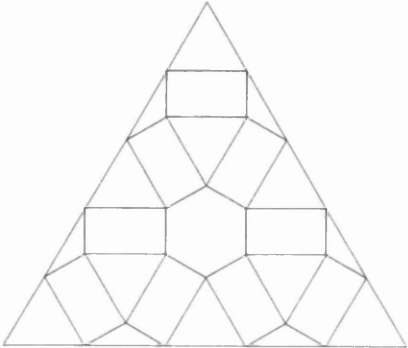
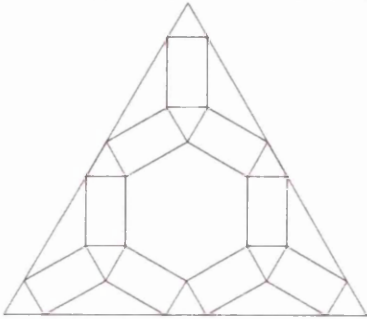
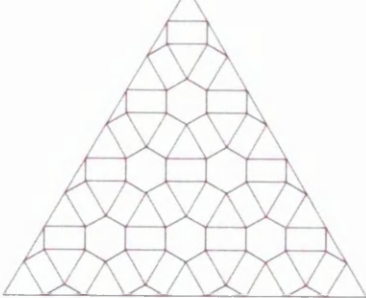
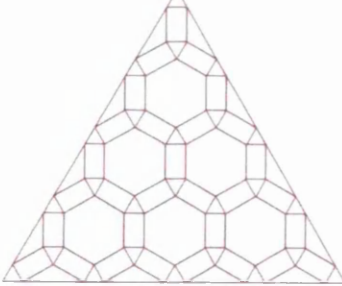
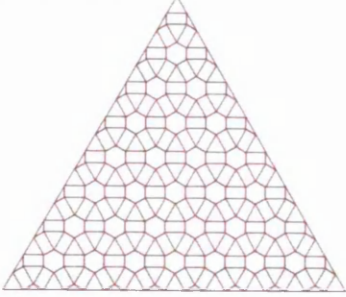
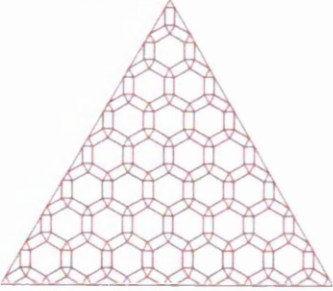
6.3 Generalised geodesic tensegrity structures

In the previous section the basic principles involved in the design of double layer geodesic tensegrity domes and dome honeycomb structures were introduced. To enable dome clustering in a regular hexagonal pattern it was required to develop a dome structure with a hexagonal profile. Starting with basic dome geometry we first identified suitable truncation planes before developing the 3-dimensional structure for the dome. In general, for any honeycomb of hexagonal dome modules it is always possible to exploit the power of the tetrahedron to develop a rigid, efficient supporting structure, which elevates the dome canopy and increases the overall integrity of the structure. In addition, a rigid, lightweight, tensegrity dome superstructure was developed (Fig.6.13), composed of relatively few struts and braced by a double layer network of cables. It is anticipated that developing these relatively simple modular structures could lead to a wide range of practical applications for tensegrity dome structures. On the other hand, a more holistic approach may be required for applications where it is required to span relatively larger areas with minimum internal supports or where a relatively small diameter dome is required for which a double layer dome would be over engineered at low frequencies.

In order to introduce a more holistic approach for the design of geodesic tensegrity structures in general it is first necessary to recognise that it is required to build domes at various frequencies and scales. By "*frequency*," is meant the frequency of subdivision of a sphere used to obtain the dome geometry. It is anticipated that the more important applications will require domes to be built at higher frequencies. Indeed, from experience with geodesic domes, it is well known that, for most terrestrial applications, more efficient dome structures are obtained at relatively higher frequencies. In Chapter 2 an alternative geodesic breakdown system was introduced for developing geodesic tensegrity dome structures. Rather than using a conventional triangular chart lattice structure for obtaining dome nodal coordinates, a more efficient topological structure was proposed known as the X-trihexagonal chart lattice. In this section the general theory and classification scheme for applying geodesic breakdown based on X-trihexagonal lattice structures is developed further (see Table 6.5).

In section 6.2 the principle of structural synergy was referred to in relation to the design of dome honeycomb structures. Yet even though the benefit of applying tensegrity principles was made clear, it is also apparent that we cannot truly describe these primitive dome structures as "*discontinuous compression*" structures. To achieve a true structural synergy it would appear to be crucially important that tension is the dominant cohering force throughout the entire structure. The principle of "*continuous tension, discontinuous compression*" is at the heart of

Table 6.5: Geodesic Tensegrity Chart Lattice Structures

<i>f</i>	<i>Class I X-trihexagonal chart lattice</i>	<i>Class II X-trihexagonal chart lattice</i>
1		
2		
4		
8		

the more holistic approach in design of tensegrity structures which has been advocated by Kenneth Snelson and Buckminster Fuller. Inspired by these two pioneers of tensegrity, a novel structural system is proposed in order to develop highly efficient, double layer tensegrity domes and structures.

In Table 6.5 a general scheme of classification for X-trihexagonal chart lattice types is presented. In this scheme of classification both the frequency, f and the "Class" of a geodesic breakdown has an alternative meaning. For example, the Class I, frequency 2 X-trihex lattice was studied in detail in Chapter 2 in which it was shown how this structure may be constructed from a series of regular triangular lattices. More generally, any X-trihex chart lattice may be constructed from a quasi-regular tessellation composed of triangles and hexagons which is commonly known as a trihexagonal lattice. We may illustrate this transformation by considering its inverse. Note that each rectangle in an X-trihex lattice structure represents an X-module. For simplicity, the struts are not shown in Table 6.5 but if these struts are redrawn we find that they coincide with the edges of a trihexagonal lattice (Fig. 6.17). This is true for both Class I and Class II lattice types although the cable sets are constructed differently in both cases. For a Class I X-trihex lattice the vertices are coincident with those of the underlying trihexagonal lattice, whereas for a Class II X-trihex lattice the vertices are coincident with the mid points of the edges of the trihexagonal lattice. The frequency of subdivision of a particular chart has a natural interpretation through iterative geometric construction and is simply the number of times a frequency 1 lattice structure repeats along the edge of the chart in question.

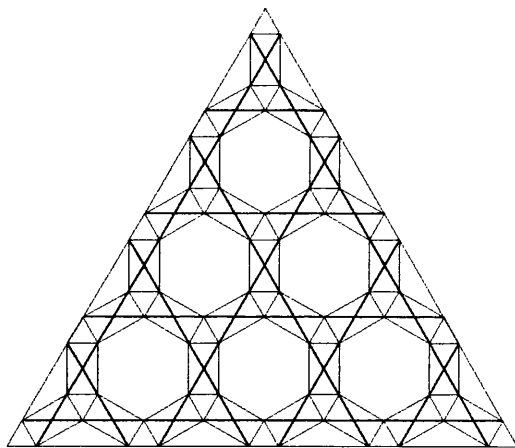


Figure 6.17:

Class II, frequency 4 X-trihex chart lattice. The struts of the X-modules highlighted in bold, black lines, reveal the underlying trihexagonal lattice structure.

By introducing struts as shown in Figure 6.17 and comparing Class I and Class II chart lattices it is immediately apparent that a dome structure based on a Class II lattice will be more efficient than a Class I lattice dome of the same frequency. This is easy to show, since the number of

struts in a Class I and Class II lattice are the same for a given frequency but the struts of a Class II lattice structure will be considerably shorter. As can be seen in Fig. 6.17, this result follows from the fact that the struts are arranged to lie along continuous geodesic curves in a Class II type dome, i.e. they must be the shortest possible.

Figure 6.18 presents a new class of continuous tension, discontinuous compression structure which is represented as a double-layer tensegrity grid composed of X-modules and T-prisms. These new structural systems may be referred to as "*hybrid T-prism modular structures.*"

The hybrid T-prism (Fig. 6.5), based on Snelson's original patent (Snelson, 1965), is the basic, repeating structural unit from which efficient grid like structures can be constructed based on the X-trihex Class II lattice pattern. Utilising the X-trihex Class II geodesic subdivision of a sphere it is fairly straight forward to obtain a double layer tensegrity grid that conforms to the geometry of a dome and is composed of the same basic structural modules as illustrated in Fig. 6.18. Similarly, the transformations from a planar lattice to a cylindrical manifold are fairly easy to obtain in order to generate double-layer grids for barrel vaults.

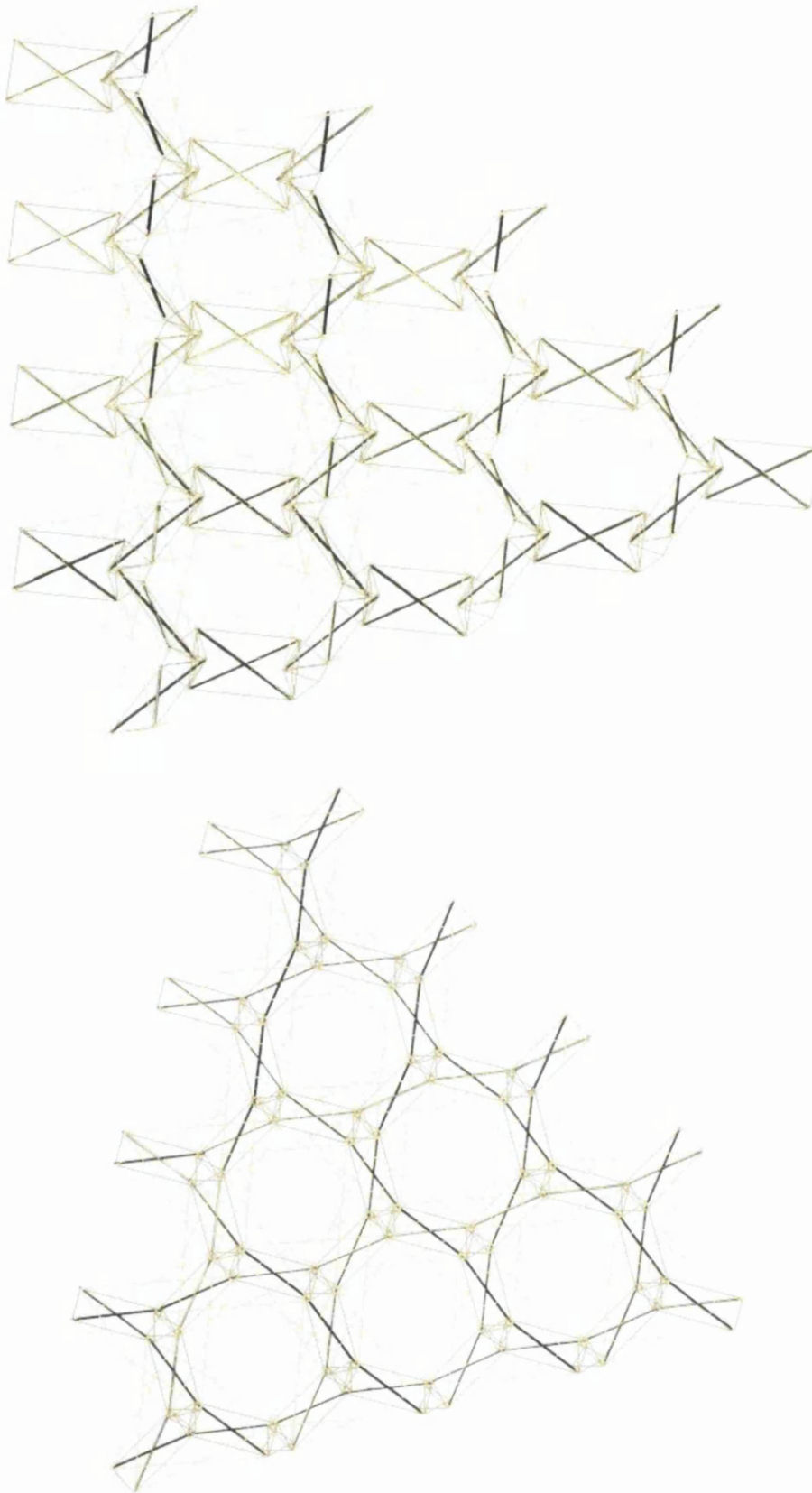


Figure 6.18: Double-layer tensegrity grid composed of X-modules and T-prisms

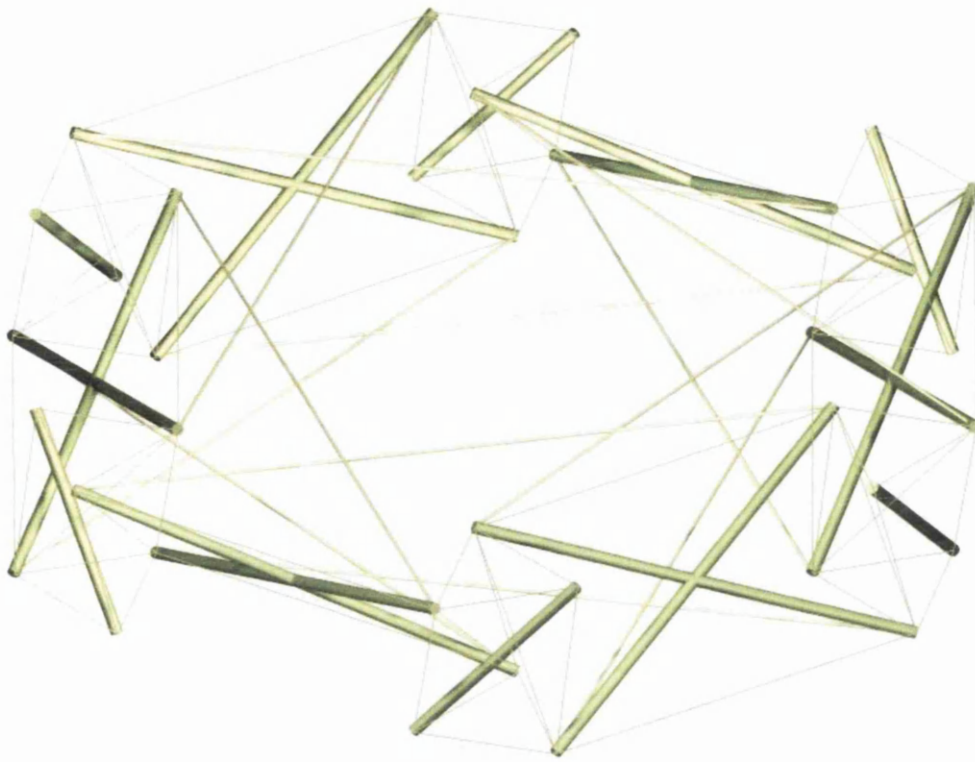


Figure 6.19: Tensegrity Torus: Assembly of 6 X-modules and 6 T-prisms.

Structural details of the double-layer tensegrity grid of Fig. 6.18 are illustrated in Fig. 6.19. The tensegrity torus, represented in the figure, is in itself a tensegrity structure with remarkable structural characteristics. The high stiffness to weight ratio and low density make this structural module ideal for constructing large span geodesic tensegrity domes and other grid like structures. To illustrate the power of the tensegrity torus, struts are inserted to brace each T-prism which, in the larger structure of Fig. 6.18, would be replaced by the edges of connecting X-modules. In addition, the cables which stabilise and inwardly pull the structure together are illustrated in more detail. From Fig. 6.19 it is clear that the T-prisms alternate between left-hand screwed and right-hand screwed T-prisms as we circulate the torus. In the larger tensegrity grid (Fig. 6.18), three X-modules surrounding an internal T-prism form a hybrid T-prism. Therefore, any pair of cables connecting neighbouring X-modules across the inside of the torus (Fig.6.19) belong to a particular hybrid T-prism.

From Fig. 6.18 it is clear that the hybrid T-prisms which make up the structure overlap, in the sense that each X-module is shared by two hybrid T-prisms. The hybrid T-prisms also alternate between left-handed and right-handed screwed prisms, however, in practice the double-layer tensegrity grid may be rapidly assembled from identical tensegrity modules which correspond to

either left-handed or right-handed screwed, hybrid T-prisms. Each module is assembled into the larger grid structure by completing the cable sets which belong to the oppositely screwed, hybrid T-prisms. The assembly process is illustrated in Figure 6.20 where 3 left-handed screwed, hybrid T-prisms are assembled by completing the cable set (highlighted in red) which belongs to the central, right-handed screwed, hybrid T-prism. Clearly, the structural joints and assembly process are much simplified by only having to deal with strut to cable connections, however, special tools, assembly techniques or closure systems may be required in order to pretension the cables and ensure the prestress forces are correctly distributed throughout the entire structure.

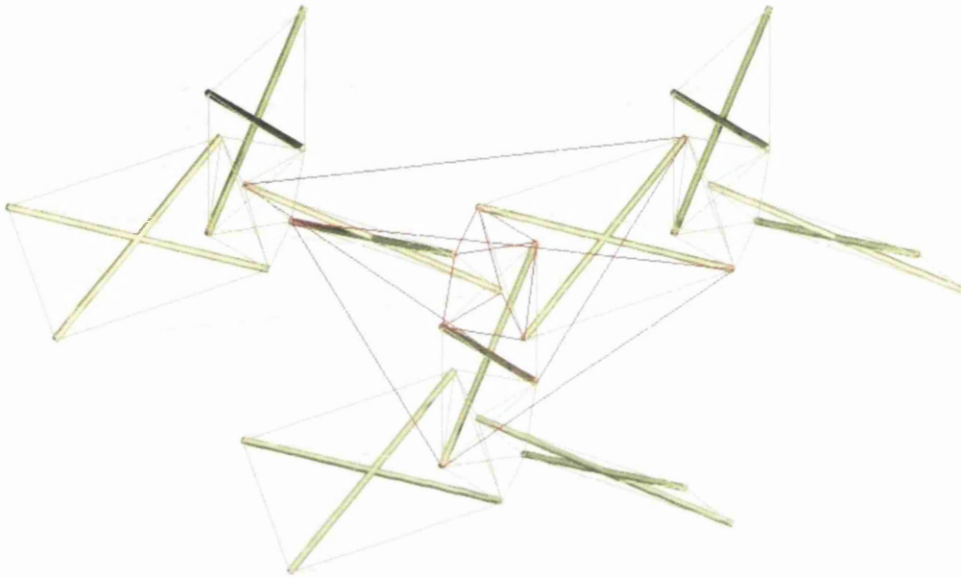


Figure 6.20: Assembly of 3 hybrid T-prisms. 3 left-handed screwed hybrid T-prisms intersect with a central, right-handed screwed hybrid T-prism.

Hybrid T-prism modular structures have a wide range of potential applications and represent an important milestone in the development of super-lightweight, efficient structures. What sets these modular tensegrity structures apart from anything that has come before is that they are the epitome of what has become to be known as “*tensegrity structures*,” and are composed of the most basic, archetypal tensegrity units possible, yet these structures do not suffer from the many disadvantages that have been ascribed to large scale tensegrity structures, which have previously limited their use in practical applications.

The development of hybrid T-prism modular structures also solves many of the problems which have been identified by leading researchers as representing major obstacles to the practical

application of tensegrity technology (Burkhadt, 2008; Motro, 1992). In particular, by employing the most efficient topological structure possible, strut congestion is reduced to a minimum. Simultaneously, the structural synergy is increased to a maximum, as is evident from the mutual strength of the tensegrity torus and hybrid T-prism. The fabrication complexity is also reduced due to the modular nature of the structure and simplicity of cable joints; however, the need to prestress each tensegrity module presents an additional challenge. Importantly, the design complexity is reduced significantly, when compared with other *“floating compression”* structures, proposed by others, which require complex form-finding methods in order to determine a prestressable configuration of the structure. In the design of the hybrid T-prism, the form-finding problem is reduced to finding the initial geometry of the T-prism. Other design parameters can be chosen more freely, which allows flexibility in the overall design.

Double-layer geodesic tensegrity domes based on the hybrid T-prism modular system represent a particular class of structure for which there are immense future possibilities. Such visions of futuristic applications of tensegrity technology as were first espoused by Buckminster Fuller were originally based on the abstract notion of what Fuller himself described as *“tensegrity geodesic spheres.”* What is significant about the abstract tensegrities described by Fuller is that as the technology evolves, the global characteristics of geodesic tensegrity domes match closely those of Fullers hypothetical structures. For instance, we may deduce that tensegrity geodesic spheres do indeed have the properties of hydraulically or pneumatically inflated structures, since at high frequencies the stiffness of a double-layer geodesic tensegrity dome is prestress dominated. To be more precise, for a geodesic tensegrity dome of given size; assuming the extents of the basic structural modules of the dome only change by scale and material properties do not change; there will be an optimum frequency of geodesic subdivision for which the material efficiency of the structure is maximised. Clearly, finding the optimum frequency of geodesic subdivision would be a highly non-trivial problem, since it requires finding the optimum of a series of optimised structures. Nevertheless, incorrectly choosing the frequency of subdivision could lead to domes being built which are several times over engineered, partly because the stiffening effect of prestressing was not taken into account in the early stages of the design.

In order to extend Fuller’s analogy further the following interpretation is proposed. At low frequencies a double-layer geodesic tensegrity dome behaves like a thick spherical shell, whereas at high frequencies it behaves like a thin spherical shell where the efficacy of prestressing diminishes. In between these two extremes there exists a range of frequencies,

about some optimum value, over which the structure takes on the character of a hydraulically or pneumatically inflated structure and responds most favourably to prestressing. Hence, close to the optimum frequency, the stiffness of the structure is said to be prestress dominated. The frequency of subdivision of a double-layer geodesic tensegrity dome is therefore of fundamental importance in determining the optimum prestress geometry and designing for efficiency. A similar principle applies to the design of any double-layer tensegrity grid or network.

The overall structural characteristics and efficiency of a modular geodesic tensegrity structure are largely influenced by the design of the structure at a local level, i.e. the design of the individual tensegrity modules of which the structure is composed. The simplicity and beauty of Ken Snelson's art and approach to tensegrity design has been highly influential in developing efficient tensegrity modules used as the essential building blocks in the design of geodesic tensegrity structures presented in this report. Although the hybrid T-prism was essentially designed by Snelson, the realisation of a method of assembling left-handed and right-handed screwed hybrid T-prisms to form efficient modular structures represents a transformation in the design process. The local structure of a hybrid T-prism modular structure (Fig. 6.18) is characteristically different from that which either Fuller or Snelson may have envisaged, yet it resembles closely one of the strongest structural forms to be found in nature, i.e. that of the Buckminsterfullerene or Carbon Nanotube.

6.4 Applications

The complexity of fabrication which strongly influences manufacturing costs is a particular feature of the geodesic dome which has limited its practical viability as a structural system. This is also an inherent feature of the double-layer geodesic tensegrity dome, although in this case a more practically viable alternative can be obtained by making small adjustments in the geometry. Since it is possible to manufacture cables or tensile elements in great lengths by winding onto spools, there is less wastage involved in dividing a cable into uneven lengths than there would be if it were required to produce a series of struts of uneven length. Also, since struts are more complicated and expensive components to manufacture, it makes sense that they should be manufactured as efficiently as possible. Consequently, the geometry of a double layer geodesic dome may be adjusted such that struts are of equal length throughout, whereas cables vary in length to take account of the distortion. Although this does not reduce the overall complexity of the design and requires the use of more ad hoc design methods, when the

frequency of subdivision is relatively high the modified geometry will not be noticeably different, since overall, member dimensions vary considerably less at high frequencies.

Other potential future applications of tensegrity technology include the development of dome honeycomb structures based on the hybrid T-prism modular system. Again, the design complexity increases as the frequency of subdivision increases, particularly as the geodesic geometry does not naturally generate the truncation planes which must be introduced to form a boundary between neighbouring domes. An advantage of the dome honeycomb structure is that due to the repetition of identical dome modules over a wide area, as the number of domes increases, the manufacturing costs per individual dome reduce substantially due to economies of scale. Therefore, dome honeycomb structures could potentially overcome the problems of manufacturing cost which have hindered the development of geodesic domes worldwide. It is anticipated that for most practical applications the simplest dome honeycomb structures would be employed by maintaining a relatively low frequency of subdivision of individual domes, since it is not required to span a large area within a single dome.

Perhaps the greatest potential for developing tensegrity structures for large scale applications lies in the development of a new agriculture based technology employing large scale greenhouses in order to provide a sustainable production of food and energy from solar power. To develop large scale commercial greenhouse structures a simple, practical solution is required, that is both structurally efficient and cost effective. In this case we may employ the hybrid T-prism modular system in order to develop large span vaulted roofs which are typically used for large, rectangular buildings. Whereas conventional, commercial greenhouses tend to employ simple roof structures which are supported by several, uniformly spaced internal columns, a vaulted roof, comprised of a double-layer tensegrity grid structure, is designed to span a large area, largely unsupported. The removal of internal supports and increase in the internal height and volume of the greenhouse improves the ease/efficiency with which agricultural operations can be performed, improves the air-circulation/ventilation and thermal/energy efficiency of the greenhouse. The vaulted roof also has a considerable advantage over the domed roof in terms of fabrication complexity, cost and practicality. Provided that the arch of the vaulted roof corresponds to a circular arch, the geometry of each hybrid T-prism comprising the modular roof structure will be identical, thus, considerably reducing manufacturing costs due to economies of scale. By developing more efficient greenhouse structures the scale and range of applications for greenhouse technology in food production will be considerably enhanced. In the future, greenhouse technology could form a

basis for developing more sustainable systems of food and energy production, which have positive environmental side effects, including the sequestration of atmospheric carbon and restoration of organic soils.

As an architectural concept, the dome honeycomb has special significance as an example of the application of principles of bio-mimicry in infrastructure design. Perhaps, more than any other structural system, the geodesic tensegrity dome honeycomb has the highest potential for facilitating sustainable development by promoting Fuller's design science revolution and fostering positive social, economic and environmental change. Dome honeycomb structures are designed principally as lightweight, efficient structures for agricultural greenhouse systems, however, due to the modular nature of the structure, dome honeycombs are easily scalable, whereas the individual domes, of which the structure is comprised, are built in a standard size. Consequently, dome honeycomb structures are more suitable for mass production and due to scalability there is a higher demand for such products at grassroots level, where people are most in need of sustainable systems of food production.

With the aid of modern technology and innovative energy solutions the solar energy captured within a greenhouse may be harnessed with the potential to produce large surpluses of useful thermal and/or electrical energy. Key challenges involve developing more efficient and reliable heat engines for converting low grade thermal energy into electricity and developing cost effective thermal energy storage solutions. In the commercial greenhouse industry semi-closed greenhouses have been developed, which make use of relatively simple energy management systems incorporating mechanical dehumidification, heat pumps and underground aquifer thermal energy storage. The greenhouse is heated in the winter months using heat which has been stored in the summer months and an overall reduction in energy consumption of between 20% and 30% is achievable, while the capital costs of the system are reasonable compared with competing technologies. The first generation of semi-closed greenhouses and fully closed greenhouses were less economically viable due to high infrastructure costs and electricity demanded by the thermoregulatory system for operating with high cooling loads. What these early experiments have shown is that, even in a north European climate, large surpluses of thermal energy can be easily generated, typically two to three times the annual heating demand for the greenhouse. As the technology evolves and the costs of thermoregulatory systems reduce we could see a resurgence of interest in energy producing greenhouses, which maximise use of natural resources. By developing solar trigeneration systems (i.e. combined cooling, heating and power) in conjunction with thermal energy storage systems it is

theoretically possible to regulate the internal climate of a greenhouse, while simultaneously optimising the electrical and thermal energy outputs. The advantage of this form of electrical power generation is that by exploiting thermal energy storage we may generate an almost continuous supply of electricity using simple, efficient heat engines. Since the heat rejected by a heat engine can easily be recycled in the thermoregulatory system it is possible to use efficient and reliable, regenerative heat engines that operate with a low Carnot efficiency but which achieve actual efficiencies that are much higher due to the recycling of thermal energy.

Dome honeycombs have a wide variety of potential applications which could be combined within a single honeycomb structure by exploiting the modular nature of the structural system. The structural diversity which can be achieved within this architectural medium strongly contrasts the regularity of the honeycomb structure and can be used as an example of bio-mimicry in infrastructure design. As the name suggests, the example from nature is a beehive honeycomb, in which different sections of the honeycomb are used for different purposes. Based on the principle of bio-mimicry, we may partition sections of a dome honeycomb and introduce thermal barriers between different compartments. Some sections of the honeycomb would be used as living quarters, whereas others would be used for growing crops or rearing livestock. In order to achieve thermal and atmospheric control within the different compartments, simple passive ventilation systems which achieve up to 90% heat recovery through use of efficient heat exchangers have been devised for the building industry. These could be used in conjunction with mechanical cooling, heat pumps and thermal energy storage systems. By storing hot and cold water in separate lagged compartments for short term thermal energy storage, supplemented by a long term aquifer thermal energy store, it would be possible to satisfy all the heating requirements of the community using solar energy collected from the greenhouses. In addition, by operating a heat engine between the hot and cold reservoirs it would be possible to convert most of the excess thermal energy into electricity. Thus, infrastructure design based on dome honeycomb structures provides an example of how we may build a sustainable technological society based on solar power and efficient use of resources.

6.5 References

Burkhardt, R. B. (2008). *A Practical Guide to Tensegrity Design*, 2nd edit. [ONLINE] Available at: http://www.angelfire.com/ma4/bob_wb/tenseg.pdf. [Accessed 23 August 2015]

Motro, R. (1992). Tensegrity Systems: The State of the Art. *Int. J. Space Structures*, 7, pp. 75-84

Snelson, K. D. (1965). *U.S. Patent No. 3,169,611*. Washington, DC: U.S. Patent and Trademark Office.

Tarnai, T. (1980). Simultaneous static and kinematic indeterminacy of space trusses with cyclic symmetry. *Int. J. Solids Structures*, 16(4), pp. 347-359.

Chapter 7 Conclusions

A range of innovative structural systems are developed and presented in this report, which demonstrate the effective application of scientific principles in the design of tensegrity structures for practical applications. Building on the tensegrity design principles and geodesic geometry pioneered by Buckminster Fuller, this project focuses on developing the intrinsic geometry for a range of efficient, modular, geodesic tensegrity structures. By developing 3-dimensional tensegrity modules, based on Kenneth Snelsons original patent designs, a new class of “*floating compression*,” modular structural system is proposed from which the geometry of a range of double layer tensegrity grids, domes and barrel vaults can be derived. A new system for clustering domes in two dimensions is developed and discussed in analytical detail. Dome designs are developed, including single layer and double layer tensegrity domes suitable for clustering in two dimensions to form dome *honeycomb* structures. The transformation equations and analytical geometry required to generate dome geometry are derived from first principles.

In this report, the computational, matrix methods required for the structural design optimisation of tensegrity domes and frameworks are explained in detail. Computational methods based on the Singular Value Decomposition of the equilibrium matrix are reviewed and explained. Matrix methods for the assembly of global equilibrium matrices from element matrices are presented for both 2-dimensional reticulate assemblies and 3-dimensional dome frameworks. The importance of exploiting the structural symmetry, characteristic of dome structures, in order to simplify structural calculations is illustrated throughout the analysis process. Advanced techniques used to analyse symmetric structures subject to a general loading are reviewed and explained in detail. Finally, the theoretical basis for analysis of inextensional mechanisms and prestress states is reviewed and simple algorithms are presented for the analysis of kinematically indeterminate tensegrities and optimisation of prestress forces.

Chapters 3 and 4 focus on presenting a general, unified computational framework with sufficient analytical detail and algorithm development to enable the computational analysis of large dome frameworks and tensegrity structures in general. As well as reviewing and explaining the existing literature which deal with specialised computational methods for analysis of tensegrity structures this section of the report also includes some novel aspects in explaining how computational methods involving the equilibrium matrix of specific and/or general structures may be implemented and how to choose an appropriate coordinate system to make

computations and implementation of symmetry sub-structuring techniques as simple and efficient as possible.

Chapter 4 also includes new algorithms which improve the efficiency and ease with which symmetry subspace methods can be implemented in a computer program. The symmetry subspace methods presented in Chapter 4 are suitable for the analysis of large symmetric structures such as geodesic tensegrity domes and particularly, dome structures with a high degree of rotational symmetry. As most of the dome structures designed for clustering in a 2-dimensional honeycomb structure have six-fold symmetry the example structures for which the implementation of symmetry subspace methods are illustrated also possess the full symmetry of the C_{6v} symmetry group.

Chapter 5 is mainly concerned with the theoretical background required for the analysis and optimisation of prestressed mechanisms, frameworks and kinematically indeterminate tensegrity structures. A similar approach used for mechanism order analysis by asymptotic methods could also be useful in developing a more mathematically rigorous method for the analysis of prestressed mechanisms, similar to that developed by Pellegrino (1990) however, this is an area which requires further investigation. The integral feasible prestress algorithm developed by Yuan and Dong (2003) illustrates well how we may exploit symmetry in order to simplify the prestress optimisation problem. It would be useful to develop this method further and to develop new algorithms to perform the prestress optimisation of more general types of symmetric tensegrity structures and domes. As explained in Chapter 5, analysis of symmetric structures using group representation theory could also be applied in order to simplify the integral feasible prestress algorithm and develop more general methods.

In summary, this report presents the results of a series of design cycles which involve consecutive rounds of identifying intentions, design realisations and evaluation of results within an adaptive, reiterative, expansive design process. By combining the simplicity and elegance of Snelson's designs with the geodesic geometry presented by Fuller; and developing more efficient topological structures, based on abstract reasoning; a range of efficient, modular structures have been developed which are broadly classified as "*geodesic tensegrity structures*". The motivating ambition of developing lightweight efficient structures for applications in agriculture and sustainable development and the efficacy of the application of logic and the scientific method are clearly apparent in the design process. General design solutions to applied problems are discussed, including issues related to manufacturability, operational use, functionality and the multidisciplinary nature of the problem.

Clearly, there are limitations on what can be achieved in a preliminary investigation of this nature, however, it is anticipated that much future research and technological developments will follow on from this report. In particular, it would be necessary to analyse and develop specific structures in more detail, look in more detail at the optimisation problem and develop computer programs to perform the analysis of dome structures based on the methods presented in this report. For the purpose of developing structures specifically for meeting sustainable development goals it would be necessary to consider innovative low carbon solutions in the use of appropriate materials and technology to replace conventional lightweight materials and construction techniques. It is apparent that bamboo could perform well as a strong, lightweight material. Wood materials, bio-composites and biopolymers represent a range of materials that could be developed further for applications in dome and greenhouse design. More generally, by developing innovative joint designs and employing nature inspired structural geometry it is anticipated that tensegrity structures and prestressed frameworks would come to represent the lightweight, efficient structures of the future and become more widely utilised by practicing engineers.